Topics in weak gravitational lensing

by

Isaac Spitzer

A thesis
presented to the University of Waterloo
in fulfillment of the
thesis requirement for the degree of
Doctor of Philosophy
in
Physics

Waterloo, Ontario, Canada, 2022

Examining Committee Membership

The following served on the Examining Committee for this thesis. The decision of the Examining Committee is by majority vote.

External Examiner:	Tereasa Brainerd Department of Astronomy, Boston University
Supervisor(s):	Michael J. Hudson
Internal Member:	Michael Balogh James Taylor
Internal-External Member:	Wayne Oldford

Author's Declaration

This thesis consists of material all of which I authored or co-authored: see Statement of Contributions included in the thesis. This is a true copy of the thesis, including any required final revisions, as accepted by my examiners.

I understand that my thesis may be made electronically available to the public.

Statement of Contribution

I was the sole author for Chapters 1 and 5 which were written under the supervision of Michael Hudson. This thesis consists in part of three manuscripts written for publication. Exceptions to sole authorship of material are as follows:

Research presented in Chapter 2:

The research in Chapter 2 is based on a submitted paper (Spitzer et al., 2021), that was written under the supervision of Michael Hudson. I was the main author of the manuscript with contributions from all co-authors.

Research presented in Chapter 3:

The research presented in Chapter 3 was done under the supervision of Michael Hudson. The computational analysis presented in the both the chapters is my work. I was the main author of this manuscript with contributions from Michael Hudson.

Research presented in Chapter 4:

Chapter 4 is based on research done in collaboration with Michael Hudson and the CFIS team, primarily Ludo van Waerbeke, Martin Kilbinger, and Axel Guinot. I was the main author of this chapter, with contributions from Michael Hudson.

Research presented in Appendix A:

Appendix A is based on an idea presented to me by Michael Hudson. The design and implementation was done by myself. I was the main author of this appendix, with contributions from Michael Hudson.

Abstract

In this thesis, various topics pertaining to weak gravitational lensing and its application to cosmology and galaxy evolution are explored.

The first chapter is the introduction which contains all of the background information needed to understand the rest of the thesis. Topics covered include cosmology, structure formation, the formation and evolution of galaxies, weak gravitational lensing, galaxy shape measurement, and simulations for the measurement and correction of biases in weak lensing surveys.

In the second chapter of this thesis, we present an analysis of weak lensing signals around galaxy groups and clusters using the data from the Canada-France Imaging Survey (CFIS), part of the Ultraviolet Near-Infrared Optical Northern Survey (UNIONS). Lenses are selected from the Tinker group catalogue and the redMaPPer cluster catalogue, and binned by estimated halo mass and richness. The weak lensing shape distortions around groups and clusters are then fit with simple models out to the virial radius. For redMaPPer clusters, we evaluate the mass-richness relation and find good agreement with previous results using other weak lensing data sets. We make the first weak lensing measurement of the masses of galaxy groups selected from the Tinker (2020a) catalogue, finding better agreement if the cosmological parameters have a lower value of $S_8 \equiv (\Omega_\mathrm{m}/0.3)^{0.5}\sigma_8 = 0.74 \pm 0.03$. Additionally, we bin the groups by the colour of the central galaxy and confirm evidence for a bimodality in halo masses between groups with red and blue centrals for stellar masses $> 10^{11} M_\odot$.

In the third chapter, we present a weak lensing analysis of satellite galaxies in galaxy group environments. We find a mean satellite mass from satellites selected from the Tinker (2020a) catalogue of $\log_{10} \langle \frac{M_\mathrm{sat}}{h^{-1} M_\odot} \rangle = 12.5 \pm 0.2$. Satellite galaxies in these environments are also predicted to be tidally stripped. We place a 1σ lower limit on the truncation radius of 19 h^{-1} kpc. We then attempt to measure the truncation radius as a function of their projected separation from the group centre, but find that binning the satellites reduces the strength of the signal too significantly to measure such an effect.

In the final chapter of the thesis, we explore the topic of bias calibration in weak lensing surveys. A set of simulations designed to mock CFIS/UNIONS weak lensing observations is described. These simulations have a known shear applied to them, which can then attempt to be recovered via the weak lensing pipeline utilized by the survey. Initial measurements of the multiplicative and additive biases, which can be used to calibrate the shape measurements, are made.

Dedication

For Carlos,
I know you would have been proud, and I will miss you always.

Table of Contents

List of Figures

List of Tables

Chapter 1

Introduction

1.1 Background Cosmology

The currently leading cosmological model is the ΛCDM model, which features three key components. The first, and least abundant component, is baryonic (or "ordinary") matter, that makes up the stars, galaxies, and planets that we observe.

The second component is cold dark matter (CDM). One of the earliest mentions of dark matter was made in the first half of the twentieth century (Zwicky, 1933). Zwicky suggested that there may be matter present that doesn't appear in observations to explain the discrepancy between the motions of satellite galaxies in galaxy clusters, and their mass as inferred by the brightness and number of galaxies in the cluster. Over time, other lines of evidence also pointed to the presence of some form of invisible matter. The masses of spiral galaxies as estimated by the motion of their stars implies a much larger mass than what is contained in the gas and stars (Roberts & Rots 1973, Rubin et al. 1978). Gravitational lensing has been used to analyze interacting clusters and has shown that the distribution of the baryonic matter does not match the total matter distribution (Clowe et al., 2004). Finally, measurements of the power spectrum of the cosmic microwave background (CMB) show acoustic peaks which imply the presence of a significant matter component that was decoupled from the radiation field in the very early universe (de Bernardis et al. 2000, Hanany et al. 2000).

The third, and most abundant component, is dark energy. Einstein favoured the idea that the universe is static - neither expanding nor contracting. To keep the universe static, he proposed a "cosmological constant" (Λ) that would counteract gravity. He soon discarded this concept after being presented with evidence that the universe is expanding by Hubble (1929). By the

1990's, however, observations were showing evidence that a cosmological model without some form of cosmological constant was insufficient to explain structure on the largest scales. New models, including both dark matter and a cosmological constant, began to be proposed (Efstathiou et al., 1990; Ostriker & Steinhardt, 1995). This model of the universe was then solidified when observations of distant Type Ia supernovae to construct a distance-redshift relation showed an acceleration in the expansion of the universe (Riess et al. 1998, Perlmutter et al. 1999).

These three components, combined with Einstein's theory of relativity, provide a framework that has been very successful at explaining observations from a wide range of physical and mass scales from the very early universe up to today. This cosmology can be expressed mathematically beginning with the Robertson-Walker metric, which describes an isotropic, homogeneous universe.

$$\mathrm{d}s^2 = c^2\mathrm{d}t^2 - \mathrm{d}l^2 = c^2\mathrm{d}t^2 - a^2(t)\left[\frac{\mathrm{d}r^2}{1-Kr^2} + r^2(\mathrm{d}\theta^2 + sin^2\theta\mathrm{d}\phi^2)\right] \tag{1.1}$$

Here, ds is the space-time interval, $a(t)$ is the scale factor, which is defined as 1 for the present day, K is the sign of the spatial curvature, and r, θ, and ϕ are the comoving coordinates. With $K = 0$, the universe is spatially flat. For non-zero values, the universe is either closed ($K < 0$), or open ($K > 0$). Observations have shown that the universe is, within the margin of error, consistent with being flat (de Bernardis et al. 2000, Planck Collaboration et al. 2020).

The scale of the universe is described by the Friedmann equation

$$H^2 = \left(\frac{\dot{a}}{a}\right)^2 = \frac{8\pi G}{3}\rho_{\mathrm{tot}} - \frac{Kc^2}{a^2} \tag{1.2}$$

where H is the Hubble parameter, G is the gravitational constant, ρ_{tot} is the total energy density of the universe, and c is the speed of light in a vacuum. The Hubble parameter is generally given in units of km/s/Mpc, and describes the rate at which galaxies are receding from us as a function of their distance. By setting K to 0 and solving for ρ_{tot}, we arrive at the critical density

$$\rho_{\mathrm{tot,cr}} = \frac{3H^2}{8\pi G}\,. \tag{1.3}$$

This defines the density required for the universe to be spatially flat. We can then define the density parameter, Ω

$$\Omega \equiv \frac{\rho}{\rho_{\mathrm{tot,cr}}} = \frac{8\pi G\rho}{3H^2} \tag{1.4}$$

It is also possible to rewrite the Friedmann equation (Equation 1.2) in terms of the components of the density parameter.

$$H^2(a) = H_0^2\left[\Omega_{\Lambda,0} + \frac{\Omega_{m,0}}{a^3} + \frac{\Omega_{r,0}}{a^4} + \frac{\Omega_{K,0}}{a^2}\right] \tag{1.5}$$

Here, Ω_Λ is the fraction of the total energy contributed by dark energy, Ω_m by matter, and Ω_r by radiation. The 0 subscript denotes that these are values measured in the universe at the present time. $\Omega_{K,0} \equiv 1 - \Omega_0$ is the spatial curvature density.

The Friedmann equation evolves as

$$\dot{H} + H^2 = \frac{\ddot{a}}{a} = -\frac{4\pi G}{3}\left(\rho_{\text{tot}} + \frac{3p_{\text{tot}}}{c^2}\right), \tag{1.6}$$

where p_{tot} is the total fluid pressure. This is broken down into three components: non-relativistic matter, radiation, and the cosmological constant that is responsible for dark energy. The relation between pressure and density is defined by the equation of state parameter, w.

$$p_i = w\rho_i c^2 \tag{1.7}$$

Each of the three fluids has a different value for w. For non-relativistic matter, $w = 0$. For radiation, $w = 1/3$. For the cosmological constant, $w = -1$, and it thus exerts a negative pressure. The scale factor, a, for spatially-flat single-component universe with $w > -1$ can be expressed as

$$a(t) = a_0 t^{\frac{2}{3(w+1)}}\,. \tag{1.8}$$

We can therefore examine how the universe scales at different epochs. During the early universe, when it was radiation dominated, $w = 1/3$ and $a(t) \propto t^{1/2}$. As the universe expanded, it became matter dominated, where $w = 0$ and $a(t) \propto t^{2/3}$. In the present day, the universe is in the era of dark energy domination, so $w = -1$ and the universe expands exponentially. This result can be obtained by solving the Freidmann equations for a single-component flat Universe with $\Omega_\Lambda = 1$.

1.2 Galaxy Formation and Evolution

Here, I will provide a brief overview of the topics of galaxy formation and evolution. First, I will cover the growth of structure, the collapse into haloes, and the formation of galaxies. I will then give an overview of the various effects that contribute to the evolution of galaxies and how the environment they reside in drives that evolution.

1.2.1 Galaxy Formation

The formation of structure in the universe begins in its earliest phases. According to inflationary theory (Guth, 1981), the very early universe undergoes a stage of exponential expansion. This inflation creates quantum fluctuations in the density field which are then magnified by the exponential expansion. After this inflationary period ends, the universe continues to expand, though at a much slower rate. The overdense regions continue to attract matter gravitationally and become the haloes that we observe today. The underdense regions continue to become more rarefied as matter is attracted to the overdense regions. Thus, the quantum fluctuations in the early universe are the seeds for the future growth of structure in the universe. The inflationary period therefore stretches out the initial inhomogeneities to large scales.

While the concept of inflation was not proposed until the late 1970s, the idea that structure can form from gravitational instabilities was being developed much earlier. Gamow & Teller (1939), for example, considers the growth of gravitational instabilities in an expanding universe. The density perturbations can be described by the density contrast, $\delta\rho/\rho$, which compares the size of the density fluctuation to the mean density of the universe. In the early stages of the universe, the density contrast is small ($\delta\rho/\rho \ll 1$), and the fluctuations expand in physical size due to the expansion of the universe. During this phase, the perturbations are said to be in the linear regime. As the fluctuations continue to grow with time, eventually a turning where $\delta\rho/\rho = 1$ is reached. At this point, the overdensities become nonlinear and are sufficiently large that they separate from the expansion of the universe and begin collapsing. The growth of the perturbations in an expanding universe can be expressed as a power law of time (Lifshitz, 1946):

$$\delta\rho/\rho \propto t^{\alpha} \,. \tag{1.9}$$

Gunn & Gott (1972a) took the theory of nonlinear growth and considered a spherically symmetric perturbation from the early stages of its growth, through its turn-around and eventual collapse into a virialized structure. Press & Schechter (1974) expanded on this work by considering an initially Gaussian density field, which resulted in the Press-Schecter mass function.

$$n(M,t)\mathrm{d}M = \sqrt{\frac{2}{\pi}}\frac{\bar{\rho}}{M^2}\frac{\delta_c}{\sigma}\exp\left(-\frac{\delta_c^2}{2\sigma^2}\right)\left|\frac{\mathrm{d}\,\ln\sigma}{\mathrm{d}\,\ln M}\right|\mathrm{d}M \tag{1.10}$$

where δ_c is the required density contrast to collapse into a halo, and σ^2 is the variance of the density field. The mass function, which describes the number of collapsed haloes we expect to see as a function of their mass, arises from inflation and the growth of structures over time. By counting and measuring the masses of haloes, we can observationally reconstruct this mass function. We can then compare this reconstruction to predictions from various cosmologies,

and therefore estimate cosmological parameters like σ (e.g. Costanzi et al. 2021). This topic is discussed further in Chapter 2.

For ΛCDM cosmologies, the Press-Schechter mass function predicts a much larger number of small haloes than large ones. This leads to the so called "bottom-up" theory of galaxy formation, whereby the largest structures in the universe are formed via the coalescence and merging of smaller objects. This picture of structure formation is supported by observations of the number counts of galaxy clusters (e.g. Bahcall & Cen 1993), measurements of the galaxy power spectrum (e.g. Reid et al. 2010), and the cosmic microwave background (e.g. Planck Collaboration et al. 2020).

Up to this point, the discussion has focussed on the growth of structures and dark matter haloes. While this is important for understanding the seeding of the universe with overdensities that contain star forming material, there are additional physics at play that determine how a cloud of gaseous material collapses to form a galaxy.

For a cloud of gaseous material to remain in hydrostatic equilibrium, the gravitational force must be equivalent to the outward pressure

$$\nabla P(r) = -\rho(r)\nabla\Phi(r) \tag{1.11}$$

where $\nabla P(r)$ is the pressure gradient, $\rho(r)$ is the density profile, and $\nabla\Phi(r)$ is the gravitational potential gradient. The gravitational potential here must satisfy the "Poisson equation"

$$\nabla^2\Phi = 4\pi G(\rho_{\rm dm} + \rho) \tag{1.12}$$

where G is the gravitational constant, $\rho_{\rm dm}$ is the dark matter density, and ρ is the baryonic matter density. For a simple model where the proto-galaxy is spherically symmetric and the gas is an ideal gas, the pressure gradient can be expressed as

$$\frac{{\rm d}P}{{\rm d}r} = \frac{{\rm d}(k_{\rm B}T\rho/\mu m_{\rm p})}{{\rm d}r} \tag{1.13}$$

where $k_{\rm B}$ is the Boltzmann constant, T is the temperature, μ is the mean molecular weight of the gas, and $m_{\rm p}$ is the mass of a proton. The potential gradient for this model can be expressed as

$$\frac{{\rm d}\Phi}{{\rm d}r} = \frac{GM(r)}{r^2} \tag{1.14}$$

where $M(r)$ is the total mass of both the dark and baryonic components.

In order for a cloud of gaseous, baryonic material to undergo gravitational collapse and form a galaxy, the gravitational force must exceed the internal pressure of the gas. In terms of time

scales, the cooling time, which represents how quickly gas dissipates energy, must be shorter than the free-fall time, which represents how quickly a cloud can collapse under gravity. Under this condition, cooling becomes a runaway process and the cloud collapses in on itself.

The energy of the gas as it compresses can be carried away by bremsstrahlung, whereby electrons are accelerated by nearby nuclei. The cooling rate due to bremsstrahlung, or free-free emission, can be characterized as

$$C_{\rm ff} = \int \epsilon_{\rm ff}(\nu) {\rm d}\nu \approx 1.4x10^{-23} T_8^{1/2} \left(\frac{n_e}{\rm cm^{-3}}\right)^2 {\rm erg\,s^{-1}cm^{-3}} \tag{1.15}$$

where $\epsilon_{\rm ff}$ is the free-free emissivity, $T_8 \equiv T/(10^8 K)$, and n_e is the number of electrons.

Bremmstrahlung is most effective at high mass scales, like galaxy clusters, where temperatures are hot. At lower temperatures, other cooling processes become more important. These other processes involve interactions between atoms and electrons. If an electron collides with an atom, ionizing it in the process, the gas loses energy equal to the ionization threshold. This is known as collisional ionization. If the collision excites a bound electron, but doesn't ionize the atom, a photon is released when the electron returns to the ground state. If an ion and an electron recombine, a photon is emitted which carries energy out of the cloud, causing it to cool and contract and lowering the internal pressure.

Because the actual cooling rate is the combination of several temperature-dependent processes, the overall rate for an optically thin gas is generally expressed as a cooling function such as

$$\Lambda(T) \equiv \frac{C}{n_{\rm H}^2} \tag{1.16}$$

where $n_{\rm H}$ is the number density of hydrogen atoms. For higher temperatures ($T > 10^{5.5}$), bremsstrahlung is the dominant process for cooling, and the resulting cooling function looks similar to Equation 1.15. At lower temperatures, these other processes dominate and the cooling function is more complex.

Another consideration is the role of shocks in galaxy formation. Shocks can occur when two clouds of baryonic material collide with one another, when a cloud accretes additional material onto itself, and when a star ejects its material into the surrounding cloud at the end of its life. These high density shock fronts compress the gas, which can cause it to collapse and form stars.

So far, all of these process have led to gas cooling. However, observations show that not all gas cools to form stars. Therefore, there must be processes that either prevent cooling or actively heat the gas to prevent it from collapsing and forming stars. One such process is called feedback. When massive stars reach the end of their lifecycle, they become supernovae - exploding stars

that release energy and material back into their surroundings. These explosions serve to heat the environment and create a galactic wind that can blow the surrounding gas out of the galaxy, thus slowing the cooling the process.

Another source of feedback is active galactic nuclei – supermassive black holes that lie in the central regions of massive galaxies. These black holes are surrounded by a disk of material. As this gas is accreted onto the black hole, it emits an immense amount of radiation which heats the surrounding environment.

While the descriptions of the various effects that lead to the formation of galaxy formation have relied on simplistic models, in reality the interactions between the numerous processes is incredibly complex. The integration of these physical processes in modern studies of galaxy formation tends to be done via numerical simulations. For a thorough review of the topic, see Vogelsberger et al. (2019).

1.2.2 Galaxy Evolution

The topic of galaxy classification begins with Hubble (1926). Hubble devised what is known as the "Hubble tuning fork", where galaxies tend to be classified as either spirals or ellipticals depending on the presence of spiral arms, or irregulars if they lack a well defined structure. While the structural differences are used to classify these galaxies, morphology is one of many properties that separates spirals from ellipticals.

Elliptical galaxies tend to be larger, more massive, poorer in gas content, redder, and as the name suggests, more elliptical, than spiral galaxies. Since higher mass, hotter, bluer stars have shorter lifespans than their lower mass counterparts, the colour of a galaxy is an important indicator of star formation. Blue galaxies have had more recent epochs of star formation given the presence of the high mass stars that give them their colour. In this sense, blue galaxies are often referred to as star forming, while red galaxies are referred to as quenched.

Another key difference is the observation that the redder, quenched, elliptical galaxies tend to live in more dense environments. These elliptical galaxies are more often found in galaxy clusters, whereas star forming spirals are more likely to be found in the field, with fewer nearby neighbours (Oemler 1974, Dressler 1980).

Here, I will outline a few of the key physical processes that affect galaxies in dense cluster and group environments. These processes are responsible for the evolution of field galaxies as they are accreted into their new surroundings.

Dynamical Friction

Dynamical friction occurs when a satellite galaxy is moving through the halo of its host. Because the host halo consists of particles that interact gravitationally with the satellite galaxy (such as dark matter and the intracluster medium), the satellite forms a density enhancement of particles behind it, much like a wake. This density enhancement of particles behind the satellite creates a drag, slowing the satellite and causing its orbit to decay.

The theory of dynamical friction was first described by Chandrasekhar (1943). While Chandrasekhar was describing the deceleration of stars moving through fields of other stars (as in galaxies and star clusters), the physics applies to massive objects in general that are moving through extended fields of other particles, such as satellites through a cluster. By assuming that all involved masses are points masses, and that the distribution of field particles is isotropic, homogeneous, and infinite, Chandrasekhar arrives at the following formula for the dynamical friction force:

$$\vec{F}_{\rm df} = M_{\rm S}\frac{{\rm d}\vec{v}_{\rm S}}{{\rm d}t} = -4\pi\left(\frac{GM_{\rm S}}{v_{\rm S}}\right)^2 \ln\lambda\,\rho(<v_{\rm S})\frac{\vec{v}_{\rm S}}{v_{\rm S}} \tag{1.17}$$

where $M_{\rm S}$ is the mass of the satellite, $v_{\rm S}$ is the velocity of the satellite, G is the gravitational constant, $\rho(<v_{\rm S})$ is the density of particles with a velocity lower than that of the satellite, and $\ln\lambda$ is the Coulomb logarithm.

The dynamical friction force therefore does not depend on the mass of the particles the satellite is travelling through, but depends only on the square of the satellite's mass. This means that the orbits of more massive satellites decay on shorter timescales than those of lower mass satellites, leading to "mass segregation", whereby more massive satellites are on average found closer to the cluster centre than their less massive counterparts.

The orbital decay time can be expressed as:

$$\tau_{\rm DF} = 1.2\frac{J_{\rm cir}r_{\rm cir}}{[GM_{\rm sat}/{\rm e}]\ln(M_{\rm halo}/M_{\rm sat})}\epsilon^{0.4}\,, \tag{1.18}$$

where $r_{\rm cir}$ and $J_{\rm cir}$ are the radius and initial orbital angular momentum of the circular orbit with the same energy as the actual orbit, and ϵ is the circularity of the orbit (Colpi et al., 1999). This timescale therefore depends on the ratio of the host halo and the satellite halo.

Tidal Stripping

Tidal stripping, in the context of galaxy evolution, is the removal of matter from the halo of satellite galaxies. The material is stripped away by the tidal forces exerted upon the satellite by

the more massive host halo. While this effect primarily strips dark matter from the halo of the satellite, satellites on orbits that pass near the centre of the host potential can experience strong tidal forces that can strip star forming gas and dust.

Tidal stripping was first discussed in the context of globular clusters by von Hoerner (1957a). While von Hoerner was discussing the stripping of stars, the same basic physics apply to the case of satellite galaxies. Some important quantities can be quickly derived by assuming the masses involved are point masses and the satellite is on a circular orbit. If the satellite galaxy has mass m and radius r, and is located a distance R from its host mass M, then the satellite experiences an acceleration due to the host that can be expressed as:

$$\vec{g} = \frac{GM}{R^2} \,. \tag{1.19}$$

Given that the satellite is not a point mass, the acceleration at the point of the satellite that is closest to the host center is:

$$\vec{g} = \frac{GM}{(R-r)^2} \,. \tag{1.20}$$

By combining the two, we arrive at the equation for the tidal acceleration at the edge of the satellite:

$$\vec{g}_{\rm tidal}(r) = \frac{GM}{R^2} - \frac{GM}{(R-r)^2} \tag{1.21}$$

If we assume that the separation between the satellite and the center of the host is much larger than the radius of the satellite ($R \gg r$), the equation approximates to:

$$\vec{g}_{\rm tidal}(r) \approx \frac{2GMr}{R^3} \tag{1.22}$$

If the following condition is met, then matter from the satellite will be stripped,

$$\frac{2GMr}{R^3} > \frac{Gm}{r^2} \,, \tag{1.23}$$

and solving for r results in the tidal stripping radius:

$$r_{\rm tidal} = R \left(\frac{m}{2M} \right)^{\frac{1}{3}} \,. \tag{1.24}$$

A more complex analytic derivation that assumes neither point mass potentials, nor circular orbits was carried out in Read et al. (2006a). In practice, tidal stripping is a physically complex problem and numerical simulations are utilized to predict the amount of matter that is stripped

as a function of various orbital parameters. van den Bosch et al. (2018) find that the fraction of stripped material can be written as

$$f_{\rm strip} = \exp[-1.65(\Delta E/|E_{\rm b}|)^{-0.44}] \tag{1.25}$$

where ΔE is the total energy injected into the subhalo during a radial orbit and $|E_{\rm b}|$ is the total binding energy of the initial subhalo. They find that for values of $\Delta E/|E_{\rm b}| = 1$, the subhalo is stripped of ~ 20 per cent of its mass, while for values of $\Delta E/|E_{\rm b}| = 100$, the subhalo loses ~ 80 per cent of its mass.

Drakos et al. (2017) carried out a set of simulations with varying satellite mass, host mass, orbit circularity, and pericentric distance, amongst other variables. They find that satellites in massive clusters ($M_{\rm host}/M_{\rm sat} = 300$) with more circular orbits and larger pericentric distances ($r_p/r_s = 50$, where r_s is the scale radius) have ~15% of their mass stripped after 1 orbit. For a satellite in the same host halo with a smaller pericentric distance ($r_p/r_s = 10$), ~70% of the mass was stripped after a single orbit. Satellites that pass nearer to the centre of the potential well of their hosts are therefore expected to be more tidally stripped. For satellites in lower mass environments ($M_{\rm host}/M_{\rm sat} = 10$) with pericentric distances of $r_p/r_s = 10$, less stripping is predicted than for satellites in high mass clusters. These satellites showed ~30% of their mass being stripped after their first orbit.

The topic of tidal stripping is discussed further in Chapter 3.

Ram Pressure Stripping

Ram pressure stripping is an effect that occurs as a galaxy joins a group or cluster environment. As the galaxy falls into the gravitational potential of the host system, it experiences the intracluster medium it passes through as a wind. If the wind is strong enough, it can overpower the infalling galaxy's gravitational potential and push the gas and dust out of it. This loss of gas and dust thereby removes some of the galaxy's star forming potential, thus causing a quenching.

This effect was first theorized by Gunn & Gott (1972b). They derive the following approximation for this ram pressure:

$$P_r \sim \rho_e v^2 \,, \tag{1.26}$$

where P_r is the pressure experienced by the infalling galaxy, ρ_e is the density of the intracluster medium, and v is the velocity of the infalling satellite. Therefore, the condition for which ram pressure stripping occurs is

$$P_r > 2\pi G \Sigma_s \Sigma_g \tag{1.27}$$

where G is the gravitational constant, Σ_s is the surface density of stars in the infalling galaxy, and Σ_g is the density of gas in the infalling galaxy.

This effect is directly observed in so called "Jellyfish galaxies" - galaxies with long tails of gas, dust, and knots of star formation trailing behind as it plunges into the host cluster. Some recent examples of such galaxies are Roberts et al. (2021a), Durret et al. (2021a), and Hodgson et al. (2021). Roberts et al. (2021a) and Durret et al. (2021a) are particularly interesting for galaxy evolution, as they analyze samples of 95 and 97 jellyfish galaxies and jellyfish galaxy candidates respectively. Smith et al. (2010) find that jellyfish galaxies are systematically oriented away from the direction of motion of the galaxy, indicating that this ram pressure stripping is particularly effective during first infall. Additionally, the jellyfish galaxies are preferentially located near to the cluster centre, where the ICM is most dense, and at high velocities, in agreement with theoretical expectations from ram pressure stripping. Durret et al. (2021a) find that 80% of their jellyfish galaxy sample consists of star forming galaxies.

Harassment

Galaxies situated in group and cluster environments interact with one another due to their close proximity. These interactions generally come in two forms:

- "Mergers", where the galaxies "collide" and result in a single larger galaxy.
- "Fly-bys", where two galaxies pass near each other at high speed, but do not merge.

In the case of mergers, one galaxy "cannibalizes" its neighbor, having the effect of disturbing the morphologies of the galaxies. Given that these mergers would be more likely to occur in high density regions, like rich galaxy clusters, this seemed like a natural explanation for why clusters tend to have an abundance of elliptical galaxies, while spirals are more likely to be found in the field. These direct mergers, however, are extremely rare compared to fly-bys (Moore et al., 1996a).

In the case of galactic fly-bys, these galaxies gravitationally perturb each other, thereby damaging the disk. This effect was first described by Richstone (1976), but when repeated is referred to as "harassment". The term "harassment" was first coined in Moore et al. (1996a), who explored this effect through simulations. In harassment, cluster galaxies pass within 50 kpc of one another at several thousand km s^{-1}. Through simulations of these clusters, Moore et al. (1996a) find that Milky Way-like galaxies in Coma-like clusters experience a fly-by once per Gyr. These repeated interactions have the effect of impulsively heating the disks of these cluster galaxies, increasing the energy of stars and dust within them and causing them to become less bound, and

therefore easier to tidally strip. This harassment can therefore be responsible for aiding in the mass loss of cluster galaxies. Even for stars that remain bound to the cluster galaxy, the heating due to harassment can transform a disk into spheroidal component.

Additional simulations by Moore et al. (1999) show that the morphologically transformative effect of galaxy harassment is much more effective at disrupting the structure of lower density disks, such as Sc and Sd disk galaxies in the Hubble classification system (Hubble, 1926). Denser spirals with shorter disk lengths (Sa and Sb) are more immune to the stripping and disruptive effects of harassment, but harassment still plays an important role in explaining the relative dearth of spiral galaxies in low redshift clusters.

All of the effects detailed in this section play some role in the evolution of galaxies as they transition from isolated field galaxies into satellite galaxies orbiting within host haloes in group and cluster environments. In the following section, we will discuss gravitational lensing - one of the primary ways to measure the distribution of dark matter in these haloes, and therefore one of the most powerful tools for studying some of these effects.

1.3 Gravitational Lensing

Gravitational lensing is the deflection of photons from distant background sources as they pass through the gravitational field of more nearby objects. This deflection results in a change in the shape and size of the background source, while the surface brightness is strictly conserved. By measuring these distant background sources, we can then learn something about the distribution of the matter in the foreground objects. Because the lensing is caused by both baryonic and dark matter, this technique is a powerful probe of things that are extraordinarily difficult to measure using other techniques.

The degree of the distortion splits the field of gravitational lensing studies into several subgroups. In *strong* gravitational lensing, the degree of distortion is high, and the background sources can be stretched and bent into large arcs, or even split into multiple distinct images, resulting in an effect that is clearly visible by eye. In *weak* gravitational lensing, the degree of distortion is much smaller. So while background sources are still stretched, the degree by which they're sheared is generally smaller than the ellipticity of a typical galaxy. This means that, in contrast with strong gravitational lensing, weak lensing results in observations that are much less obvious and requires the statistical analysis of many galaxies in order to confirm that any lensing has taken place at all. But because background sources being lensed by a massive foreground object are sheared tangentially with respect to a circle centred on the foreground object, correlations in the alignment of background galaxy shapes provide information on the

projected mass distribution of the lens. Finally, in gravitational *micro*lensing, the object being lensed is a point source, and no shearing is observed at all. In this case, the only observable is a sharp and sudden increase in brightness due to the magnification of the source's size as the source passes behind the foreground lens. All three regimes of gravitational lensing have proven very useful, as they can be used to probe different physical phenomena. However, given the topic of this thesis is weak gravitational lensing, strong and micro lensing will be ignored for the remainder of this discussion.

As mentioned above, weak gravitational lensing alters the observed shape of a background source by a degree that is typically much smaller than that object's intrinsic ellipticity. If all galaxies in the universe were perfectly circular, this would cause no issues as the measurement of a galaxy's ellipticity would then be a direct measurement of its shear. Unfortunately, most galaxies are elliptical when projected onto the two dimensional plane of the sky, and that intrinsic ellipticity makes the measurement of shear much more difficult. This problem of galaxies being naturally elliptical is often called *shape noise*. This shape noise is dealt with by observing many thousands of galaxies and determining if there is a statistical correlation in their shapes. This approach works by making the assumption that galaxy shapes should be randomly oriented across the sky. Therefore any correlation in their observed shapes must be due to gravitational lensing. This assumption does not always hold true, however, as the tidal gravitational field of the large scale structure of the universe can induce correlations in the distribution of galaxy shapes. This effect, known as *intrinsic alignment*, is a very important consideration for certain applications of weak gravitational lensing, such as cosmic shear - the lensing caused by the large scale structure. Other applications of weak lensing, however, rely on the stacking of many objects, whose shear contribution may individually be too small to measure, on top of one another to study the mean properties of these lenses as a population. By stacking all of these lenses together, any intrinsic alignment from a single lens is washed out by the contributions from the rest of the stack.

This form of weak gravitational lensing, where many objects of a similar type are stacked together is frequently used to study objects like galaxy clusters, galaxy groups, or even just galaxies. These cases are generally referred to as *cluster lensing* and *galaxy-galaxy lensing*, and are further explored in Chapters 2 and 3.

Because it is the distant background objects that carry the information, weak lensing measurements are improved by increasing the number of background sources. There are two primary ways to do this: one can observe a given region of space for a longer time allowing fainter galaxies to become detectable, or one can observe a larger region of the sky. Both approaches have their drawbacks.

By using fainter sources, which are often smaller, the sources are more strongly impacted by the distortion of their light passing through the atmosphere. The atmosphere acts to blur the

light from the background source, which circularizes its observed shape and destroys some of the information we were hoping to gain from these additional sources. By observing fainter galaxies, one is also increasing the number density of sources on the sky. This leads to an increase in *blended sources*, objects which overlap with one another on the sky. Object detection algorithms cannot always reliably separate such combinations of sources, and measuring the shape of two or more objects as if it were a single object can bias results. These topics are explored further in Chapter 4.

The alternative approach to increasing the number of background sources is to observe a larger region of the sky. While this solves the complications associated with looking deeper, it comes with the complication that a much larger set of data must be processed and analysed. This can be quite computationally expensive and time consuming. Issues with dealing with large data sets are explored in Chapter 4 and Appendix A.

1.3.1 Gravitational Lensing Formalism

Here, I will provide a brief overview of the derivation of equations which define the deflection of photons around massive bodies. A more complete derivation can be found in Blandford & Narayan (1986).

Consider a simple lensing scenario. There is a massive lensing object, located some angular diameter distance d_l from the observer, and a background source at a larger angular diameter distance d_s. Both the lens and the source are positioned near each other on the sky. While in reality photons emitted by the background source are smoothly curved around the lens, for most astrophysical sources, we can replace that smooth curvature with two simple lines that form an angle α (Figure 1.1). This deflection angle is defined as:

$$\hat{\alpha} = \frac{4GM}{c^2 \xi} \tag{1.28}$$

where M is the mass of the lens, G is the gravitational constant, and ξ is the impact parameter between the photon and the lens plane. This equation holds for impact parameters that are much larger than the Schwarzschild radius of the lens ($\xi \gg R_s \equiv 2GMc^{-2}$).

We can then define the two dimensional position of the source, η as

$$\eta = \frac{d_\mathrm{s}}{d_\mathrm{l}} \xi - d_\mathrm{ls} \hat{\alpha}(\xi) \, . \tag{1.29}$$

Changing to angular coordinates ($\eta = d_\mathrm{s}\beta$, $\xi = d_\mathrm{l}\theta$) yields the "lens equation"

$$\beta = \theta - \frac{d_\mathrm{ls}}{d_\mathrm{s}} \hat{\alpha}(d_\mathrm{l}\theta) \equiv \theta - \alpha(\theta) \tag{1.30}$$

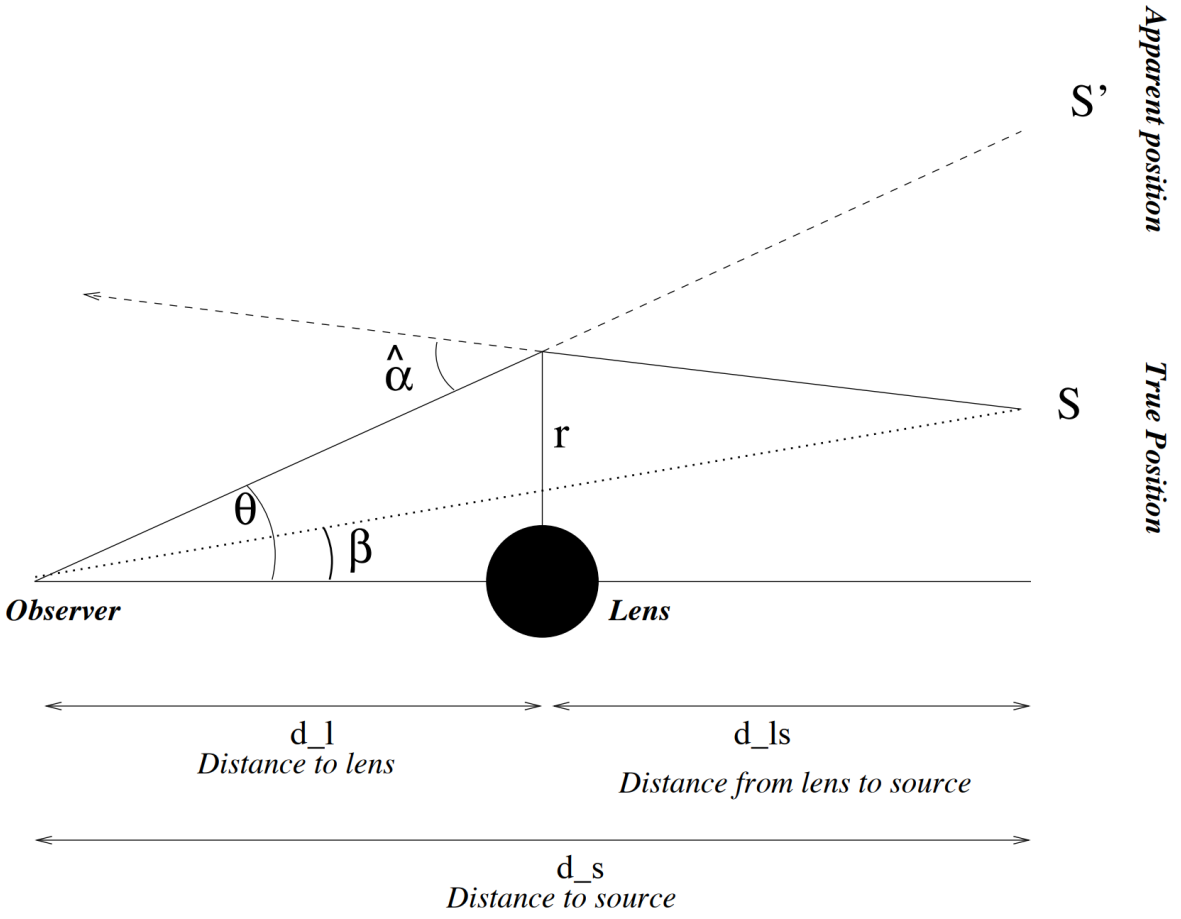

Figure 1.1: A schematic of gravitational lensing geometry. A lens and source lie an angle β from one another on the sky, but at separate angular diameter distances d_l and d_s. Photons from the source are smoothly curved around the lens. However, we can replace the smooth curve by considering two lines which form an angle α, the deflection angle. Figure courtesy of M. Hudson.

where the reduced deflection angle is defined as $\alpha(\theta) \equiv \frac{d_{ls}}{d_s}\hat{\alpha}(d_l\theta)$. Sources which, in reality, are located at β are therefore observed on the sky at angular position θ. It should be noted here that this equation can have multiple solutions, and therefore a single source can be observed at multiple locations on the sky. Lenses causing this phenomenon are called strong lenses.

The boundary between strong and weak lensing can be defined using

$$\kappa(\theta) = \frac{\Sigma(d_l\theta)}{\Sigma_{cr}} . \tag{1.31}$$

Here, $\kappa(\theta)$ is the dimensionless surface mass density known as the convergence in gravitational lensing theory. The critical surface mass density Σ_{cr} is defined as

$$\Sigma_{cr} \equiv \frac{c^2}{4\pi G}\frac{d_s}{d_l d_{ls}} . \tag{1.32}$$

If $\kappa \geq 1$, the surface mass density at θ exceeds the critical surface mass density, and the lensing is strong (multiple images and large arcs). If $\kappa < 1$, then the surface mass density at θ is below the critical surface mass density, and these strong lensing features are not produced. κ therefore defines the edge dividing strong and weak lensing. Because κ depends on the angular position θ, a sufficiently massive lens can produce both strong and weak lensing at different angular positions. In such cases, strong lensing features are generally observed near the centre of the lens where the surface mass density is greatest, and weak lensing features are observed at larger radii where the surface mass density is lower.

For point sources, the lens equation implies a simple shifting in the observed position. However, for extended sources such as galaxies, the index of refraction is variable, and the photons are deflected differentially. Therefore, extended sources are not merely shifted, but are distorted as well. One can solve for the observed shape of the distorted source by evaluating the lens equation (Equation 1.30) at all points. Or, by assuming that the background extended source is much smaller than the foreground lens, the change to the source can be described by the Jacobi matrix

$$A(\theta) = \frac{\partial\beta}{\partial\theta} = \left(\delta_{ij} - \frac{\partial^2\psi(\theta)}{\partial\theta_i\partial\theta_j}\right) = \begin{pmatrix} 1-\kappa-\gamma_1 & -\gamma_2 \\ -\gamma_2 & 1-\kappa+\gamma_1 \end{pmatrix} . \tag{1.33}$$

Here, $\psi(\theta)$ is the two dimensional gravitational potential of the lens, and γ is the two component shear, which can be expressed as a complex number ($\gamma \equiv \gamma_1 + i\gamma_2 = |\gamma|e^{2i\phi}$). In the case of weak gravitational lensing, this Jacobi matrix approaches the unit matrix and $\kappa \ll 1$. Therefore, the deflection of light is quite small, and the background sources are only sheared slightly from their original shape.

For cluster and galaxy-galaxy lensing, what's measured is an object's shear with respect to the vector connecting the background source to the centre of the foreground lens. In this scenario, we can break the shear into tangential and cross components

$$\begin{pmatrix} \gamma_t \\ \gamma_x \end{pmatrix} = \begin{pmatrix} -\cos 2\phi & -\sin 2\phi \\ \sin 2\phi & -\cos 2\phi \end{pmatrix} \begin{pmatrix} \gamma_1 \\ \gamma_2 \end{pmatrix} \tag{1.34}$$

where ϕ is the azimuthal angle of the lens-source vector. The excess surface mass density of the lens can then be calculated as

$$\Delta\Sigma \equiv \overline{\Sigma}(<R) - \Sigma(R) = \gamma_t \Sigma_{cr} \tag{1.35}$$

where Σ_{cr} is the critical surface density defined by Equation 1.32. The mass of the lens can then be estimated by assuming a mass model, converting it to a $\Delta\Sigma$ profile, and comparing it to the $\Delta\Sigma$ signal measured around the lens. This process is covered in more detail for clusters, groups, and satellite galaxies in Chapters 2 and 3.

1.3.2 First Observations

Published material on the subject of gravitational lensing using Newtonian physics dates all the way back to von Soldner (1804). However, the modern theory of gravitational lensing begins with Einstein's theory of relativity which predicts a larger degree of lensing than expected from Newtonian physics due to the additional effect of temporal distortion by the lens. While Einstein wrote unpublished letters on the effect of a massive body deflecting photons as early as 1912, it wasn't until Einstein (1916) that he published work on the topic. Despite the unpublished nature of Einstein's early thoughts on the topic, he would not have to wait long for the first set of observations to help confirm his theory. Dyson et al. (1920) took advantage of a solar eclipse to observe stars near the sun's position on the sky. They noted that the relative location of the stars during the eclipse shifted as their photons were deflected by the gravitational field of the sun.

It wasn't until decades later that the first strong lenses were discovered. Walsh et al. (1979) marks the first time that an object was observed to be multiply imaged. The object, the so-called "Twin QSO", was a distant quasar which appeared in two nearby locations on the night sky. The first giant arcs were later detected around the cluster Abell 370 by Soucail et al. (1987). The following year, Fort et al. (1988) reported the detection of less extremely distorted objects in the vicinity of Abell 370 that were dubbed "arclets".

While the discovery of these arclets was promising, observations of weak gravitational lensing were still a couple years away. It wasn't until advances were made in imaging technologies that

data would be sufficiently deep and PSF effects could be corrected for. Indeed, early attempts to measure weak gravitational lensing were made on photographic plates by Tyson et al. (1984), but it wasn't until CCDs were introduced that a successful detection of the effect would be made. Tyson et al. (1990) found a correlation in the shapes of background galaxies around the massive galaxy clusters A1689 and CL 1409+52.

This detection would continue to drive the further development of techniques for observing and measuring weak gravitational lensing. Kaiser & Squires (1993) developed a theoretical framework for converting these correlations in background galaxy shapes to a parameter free projected map of the matter distribution in the lenses. Additionally, Kaiser et al. (1995) describes a technique for more accurately determining the shapes of small, faint, background galaxies upon which weak lensing measurements depend.

Due to the growing relevance of weak lensing studies, more time and money were allocated to the topic. This led directly to the growth of large surveys which would yield much more robust results.

1.3.3 Modern Weak Gravitational Lensing

Technological advances in observational astronomy since the early days of weak gravitational lensing have enabled dedicated surveys. These surveys cover large fields of the sky, obtaining deep photometry for millions of galaxies.

CFHTLS took observations from 2003 to 2008, covering 150 square degrees of the sky with a sub-arcsecond mean image quality and a mean r-band limiting magnitude of 25[1]. The larger footprint of the survey greatly increases the number of background sources, which enables the probing of lower mass objects. Using data from CFHTLenS[2] the dark matter dominated filaments that connect dark matter haloes were detected for the first time using weak gravitational lensing (Epps & Hudson, 2017). While measurements of the cosmic shear, the weak lensing induced by the large scale structure of the universe, had been made prior to CFHTLS (Bacon et al. 2000, Kaiser et al. 2000, Van Waerbeke et al. 2000, Wittman et al. 2000), the survey facilitated measurements of cosmic shear with greater precision, resulting in measurements of the cosmological parameters σ_8 and w_0, the variance in the cosmic matter density field on scales of 8 h^{-1}Mpc, and the dark energy equation of state parameter respectively (Hoekstra et al., 2006). Additionally, a measurement of the cluster mass-richness relation was made which relates the number of satellites in the cluster (richness) to its mass (Ford et al., 2014). Because σ_8 essentially

[1]https://www.cfht.hawaii.edu/Science/CFHLS/T0007/

[2]https://www.cfhtlens.org/

describes how "clumpy" the matter distribution in the universe is, the observed cluster mass function can be used to constrain σ_8. This requires mass estimates for clusters, which is made possible via the mass-richness relation.

The Kilo-Degree Survey (KiDS) began in 2011 and covers over 1,000 square degrees in 9 bands[3]. The improvements over previous surveys allowed for even more precise measurements on cosmological parameters. This, however, revealed a significant discrepancy between measurements of cosmological parameters measured at low redshifts (Hildebrandt et al., 2017) and those measured from the CMB (Planck Collaboration et al., 2020). The measurement of σ_8 made by KiDS, while in agreement with measurements made by other cosmic shear analyses, disagrees with the measurement made by Planck by more than 2σ. Local measurements of the parameter indicate that matter in the universe is more smoothly distributed than the Planck measurement, which challenges the predictions of the ΛCDM cosmological model.

The Dark Energy Survey (DES)[4] is a survey that began in 2013 and covers 5,000 square degrees of the sky in the $grizY$ bands down to an i-band depth of 23 with a S/N of 10 (Sevilla-Noarbe et al., 2021). As the name suggests, one of the primary science goals of DES is to probe the nature of dark energy. DES, in contrast with KiDS, finds agreement with the prediction of cosmological parameters from Planck by measuring the cosmic shear with the 100 million source galaxies in the catalogue (DES Collaboration et al., 2021), easing the tension between low and high redshift measurements of cosmological parameters.

The Ultraviolet Near-Infrared Optical Northern Survey (UNIONS) is a survey that is currently underway, and which will eventually cover 5,000 square degrees of the sky in the u, g, r, i, and z bands. The Canada-France Imaging Survey (CFIS)[5] is providing the u and r band data, which is taken by the wide field imager MegaCam, with a field of view of 1 square degree. The r-band data, which reach a depth of 24.1 magnitudes for a point source in a 2 arcsecond aperture at 10 σ (25.3 magnitudes at 5 σ), is being used as a weak lensing survey. A primary advantage that CFIS/UNIONS has over DES, is that it overlaps with SDSS[6], providing a vast catalogue of spectroscopic information across its footprint. This enables a lot of weak lensing science, as there already exist many catalogues of clusters and groups which can be analyzed. For a review of the first results from a preliminary set of the first 1,500 square degrees of data, see Chapters 2 and 3.

[3] http://kids.strw.leidenuniv.nl/index.php
[4] http://www.darkenergysurvey.org
[5] https://www.cfht.hawaii.edu/Science/CFIS/
[6] https://www.sdss.org/

Future

With many cosmological tensions and questions that are yet to be resolved, there are many surveys planned to start in the coming decade that aim to address them. The Legacy Survey of Space and Time (LSST)[7] at the Vera C. Rubin Observatory is set to start in 2023 and will use an 8.4 meter telescope with a 9.6 square degree field of view (Ivezić et al., 2019). The field of view will produce about 20 TB of data per night, and will enable LSST to observe the visible sky in the $ugrizy$ bands every few nights. By the end of the survey's 10 year duration, it will reach 18,000 square degrees at an r-band depth of 27.5 (5σ point source depth) and will have observed 20 billion galaxies and resolved 17 billion stars, resulting in a total catalogue size of 15 PB. This enormous amount of data is orders of magnitude larger than any currently operating weak lensing survey.

There are also surveys planned which will bypass the problems associated with ground based observing by using space telescopes. The first of these is Euclid, a 6 year mission by the European Space Agency (ESA) set to launch in late 2022 (Laureijs et al., 2012). Euclid is equipped with a 1.2 meter telescope with two 0.53 square degree field of view instruments, the visible imager (VIS) which will reach a limiting magnitude of 24.5 (10σ extended), and the Near Infrared Spectro-Photometer (NISP) which will reach a limiting magnitude of 24 (5σ point-like). It will observe 15,000 square degrees of the sky from the L2 Sun-Earth Lagrangian point[8]. Euclid aims to measure shapes for more than a billion galaxies.

The Roman Space Telescope, formerly called the Wide-Field Infrared Survey Telescope (WFIRST), is a NASA mission set to launch no later than 2027[9]. Roman is equipped with a 2.4 meter telescope with a 0.28 square degree field of view (Spergel et al., 2013). Over the course of 2.4 years, it will survey 2,000 square degrees to an $YJHF184$-band depths of 27 (5σ point source). One of the primary differences between Roman and Euclid is that Roman is an infrared telescope, while Euclid operates in the visible spectrum to obtain photometry for the purposes of measuring shapes, but also extends into the near infrared to be able to precisely measure photometric redshifts.

All of these telescopes support additional science goals (baryonic acoustic oscillations, supernovae, and exoplanets, for example), but given the preponderance of telescopes and surveys that are being designed with weak lensing as a core science motivation, weak lensing will be one of the primary probes of the nature of dark matter and dark energy in the coming decades.

[7] http://lsst.org
[8] https://www.euclid-ec.org/
[9] https://roman.gsfc.nasa.gov/

1.4 Shape Measurement

Shape measurement plays a fundamental role in weak lensing observations. Our ability to measure a weak lensing signal depends on our ability to extract shape information from the data. Modern surveys aiming to measure the weak lensing signal induced by the large scale structure of the universe (cosmic shear) demand that the systematics be reduced below the 1% level (e.g. Cardone et al. 2014). This is not a simple requirement to achieve. Because the galaxies whose shapes have been distorted are background galaxies, these objects tend to be very faint, with r-band magnitudes extending beyond 24. This means the images of these objects are quite noisy. Additionally, these galaxies are very small and in some cases subtend only a few pixels. The light from these distant background sources also passes through the Earth's atmosphere (for ground-based surveys). The atmosphere has the effect of circularizing the observed shape of the galaxy. To undo this effect, the point spread function (PSF), which describes how the light from a point source is distorted by the atmosphere, must be estimated at the location of the object on the sky, then the shape and the PSF must be deconvolved in an attempt to recover some of the lost shape information. Finally, the photons are discretized onto a charge-coupled device (CCD), resulting in the final faint, small, noisy, blurry, and pixelized observation of the galaxy whose shape must be measured.

Given the difficulty of measuring these galaxy shapes and the demand to do so accurately, shape measurement and bias estimation in the weak lensing community is a quite active topic. Here, I will provide a brief overview of the current state of this topic. I will discuss the most popular methods of measuring shapes (Sections 1.4.1 and 1.4.2), the various challenges that have driven the development of shape measurement techniques (Section 1.4.3), and how biases are corrected for after the shapes have been measured (Section 1.4.4).

1.4.1 Moments Based Approach

Noting that the alternative of using isophotal radii is extremely difficult due to the faint nature of the background sources, Tyson et al. (1984) developed a method for measuring galaxy shapes using the second moment of their intensity distributions. The central moments are defined as

$$M_{i,j} = \sum (x - \overline{x})^i (y - \overline{y})^j [b(x, y) - b_s] / \sum [b(x, y) - b_s] \tag{1.36}$$

where $\overline{x}$ and $\overline{y}$ represent the location of the object's centroid, $b(x, y)$ is the intensity distribution, b_s is the sky intensity, and x and y are the pixel coordinates. The second moments (M_{20}, M_{02}, and M_{11}), which are sensitive to the less elliptical inner regions of the source and therefore less sensitive to the noisier but more elliptical outer regions, are then computed along two axes: the

radial axis r connecting the lens to the background source, and the orthogonal axis θ. This results in

$$M_r = M_{20}\cos^2\phi + M_{02}\sin^2\phi + 2M_{11}\sin\phi\cos\phi \tag{1.37}$$

$$M_\theta = M_{20}\sin^2\phi + M_{02}\cos^2\phi + 2M_{11}\sin\phi\cos\phi \tag{1.38}$$

where ϕ represents the angle between the radial axis and the arbitrarily selected x axis. Tyson et al. (1984) then defines a dimensionless image distortion statistic

$$\mathcal{D} \equiv \psi(M_r - M_\theta)/(M_r + M_\theta) \tag{1.39}$$

where $\psi = b/D$ is the ratio of the impact parameter of the light ray to the distance of the lens.

While overly simplistic (this approach neglects corrections for the distortions made by the atmosphere and the instrument), this set the foundations for more sophisticated moments-based methods.

Kaiser et al. (1995) (KSB) advanced this technique by incorporating the effects of anisotropic instrumental PSFs. KSB use the weighted quadrupole moments

$$Q_{ij} \equiv \int d^2\theta W(\theta)\theta_i\theta_j f(\vec{\theta}) \tag{1.40}$$

where $W(\theta)$ is a Gaussian window function with a scale length defined to be some multiple of the measured background object. The polarisation is then defined as

$$e_\alpha \equiv Q_\alpha/T \tag{1.41}$$

where

$$\begin{aligned} Q_1 &\equiv Q_{11} - Q_{22} \\ Q_2 &\equiv Q_{21} \\ T &\equiv Q_{11} + Q_{22}\,. \end{aligned} \tag{1.42}$$

If one were using unweighted moments, the relation between the change in polarisation and shear is simply $\langle \delta e_\alpha \rangle = 2\gamma_\alpha$. However, given the use of weighted moments to mitigate the effect of noise, this simple relation no longer holds. Instead, KSB introduce the shear polarizability tensor, $P^\gamma_{\alpha\beta}$, such that

$$\delta e_\alpha = P^\gamma_{\alpha\beta}\gamma_\beta\,. \tag{1.43}$$

Similarly, to account for the atmospheric smearing, KSB introduce a smear polarizability tensor, $P^s_{\alpha\beta}$, such that

$$\delta e_\alpha = P^s_{\alpha\beta}p_\beta \tag{1.44}$$

where p_β represents a measurement of the PSF anisotropy. Both polarizability tensors are measurable from the higher weighted moments of the observed galaxies and PSFs. While imperfect, the KSB technique has remained as one of the key methodologies for estimating the shapes of galaxies in weak lensing surveys. It does not meet the $< 1\%$ bias level required for cosmic shear measurements as the shapes can be biased (especially for small galaxies which can be dominated by the PSF smearing), though it can achieve this level of accuracy through additional calibration.

1.4.2 Model Based Approach

Model fitting to estimate galaxy shapes is an alternative to the moments based methods that was first discussed in Kuijken (1999). Kuijken acknowledges that the weaker and weaker signals sought to be measured over time demand an algorithm that is less biased than the moments based measurements that came before. To this end, Kuijken proposes an algorithm that essentially involves averaging the galaxy profiles then fitting this profile with a model, resulting in a measurement of the averaged shear.

Bridle et al. (2002) expand on this concept by fitting individual galaxies with combinations of Gaussian profiles which are summed and convolved with a PSF. A Markov Chain Monte-Carlo (MCMC) algorithm is used to find the best fitting parameters for each of the galaxies. A Monte-Carlo based approach comes with the benefit of providing an uncertainty estimate for the galaxy shapes, something that is quite difficult to estimate with moments based measurement techniques.

However, galaxy surface brightness profiles are not necessarily well described by Gaussian profiles. The use of alternative prescriptions, such as de Vaucouleurs and exponential profiles, is explored with the $lensfit$ algorithm as described in Miller et al. (2007b). This algorithm was tested on a set of simulations, which showed that $lensfit$ was accurate enough that it need not be additionally calibrated. As simulations increased in complexity, however, it was later shown that regardless of whether one uses a model fitting or a moments based shape measurement approach, some additional bias calibration is needed (see section 1.4.3).

Model fitting has the benefit of being less biased, whereas moments based techniques are computationally faster, which is advantageous for large weak lensing surveys with millions of galaxies. In practice, both methods are still used, and neither is demonstrably superior to the other.

1.4.3 Comparisons

Given the large number of implementations of shape measurement algorithms and the growth of weak lensing surveys with a high demand for accuracy, the weak lensing community began organizing shape measurement challenges which could be used to quantitatively compare the accuracy and efficiency of these shape measurement strategies.

The first such challenge was the "Shear TEsting Programme" (STEP) (Heymans et al., 2006a), which was then succeeded by STEP2 (Massey et al., 2007). This was then followed up by the "GRavitational lEnsing Accuracy Testing" (GREAT) challenges: GREAT08 (Bridle et al., 2010), GREAT10 (Kitching et al., 2010), and GREAT3 (Mandelbaum et al., 2014).

The challenges generally consist of a set of simulated galaxy observations with known shapes. These data sets are then processed by each of the algorithms that had been submitted to the challenges. The results could then be directly compared to the applied shears to examine the advantages and disadvantages of each shape measurement technique.

The initial STEP challenge modeled galaxies as a de Vaucouleurs bulge with an exponential disc that were convolved with simulated PSFs which included effects like atmospheric turbulence. The galaxies were then placed on the image in such a way that they could blend with one another, which required algorithms to detect the galaxies in addition to measuring their shape. The shears and PSFs were constant across any given image. For STEP2, the complexity was increased, and the simulated galaxies contained substructure to make the shapes more realistic.

GREAT08 employed a more simple strategy than STEP, in order to allow the challenge to focus solely on shape measurement rather than detection. GREAT08 used a bulge and disc profile for the galaxies, and PSFs were modeled with Moffat profiles. The galaxies were then placed uniformly onto a grid, which eliminated blended sources and removed the detection phase.

GREAT10 increased the realism of the simulations by introducing shears and PSFs that varied across the field, as they do in real observations. GREAT3 improved the realism in 3 key ways. First, it used real galaxy images from the HST COSMOS survey, rather than simplified parametric surface brightness profiles. Second, it reintroduced complex PSFs that vary across the field, and included effects from atmospheric and telescope distortion. Finally, it introduced multi-epoch data. Real weak lensing survey data often includes multiple dithers of the same field. These dithers can then be stacked to provide a single image with a higher signal to noise ratio but a galaxy profile which has been averaged (including the distorting effects of the PSF), or the dithers can be fit individually. The galaxies, however, remained gridded and just the shape measurement was being tested. Additionally, GREAT3 produced several branches of the simulations with varying parameters. Some branches included spatial variation in shear and PSF, while other branches

held those parameters as fixed. Some branches were intended to simulate ground based data, while others were intended to simulate the space based observations of upcoming surveys.

The results revealed a lot of complexity (Mandelbaum et al., 2015). Some algorithms fared well in variable shear branches, but showed poorer performance when the shear was fixed. Some algorithms showed a performance that varied greatly depending on the weighting scheme used. Ultimately, model based fitting approaches showed a more favorable performance, but still suffered from certain biases. Notably, the choice of which pixels to fit can induce a so-called "truncation bias" which can be up to several percent, above the required threshold for cosmic shear analyses. There is also a bias depending on how the algorithms choose to model the source galaxies. The bias introduced by using real galaxy images appears to have a more significant impact on the space based branches than the ground based branches.

1.4.4 Bias Correction

The shape measurement challenges revealed that simulations must accurately represent the survey in order to capture the most significant biases. To this end, surveys typically employ simulations targeted specifically to the survey specifications in order to calibrate the weak lensing catalogues.

KiDS, for example, developed the "Simulations Code for Heuristic Optimization of *lens*fit for the Kilo Degree Survey" (SCHOo*l* for KiDS) simulations. The simulations were made to match the footprint, noise, seeing, and PSF properties of the KiDS survey. Galaxy properties were selected from the GEMS (Rix et al., 2004) and UVUDF (Rafelski et al., 2015) catalogues in order to match the magnitude distribution of sources to that of KiDS. The simulated galaxies were modelled with a linear combination of a de Vaucouleur bulge and an exponential disk, with 10% of galaxies specified as bulge-only. The sizes of the disks were drawn randomly from a distribution

$$P(r) \propto r\exp(-(r/A)^{4/3}) \tag{1.45}$$

where $A = r_{\rm median}/1.13$ and $r_{\rm median} = \exp(-1.31 - 0.27(m_r - 23))$.

Each galaxy is included 4 times in the simulated survey. Each duplicate is rotated by an additional 45° to cancel the effects of shape noise.

Stars were added as Moffat profiles with size and ellipticity distributions that closely resemble those of KiDS. The stars and galaxies were then distributed randomly throughout the simulated survey footprint. The random distribution allows for the blending between two or more sources, which can affect shape measurement bias. Each region of the simulation is then reproduced eight times, each with a different shear being applied to all of the galaxies. The sheared galaxies were then convolved with the simulated PSFs which were constant across the

field of a single observation. Finally, Gaussian background noise was added to complete the simulated observations.

The simulations were then run through the lensing pipeline, which used *lens*fit (Miller et al., 2013), a Bayesian model fitting algorithm, as its shape measurement component. The results showed that the *lens*fit algorithm had a ∼2% multiplicative bias, greater than the ∼1% requirement for cosmic shear. Because the simulations were specifically tailored for KiDS, the measured multiplicative and additive biases could be directly applied to the shape catalogues produced by running the lensing pipeline on the real KiDS data.

Fenech Conti et al. (2017) also note that the selection bias is roughly equivalent to the shape measurement bias. The selection bias here refers to the fact that galaxies are more easily identifiable if they are elliptical. Therefore, objects whose ellipticity aligns with the shear (and are therefore more elongated) are more likely to be identified as galaxies than objects whose ellipticity is anti-aligned with the shear (and are therefore circularized). The circularized (anti-aligned) objects are more likely to be identified as stars, and thus removed from the analysis. Because the GREAT shape measurement challenges omitted the object detection and classification phases from the process, they were blind to this particular selection bias. Therefore, even lensing pipelines which use algorithms with a sub-1% multiplicative bias in the GREAT challenge need to be calibrated.

The simulations of Fenech Conti et al. (2017) were later revisited by Kannawadi et al. (2019). Several minor improvements were made to SCHOo*l* for KiDS, and the resulting pipeline was redubbed the "COSMOS-like lensing emulation of ground experiments" (COllege). The primary improvement is the use of the COSMOS catalogue (Griffith et al., 2012) as the input for galaxy properties, rather than relying on parameterizations. In addition to ensuring the properties (magnitude, size, ellipticity, etc) are realistic, the galaxies are placed on the image in the same locations as the COSMOS sources. Because galaxies are not randomly distributed in the universe, the SCHOo*l* simulations underestimate the amount of clustering, which in turn underrepresents the number of blended sources in the final simulations. The use of COSMOS also allows photometric redshift estimates from the catalogue to be applied to sources in the simulations. This enables tomographic bias calibration which improves the tomographic cosmic shear analysis.

Another approach to shape measurement bias calibration that has become more popular in recent years is METACALIBRATION (Huff & Mandelbaum, 2017). METACALIBRATION is distinct from simulations in that it only requires the actual survey data itself. METACLIBRATION applies a series of multiplicative shears to the survey data. The measurement process is then applied to the versions which have been sheared by some known positive and negative amounts. By measuring

all versions of the data, what's being measured is the *response* to the applied shear, R.

$$R = \frac{\partial e}{\partial \gamma} \tag{1.46}$$

Here e is the two-component ellipticity of the measured objects, and γ is the shear. The two-component ellipticity is defined as:

$$(e_1, e_2) = \frac{1 - q^2}{1 + q^2}(\cos 2\theta, \sin 2\theta) \tag{1.47}$$

where q is the minor-to-major axis ratio and θ is the position angle with respect to the x axis in pixel coordinates.

To show how this response relates back to the original shear, Sheldon & Huff (2017) starts with a noisy estimate of the two-component ellipticity for an object, $e = (e_1, e_2)$. This can be Taylor expanded around zero shear, $\gamma = 0$

$$e = e|_{\gamma=0} + \left.\frac{\partial e}{\partial \gamma}\right|_{\gamma=0} \gamma + ... \equiv e|_{\gamma=0} + R\gamma + ... \tag{1.48}$$

Assuming shear is small and the galaxies are randomly oriented, $\langle e \rangle|_{\gamma=0} \sim (0, 0)$, the ensemble mean of e can be expressed as

$$\langle e \rangle = \langle e \rangle|_{\gamma=0} + \langle R\gamma \rangle \approx \langle R\gamma \rangle \,. \tag{1.49}$$

The response, R, is estimated for each object in the catalogue, and so the ensemble shear can be expressed as

$$\langle \gamma \rangle \approx \langle R \rangle^{-1} \langle e \rangle \approx \langle R \rangle^{-1} \langle R\gamma \rangle \,. \tag{1.50}$$

Because both e and γ have two components, R is a 2 x 2 matrix. METACALIBRATION forms an estimate of R by measuring e on the sheared versions of the data to compute a finite-difference central derivative

$$R_{i,j} = \frac{e_i^+ - e_i^-}{\Delta\gamma_j} \tag{1.51}$$

where $\Delta\gamma = 2\gamma$.

Excluded from the METACLIBRATION discussion so far is the means of actually measuring the shapes. This is because METACALIBRATION is a shape measurement algorithm agnostic calibration technique. Any reasonably well behaved shape measurement algorithm can be plugged into the METACALIBRATION framework.

METACALIBRATION has been shown to be effective at reducing measurement and selection biases in GREAT3 data, achieving the one part in a thousand accuracy required for cosmological studies (Sheldon & Huff, 2017). However, its performance remains to be seen when applied to real wide field survey data.

The topic of simulations for the purpose of weak lensing calibration is further explored in the context of the CFIS/UNIONS weak lensing survey in Chapter 4.

1.5 Outline of the thesis

This thesis will cover a variety of topics related to the CFIS/UNIONS weak lensing survey. In Chapter 2, clusters and group centrals will be analyzed using a shape catalogue created from a preliminary version of the CFIS-*r* band data. The distribution of source redshifts, an important component for converting shape correlations into weak lensing signals, is estimated despite the survey's lack of photometric or spectroscopic redshifts. The cluster mass-richness relation is then calculated using the redMaPPer cluster catalogue. Finally, weak lensing masses are measured for both red and blue group centrals as a function of their stellar mass. The two populations display a bimodality in halo masses for a fixed stellar mass.

Chapter 3 uses the same preliminary weak lensing catalogue to analyze the signal around satellite galaxies orbiting in galaxy groups. A mean satellite subhalo mass is determined for satellite galaxies living in groups with 5 or more members. Observations show that satellites in more massive galaxy clusters are subject to tidal stripping, and simulations predict this occurs in galaxy groups as well. Tidal stripping is thought to play a role in the quenching of star formation in satellites. We attempt to measure tidal stripping in these galaxy groups by binning the satellites by their projected separation from the group centre and measuring their subhalo masses. If stripping occurs, we expect to see a declining subhalo-to-stellar mass ratio as satellites get closer to the group centre, as tidal forces are strongest there.

Chapter 4 reviews the work done so far to calibrate the early CFIS-*r* shape catalogues. The simulations framework is described, and early multiplicative and additive bias corrections are derived. Analyses of the uncalibrated shapes in the survey are also shown.

Finally, Appendix A discusses a public, online, web-based tool for weak lensing analysis named "Weak Lensing for the Masses". Users input a list of lenses (right ascensions, declinations, and redshifts) and select a publicly available shape catalogue. The tool then calculates and returns via email the $\Delta\Sigma$ signal. The overall architecture and lensing pipeline are described, and a brief comparison to published results is shown.

Chapter 2

Galaxy group and cluster masses from weak lensing in UNIONS

2.1 Introduction

Clusters of galaxies, the most massive collapsed structures in the universe, serve as a useful probe for cosmological measurements. Cluster number counts trace the growth of large scale structure over time. They have been used as a probe of the matter density parameter $\Omega_{\rm m}$ and the density power-spectrum normalisation σ_8 (see, e.g., Carlberg et al., 1997, Allen et al., 2011). Uncertainty in the measurement of these two parameters is no longer dominated by low number statistics, but by uncertainties in mass estimates (Planck Collaboration et al., 2014).

There are multiple techniques for measuring cluster masses. For sufficiently massive clusters, the intracluster medium becomes hot enough to emit X-rays via *bremsstrahlung* radiation (Böhringer et al., 2000). The Sunyaev & Zeldovich (1972) effect is another probe of cluster mass (Bleem et al., 2015).

Another technique for measuring the masses of clusters is weak gravitational lensing. Weak gravitational lensing is the slight distortion in the observed shape of background galaxies as their photons travel through the gravitational potential of more nearby structures along the line of sight. This effect is a probe of the distribution of matter, both baryonic and dark, in the cluster.

Galaxy clusters and groups are detected from optical and spectroscopic data in a variety of techniques. In photometric surveys, clusters can be detected by looking for overdensities of red galaxies. This technique was applied to the SDSS DR8 data set (Aihara et al., 2011) to produce the redMaPPer cluster catalogue (Rykoff et al., 2014). redMaPPer then utilizes the mass-richness

relation, the relation between the number of cluster members and its mass, in order to estimate the cluster mass. The mass-richness relation can also be calibrated by using weak gravitational lensing to measure the masses of clusters. Simet et al. (2017) used the redMaPPer cluster catalogue and a shape catalogue derived from SDSS photometry to measure the cluster masses as a function of their richness.

The friends-of-friends algorithm is a popular technique for spectroscopic surveys that associates objects within a defined radius called the "linking length", doing so iteratively until no further objects are added. This can be used to find virialized halos in simulations (Frenk et al., 1988) as well as galaxy groups and clusters in spectroscopic surveys (Huchra & Geller 1982, Eke et al. 2004, Berlind et al. 2006). Yang et al. (2007) use a more complex approach, where they locate potential group centres, estimate their characteristic luminosity, then make use of the average mass-to-light ratio for groups to assume a group mass. Then, this information is used to estimate the halo size and velocity distribution. This process is repeated iteratively to build up the group membership in redshift space. Finally, a group mass is then estimated using the luminosities (or the stellar masses) of the group members.

Tinker (2020a) expands on the methodology of Yang et al. (2007). The improved algorithm no longer implicitly assumes that red and blue galaxies share the same galaxy and halo properties. The group finding algorithm additionally self-calibrates by comparing results to external data sets and mock catalogues. These changes are designed to improve the mass estimation of the groups and increase the purity of the satellite selection. The masses of the Tinker groups have not previously been tested with weak gravitational lensing.

In this chapter, we make use of weak gravitational lensing to measure group and cluster masses and compare the consistency of the various mass estimation techniques used by group and cluster finders. To do this, we leverage the Canada-France Imaging Survey (CFIS), a wide area survey with exquisite image quality, as our data set. CFIS is part of the Ultraviolet Near-Infrared Optical Northern Survey (UNIONS). One of the primary scientific drivers of the CFIS survey is weak gravitational lensing, and it will ultimately consist of 4,800 square degrees of r-band data with a median seeing of 0.65 arcseconds and a depth of 24.1 magnitudes for a point source in a 2 arcsecond aperture at 10 σ (25.3 magnitudes at 5 σ). We make use of an internal release of the first 1,565 square degrees of weak lensing galaxy shapes (Guinot et al., submitted) to place constraints on galaxy group and cluster masses using the Tinker group catalogue (Tinker, 2020b) and the redMaPPer cluster catalogue (Rykoff et al., 2014).

In Section 2.2 we outline the basic method for measuring masses using weak gravitational lensing. Section 2.3 describes the CFIS weak lensing data and our procedure for modelling the source redshift distribution. Section 2.4 reviews the redMaPPer cluster catalogue and the Tinker (2020b) group catalogue and the models we use to fit the data. We present the results in 2.5 and

summarize our conclusions in 2.6.

Throughout this chapter, we adopt a flat ΛCDM cosmology with a Hubble parameter $h \equiv H_0/(100 \text{ km s}^{-1} \text{ Mpc}^{-1}) = 0.7$ and $\Omega_\text{m} = 0.3$. The h dependence is included in all derived quantities throughout this work. Halo masses are defined as the mass within a radius where the density is 200 times the mean matter density ($M_{200\text{m}}$).

2.2 Masses from Weak Gravitational Lensing

Weak lensing is the distortion of light from distant background galaxies as they pass through intervening gravitational potentials. For a circularly-symmetric lens, the distortion comes in the form of a small tangential shear, much smaller than the intrinsic ellipticity of a typical galaxy. Therefore, to detect this shear, one must measure the shapes of many galaxies behind these foreground lens objects to determine if there is any statistical preference for the background galaxies to lie tangentially around them.

The advantage of gravitational lensing is that it is sensitive to both the baryonic matter and the dark matter, regardless of its dynamical state, making it a powerful probe of the dark sector. Indeed, weak gravitational lensing has long been used to probe the structure of dark matter at cluster scales (Tyson et al., 1990), at galaxy scales (Brainerd et al., 1996; Hudson et al., 1998) and at the scales of large-scale structure (Wittman et al. 2000, Van Waerbeke et al. 2000, Bacon et al. 2000). Weak lensing studies of galaxy groups are more challenging because large spectroscopic surveys are required to identify large samples of galaxy groups, which must then be stacked. For these reasons, the earliest weak lensing studies of galaxy groups (Hoekstra et al., 2001; Parker et al., 2005) are more recent than the studies of clusters and galaxies.

In weak lensing, the measured galaxy shapes allow us to measure the tangential shear, γ_t. This can be related to the underlying mass of a circularly symmetric object as follows:

$$\gamma_\text{t} = \frac{\Delta\Sigma}{\Sigma_\text{cr}} \tag{2.1}$$

where $\Delta\Sigma$ is the excess surface density (ESD), and Σ_cr is the critical surface density. The excess surface density with respect to the mean surface density is defined as

$$\Delta\Sigma = \overline{\Sigma}(<R) - \Sigma(R) \tag{2.2}$$

where R is the projected separation between the lens and the background source on the sky at the distance of the lens and $\bar{\Sigma}(< R)$ is the mean surface density within R. The critical surface

density can be expressed as

$$\Sigma_{\rm cr}(z_{\rm l}, z_{\rm s}) = \frac{c^2}{4\pi G} \frac{D_{\rm A}(z_{\rm s})}{D_{\rm A}(z_{\rm l})\ D_{\rm A}(z_{\rm l}, z_{\rm s})} \tag{2.3}$$

where $D_{\rm A}(z_{\rm l})$, $D_{\rm A}(z_{\rm s})$, and $D_{\rm A}(z_{\rm l}, z_{\rm s})$ are the angular diameter distances to the lens, source, and between the lens and source, respectively. This, however, assumes that redshifts are available for each source galaxy, which is not the case for the CFIS survey at this time, since all bands of UNIONS have not been observed yet, therefore photometric redshifts are not available. In order to mitigate this lack of information, for CFIS, we compute the inverse effective critical surface density by integrating over the possible source redshifts

$$\widetilde{\Sigma}_{\rm cr}^{-1} = \frac{4\pi G}{c^2} \int_{z_{\rm l}}^{\infty} \frac{D_{\rm A}(z_{\rm l})\ D_{\rm A}(z_{\rm l}, z_{\rm s})}{D_{\rm A}(z_{\rm s})}\ n(z_{\rm s})\ dz_{\rm s} \tag{2.4}$$

where $n(z_{\rm s})$ represents the normalized probability density function of the source redshifts in the CFIS survey. The determination of $n(z_{\rm s})$ will be discussed in additional detail in Section 2.3.1.

Following Sheldon et al. (2004), each lens source pair is then given a weight, $w_{\rm ls}$, defined as:

$$w_{\rm ls} = w_{\rm s}\ \widetilde{\Sigma}_{\rm cr}^{-2} \tag{2.5}$$

where $w_{\rm s}$ is the statistical weight assigned to the source ellipticity. For high redshift lenses, the $\widetilde{\Sigma}_{\rm cr}$ term effectively down-weights the lens-source pairs, as sources that are near the lens are less sensitive to the shear.

2.3 Source galaxy catalogue from CFIS

The Ultraviolet Near Infrared Optical Northern Survey (UNIONS) collaboration is a collaboration of wide field imaging surveys of the northern hemisphere. UNIONS consists of the Canada-France Imaging Survey (CFIS), conducted at the 3.6-meter CFHT on Maunakea, members of the Pan-STARRS team, and the Wide Imaging with Subaru HyperSuprime-Cam of the Euclid Sky (WISHES) team. CFHT/CFIS is obtaining deep u and r bands; Pan-STARRS is obtaining deep i and moderate-deep z band imaging, and Subaru/WISHES is obtaining deep z band imaging. These independent efforts are directed, in part, to securing optical imaging to complement the Euclid space mission, although UNIONS is a separate collaboration aimed at maximizing the science return of these large and deep surveys of the northern skies.

A primary science driver of the survey is weak gravitational lensing. The survey will ultimately contain 4,800 square degrees of high quality, r-band weak lensing data. This work uses an internal "version 0" release of the first 1,565 square degrees of weak lensing data.

For this work, we use the shape catalogue generated by the ShapePipe shape measurement pipeline (Guinot et al., submitted). ShapePipe uses the `ngmix` [1] software package for shape measurements, which fits a Gaussian mixture model to the galaxy images to determine their shape, and metacalibration (Sheldon & Huff, 2017) for a preliminary calibration of the shape measurements. Overall, 40,151,119 calibrated galaxy shapes are produced for this preliminary CFIS shape catalogue yielding an average density of 7.13 galaxies per square arcminute in unmasked areas. It should be noted that, for this version 0 release, the selection criteria are conservative; future releases are expected to achieve a higher surface density of sources.

For weak lensing, compared to SDSS, it should be noted that the number density of source galaxies is not the only advantage of the CFIS data. The CFIS data are also deeper, which when paired with improved image quality, provides a greater fraction of sources at large distances. This increases $\widetilde{\Sigma}_{\rm cr}^{-1}$, boosting the excess surface mass density signal (Equations 2.4 and 2.9).

2.3.1 Source galaxy redshift distribution

As demonstrated by equation 2.4, an estimate of the redshift distribution of background sources is required in order to compute the effective critical surface density. Accurately determining this redshift distribution is critical to obtaining an unbiased estimate of cluster and group masses (Hoekstra et al., 2015). This presents a complication for CFIS as the survey is deeper than overlapping spectroscopic surveys, and photometry is available for the sources in the r band only.

To estimate the source redshift distribution, we therefore leverage the overlapping CFHTLenS survey, which is both slightly deeper than CFIS and has deep photometry in 5 bands. We match the objects in the 50 square degree W3 region, covered by both CFIS and CFHTLenS, so that we have multiband CFHTLenS photometry for the CFIS objects.

We then apply the methodology described in Lima et al. (2008) in order to estimate the $n(z_{\rm s})$ from the multi-band photometry. Essentially, this method compares the photometric distribution of the sources with those from another sample that also contains spectroscopic redshifts for each source. In our case, the spectroscopic sample comes from SDSS (Blanton et al., 2017), DEEP2/3 (Newman et al., 2013), and VVDS (Le Fèvre et al., 2013) fields that overlap CFHTLenS photometry. For the matched CFIS-CFHTLenS catalogue, we estimate the density of CFIS sources in the 5-dimensional CFHTLenS magnitude space, and do likewise with the galaxies in the spectroscopic sample. The sample of spectroscopic redshifts is then reweighted until its density in the 5-dimensional magnitude space matches that of the CFIS catalogue. Note that with this method there is no explicit source-by-source matching between CFIS sources and the

[1] https://github.com/esheldon/ngmix

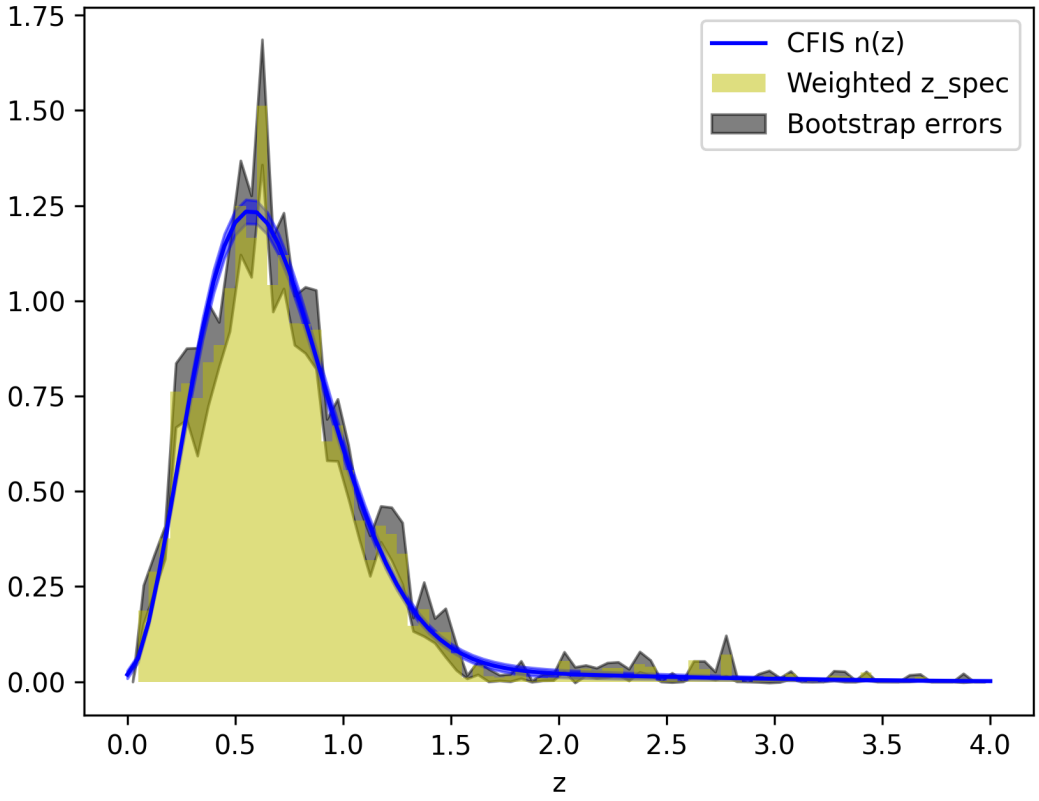

Figure 2.1: The reweighted spectroscopic redshift distribution (yellow) with uncertainties from bootstrapping (black). The n(z) fit to this distribution and used throughout this work is overplotted along with its one sigma uncertainties (blue).

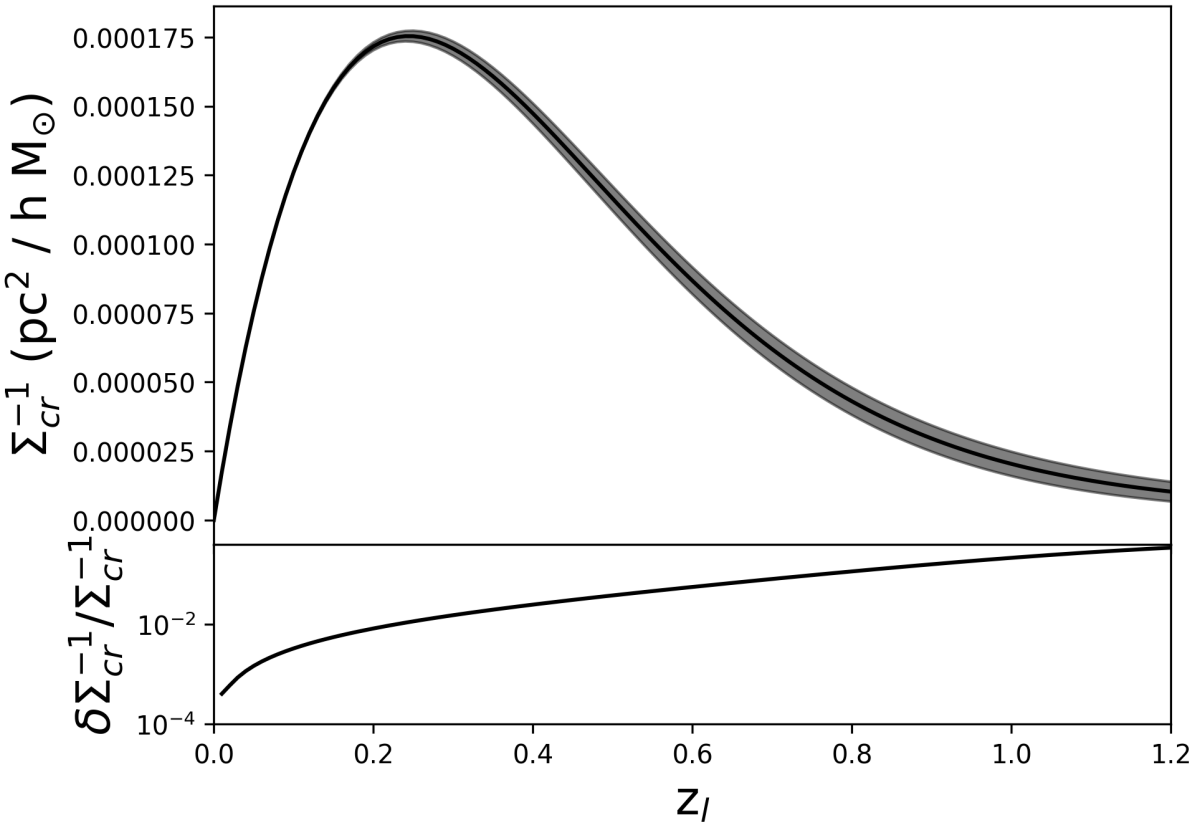

Figure 2.2: Inverse critical surface mass density, $\langle\Sigma_{\rm cr}^{-1}\rangle$, as a function of the lens redshift. In the lower panel, we plot the fractional error in this quantity.

spectroscopic sample, and hence no need for the spectroscopic sample to overlap on the sky with the CFIS sample (although it does partially because DEEP2/3 is observed in CFIS). The reweighted spectroscopic redshift distribution can then be used as an estimate of the $n(z_s)$ for the CFIS survey. This technique avoids the systematic biases associated with using photometric redshifts, and has shown to be effective in similar weak lensing surveys such as KiDS (Hildebrandt et al., 2017).

To estimate the effect of cosmic variance, we first divide the spectroscopic catalogue into 10 equally sized regions, bootstrap resample those regions, then reweight the bootstrapped catalogues to obtain an uncertainty for the $n(z_s)$. We then fit the profile with a 2-term model, following Hildebrandt et al. (2017):

$$n(z) = \left(A \cdot \frac{z^{\alpha} \cdot e^{-\left(\frac{z}{z_0}\right)^{\alpha}}}{\frac{z_0^{\alpha+1}}{\alpha} \cdot \Gamma(\frac{\alpha+1}{\alpha})} \right) + \left((1-A) \cdot \frac{e^{-\frac{(z-\mu)^2}{2\sigma^2}}}{2.5046} \right). \tag{2.6}$$

The first term fits the initial peak, while the second term defines the extended high-redshift tail of the distribution. As in Hildebrandt et al. (2017), we fix $\sigma = 1.3$ and $\mu = 1$ for the tail as these parameters are not well constrained by the fitting process, and $\alpha = 1.79$ for the first term. This combination of values allows for an extended wing to fit the high redshift tail, but that doesn't contribute to an excess at the low redshift end of the distribution. z_0 and A are fit, which together determine the location of the peak and how much weight is given to the peak versus the tail. Γ is the gamma function, and the constant in the denominator of the second term is the normalization factor.

For the ShapePipe catalogue, the best fit parameters from using an affine invariant Markov chain Monte Carlo sampler are $z_0 = 0.571$ and $A = 0.936$, resulting in a mean redshift of 0.73.

To estimate the uncertainty in the source redshift distribution, we fit each of the 1,000 bootstrapped samples with the same model. We then calculate the variance in the resulting inverse critical surface mass density. For lenses with $z_l \lesssim 0.23$, this results in a relative error of $\leq 1\%$ in the inverse critical surface mass density (Figure 2.2). The highest redshift bins used in this work are ≈ 0.27 which corresponds to a relative error of $\approx 1.3\%$. We therefore find that the uncertainty in the source redshift distribution is subdominant compared to our other uncertainties and ignore it hereafter.

2.4 Lenses

2.4.1 redMaPPer Clusters

As these are among the first weak lensing results from the CFIS survey, we opt to validate the survey by making a direct comparison to previously published works. Simet et al. (2017) estimated the mass-richness relation for clusters by measuring weak lensing masses of redMaPPer clusters (Rykoff et al., 2014) using source shapes from SDSS imaging data. Because the same cluster catalogue is being analyzed using the same methodology, we expect to derive a mass-richness relation in agreement with Simet et al. (2017). The clusters are binned by the richness parameter, λ, and by redshift in order to make a measurement of the mass-richness relation. Richness, as defined by the redMaPPer cluster finder, is simply the sum of the probabilities that each satellite is a member of the cluster. A comparison with the results of Simet et al. (2017) is made in Section 2.5.

$\Delta\Sigma$ model for redMaPPer clusters

In reality, the redMaPPer galaxy clusters (Figure 2.3) may not have correct centres. Here we follow Simet et al. (2017) and assume that a fraction $p = 0.8$ of the clusters are well-centred and $(1 - p) = 0.2$ are miscentred. To create the miscentred $\Delta\Sigma$ profiles, we first calculate the following contribution from an offset or miscentred halo

$$\Sigma_{\rm mis}(R|R_{\rm mis}) = \frac{1}{2\pi}\int_0^{2\pi} \Sigma_{\rm NFW}\left(\sqrt{R^2 + R_{\rm mis}^2 + 2RR_{\rm mis}\cos\theta}\right) d\theta \tag{2.7}$$

where $R_{\rm mis}$ is the distance between the true cluster centre and the measured cluster centre. We then use equation 2.2 to calculate $\Delta\Sigma$. Finally, we convolve this with a distribution of offsets $R_{\rm mis}$, assumed to be a Gaussian with $\sigma(R_{\rm mis}) = 0.4\ h^{-1}$ Mpc and a mean of $0.0\ h^{-1}$ Mpc, in accordance with Simet et al. (2017). The NFW mass assumed for the miscentred component is assumed to be the same as for the centred component. We adopt the mass-concentration relation of Duffy et al. (2008) when defining our haloes, and reported masses are masses within a sphere where the matter density exceeds 200 times the mean matter density of the universe ($M_{\rm 200m}$). Having fixed the centring probabilities, p and the concentration c, there is only a single free parameter, $M_{\rm 200m}$.

We omit the innermost regions ($R < 0.3\ h^{-1}$ Mpc) to reduce systematic issues from strong lensing near the cluster centres, lack of stellar mass estimates, and dilution which is strongest in these regions. Finally, we apply a small multiplicative correction of 0.98 to the final mass to account for cluster projection and triaxiality as estimated by Simet et al. (2017).

Properties of the redMaPPer lens sample are available in Table 2.1.

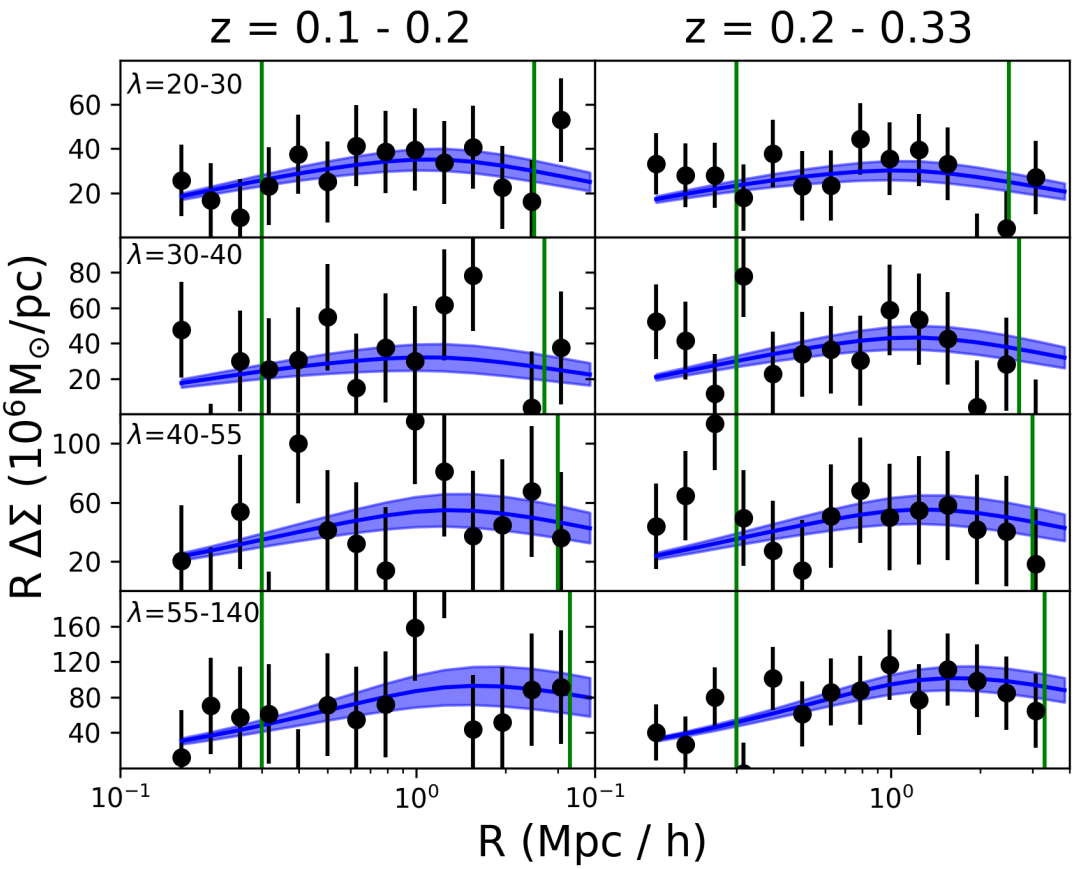

Figure 2.3: Weak lensing signals for all 4 richness bins fit with the halo model. As no stellar masses are available for the redMaPPer sample, we simply restrict our fit to larger radii and omit the stellar contribution. The shaded region represents the 1σ uncertainty. The vertical green lines indicate the inner and outer limits of the fit.

Table 2.1: Properties of the lens sample selected from the redMaPPer cluster catalogue. Clusters were binned by their richness, λ, and redshift.

Richness Bin	Redshift Bin	$\langle z \rangle$	$N_{\rm lenses}$	$\langle \lambda \rangle$	$\log\langle \frac{M_{\rm h,wl}}{h^{-1}M_\odot} \rangle$
[20, 30)	[0.1, 0.2)	0.162	158	24.1	$14.26^{+0.09}_{-0.10}$
[20, 30)	[0.2, 0.33)	0.272	390	24.2	$14.11^{+0.08}_{-0.10}$
[30, 40)	[0.1, 0.2)	0.162	59	34.3	$14.17^{+0.15}_{-0.19}$
[30, 40)	[0.2, 0.33)	0.271	163	34.3	$14.33^{+0.10}_{-0.11}$
[40, 55)	[0.1, 0.2)	0.165	28	46.5	$14.49^{+0.13}_{-0.16}$
[40, 55)	[0.2, 0.33)	0.272	84	46.4	$14.47^{+0.11}_{-0.13}$
[55, 140)	[0.1, 0.2)	0.163	12	69.5	$14.82^{+0.16}_{-0.21}$
[55, 140)	[0.2, 0.33)	0.273	54	72.5	$14.88^{+0.09}_{-0.10}$

Dilution

There are no photometric redshifts for our dataset at this time. Consequently, it is difficult to separate cluster members from background sources. The cluster members are not sheared and so dilute the weak lensing signal. To estimate this effect, we adopt the method of Sheldon et al. (2004). We select random RA and Dec positions from within the CFIS footprint and assign them redshifts from our lens catalogue, ensuring that the redshift distribution of the lens catalogue and the random catalogue are similar. We then process this set of random points as if they are lenses. Here, $C(R)$ corresponds to the overdensity of sources around the lenses by comparing the density to a set of randomly selected points in the survey which represent the mean source density.

$$C(R) = \frac{N_r}{N_l} \frac{f_r(R)}{f_l(R)} \frac{\Sigma_{ls} w_{ls}}{\Sigma_{rs} w_{rs}} \tag{2.8}$$

The number of randomly selected "lenses" is N_r , N_l is the number of group/cluster lenses, $f_r(R)$ and $f_l(R)$ are the fractions of pixels which are unmasked around the random points and the lenses respectively, and w_{rs} and w_{ls} are the weights of the background galaxies around the randoms points and the group/cluster lenses respectively.

Because masking can vary from one point to another in the survey, we must also account for

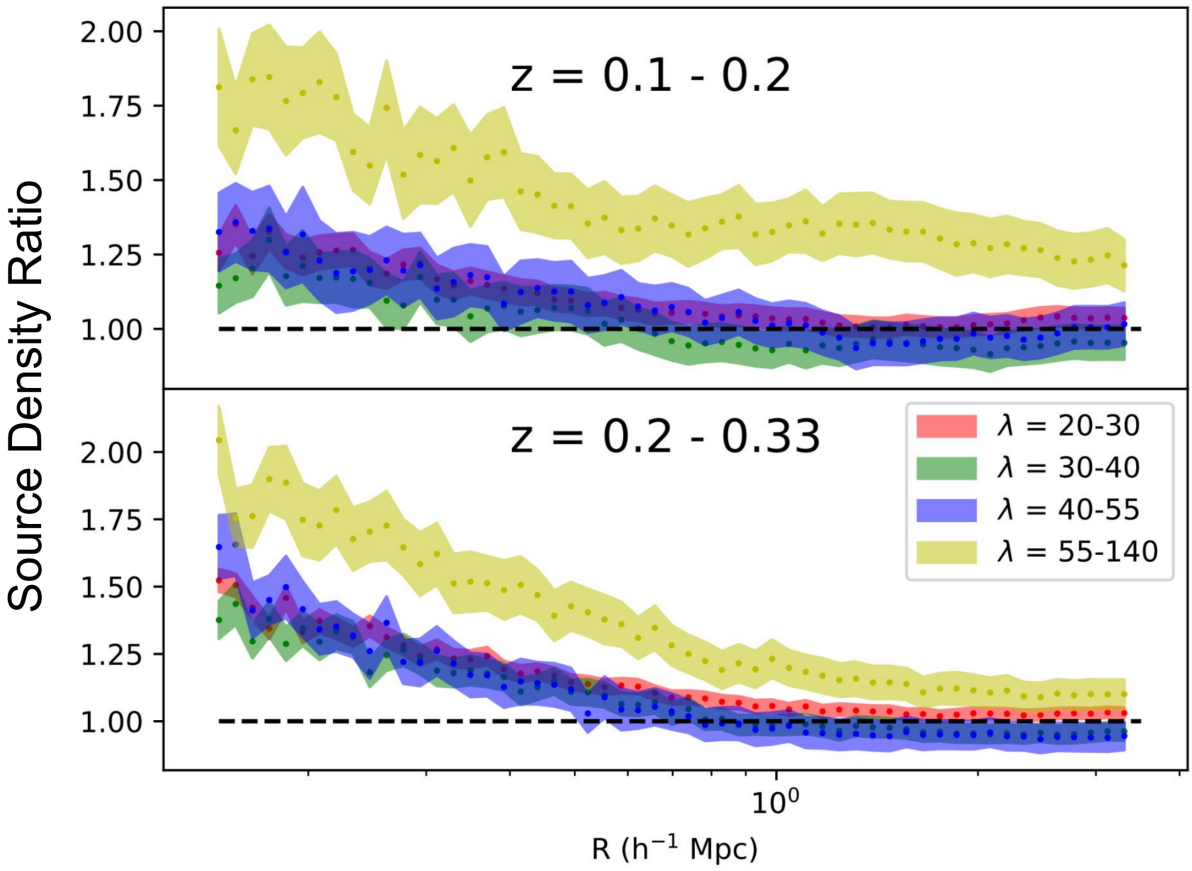

Figure 2.4: Source density ratio for the redMaPPer richness bins.

the masked out fraction around each random point and cluster as the variable masking affects our measurement of the source density. We therefore Monte-Carlo sample the masks around every random point and cluster, calculate the masked out fraction for each of these points, then correct the overall source density.

Uncertainties in the overdensity are estimated by examining the number density of sources around a selection of random points. This variability in the source density from one CFIS field to the next enhances the uncertainty in the dilution correction factors, and hence the $\Delta\Sigma$ signal as well as the final fitted masses. Given that the boost factors are correlated from one bin to the next, we use covariance matrices to propagate these correlations into the final uncertainties.

Following Simet et al. (2017), we randomly select 20 sets of coordinates from the region where CFIS and SDSS overlap for each lens in our catalogue to compute the overdensity. Source density ratios for both redshift bins are plotted in Figure 2.4. It can be seen from Figure 2.4 that this effect is something that must be accounted for, particularly for very rich clusters where there remains an overdensity of sources even at large separations from the cluster centres.

We could use 2.8 to compensate for the effect of dilution, but instead, we opt to utilize the Singh et al. (2017) estimator which attempts to correct for this effect by considering the density of sources around the lenses as well as around a set of randomly selected points. Additionally, this estimator subtracts the tangential shear around the random points. The estimator implicitly assumes that the area around the clusters and the random points is equally masked in the survey. We therefore incorporate the sampling of the masks around the lenses and randoms, and apply them as a modification as follows:

$$\Delta\Sigma(R) = \frac{N_r}{N_l}\frac{f_r(R)}{f_l(R)}\frac{\sum_{ls} w_{ls}\gamma_{\mathrm{t},ls}(R)\Sigma_{\mathrm{cr},ls}}{\sum_{rs} w_{rs}} - \frac{\sum_{rs} w_{rs}\gamma_{\mathrm{t},rs}(R)\Sigma_{\mathrm{cr},rs}}{\sum_{rs} w_{rs}}. \tag{2.9}$$

2.4.2 Tinker Groups

Lenses have also been selected from the group catalogue compiled by Tinker (2020b). This group catalogue was created using a new self-calibrating group finding algorithm, which was applied to the SDSS catalogue.

We bin the Tinker groups by their abundance-matched halo mass into 4 equally sized bins. Properties of the lens sample binned by the halo mass are found in Table 2.2.

We also split the group sample by colour, using the COLOR_FLAG parameter included in the Tinker catalogue which is derived from measurements of the 4000 Å ngstrom break of the central

Table 2.2: Properties of the lens sample selected from the Tinker group catalogue. The lenses were binned by the halo mass as estimated in the Tinker catalogue. N_{lenses} is the number of lenses in the given M_h bin. Also shown are the log of the mean estimated halo mass, the log of the mean halo mass after adjusting the value of S_8, the mean redshift, the log of the mean stellar mass of the group centrals, the log of the mean mass as measured by weak gravitational lensing in this work, and the reduced χ^2 of fit to determine the mass.

M_h Bin	N_{lenses}	$\log\langle\frac{M_h}{h^{-1}M_\odot}\rangle$	$\log\langle\frac{M_{h,S_8}}{h^{-1}M_\odot}\rangle$	$\langle z\rangle$	$\log\langle\frac{M_*}{M_\odot}\rangle$	$\log\langle\frac{M_{h,wl}}{h^{-1}M_\odot}\rangle$	χ^2_{red}
(12.5, 13.0]	14785	12.75	12.72	0.13	11.17	$12.69^{+0.16}_{-0.13}$	1.01
(13.0, 13.5]	8227	13.24	13.20	0.15	11.36	$13.36^{+0.07}_{-0.07}$	0.94
(13.5, 14.0]	3833	13.74	13.68	0.17	11.53	$13.80^{+0.06}_{-0.05}$	0.89
(14.0, ∞]	1633	14.36	14.28	0.21	11.71	$14.18^{+0.06}_{-0.05}$	0.84

galaxy in the group. More specifically, Tinker (2020b) defines the boundary between star forming blue galaxies and quiescent red galaxies as:

$$D_{crit} = 1.42 + \frac{0.35}{2}\left[1 + \mathrm{erf}\left(\frac{\log L_{gal} - 9.9}{0.8}\right)\right] \tag{2.10}$$

The red and blue samples are then binned by stellar mass. The properties of the groups from this binning regime are listed in Table 2.3.

$\Delta\Sigma$ model for Tinker groups

For the galaxy groups, we compare the density of sources to those around a set of random points. We see no evidence of a significant overdensity of galaxies around these galaxy groups. This is likely due to the small overdensity in a narrow redshift range from galaxies in the group being dominated by the high background density due to the depth of the survey. We therefore neglect the effect of dilution, and opt to use a simpler estimator that makes no correction for this effect.

$$\Delta\Sigma(r) = \frac{\Sigma_{ls} w_{ls} \gamma_t \tilde{\Sigma}_{cr,ls}}{\Sigma_{ls} w_{ls}} \tag{2.11}$$

Uncertainties in the $\Delta\Sigma$ signals of the Tinker groups are calculated in a more simple way than with the redMaPPer clusters since dilution is not a concern due to the lower richness nature of the

Table 2.3: Properties of the lens sample selected from the Tinker group catalogue. The lenses were binned by the colour and stellar mass as estimated in the Tinker catalogue.

M_* Bin	$N_{\rm lenses}$	$\log\langle\frac{M_{\rm h,Tinker}}{h^{-1}M_\odot}\rangle$	$\langle z\rangle$	$\log\langle\frac{M_*}{M_\odot}\rangle$	$\langle M_{\rm h,wl}\rangle/10^{12}$ $(h^{-1}M_\odot)$	$\chi^2_{\rm red}$
			Blue			
(10.0, 10.4]	7859	11.83	0.07	10.23	$0.07^{+1.44}_{-0.07}$	1.72
(10.4, 10.8]	10717	12.11	0.09	10.62	$0.17^{+1.30}_{-0.17}$	1.36
(10.8, 11.2]	10507	12.41	0.12	11.00	$2.38^{+2.01}_{-1.68}$	1.06
(11.2, 11.6]	3860	12.80	0.16	11.36	$3.22^{+4.13}_{-3.00}$	0.85
(11.6, ∞]	395	13.46	0.20	11.75	$7.69^{+18.8}_{-7.69}$	0.69
			Red			
(10.0, 10.4]	1781	12.05	0.05	10.26	$12.3^{+11.6}_{-7.97}$	0.97
(10.4, 10.8]	6579	12.28	0.07	10.65	$2.32^{+2.96}_{-2.07}$	1.34
(10.8, 11.2]	14333	12.80	0.11	11.03	$8.80^{+2.53}_{-2.43}$	0.89
(11.2, 11.6]	12506	13.42	0.15	11.39	$21.5^{+3.48}_{-3.82}$	1.04
(11.6, ∞]	2779	14.09	0.20	11.74	$75.6^{+13.6}_{-13.2}$	0.89

lenses. For the uncertainty, we use the variance of the ShapePipe shape catalogue. In general, this can be written as

$$\mathrm{Var}(\gamma_t) = \left(\frac{1}{\Sigma w_i}\right)^2 \Sigma w_i^2 \sigma_i^2 \tag{2.12}$$

where w_i is the weight assigned to a given galaxy shape measurement and σ_i is the variance of the ellipticity. For ShapePipe , σ_i^2 is simply $\frac{1}{2w_i}$. The variance therefore reduces to

$$\mathrm{Var}(\gamma_t) = \frac{1}{2\Sigma w_i} \tag{2.13}$$

This quantity is calculated for each radial bin, and multiplied by $\Sigma_{\rm cr}$ to obtain the final uncertainty for each $\Delta\Sigma$ measurement.

The $\Delta\Sigma$ signals are fit with simple NFW profiles for the group component. Given that the Tinker (2020b) catalogue is accompanied with a mock catalogue, we additionally fit the signals for these groups with an offset component to account for miscentring and other inaccuracies in the group finding algorithm. We bin the mock catalogue with the same constraints as the real group catalogue, and generate offset NFW halos for each group using the following equation to calculate their contribution.

$$\bar{\Sigma}_{\rm OH}(R|R_{\rm OH}) = \frac{1}{2\pi}\int_0^{2\pi} \mathrm{d}\theta\, \Sigma_{\rm NFW}\left(\sqrt{R_{\rm OH}^2 + R^2 + 2RR_{\rm OH}\cos\theta}\right) \tag{2.14}$$

We compute the mean of these individual profiles and take this as the total offset halo contribution to the $\Delta\Sigma$ signal. This composite offset profile is then fixed and added to the overall model.

Finally, we add a stellar component with fixed mass M_* to complete the model using the following equation:

$$\Delta\Sigma_* = \frac{M_*}{\pi R^2} \tag{2.15}$$

The data were fit out to $2R_{200}$ to avoid fitting contributions to the $\Delta\Sigma$ signal from contaminating effects from nearby structures.

2.5 Results and Discussion

2.5.1 Clusters

In order to test the validity of our source redshift distribution $n(z_{\rm s})$ model, as well as the shape measurement pipelines used by the CFIS survey, we make a comparison of redMaPPer clusters

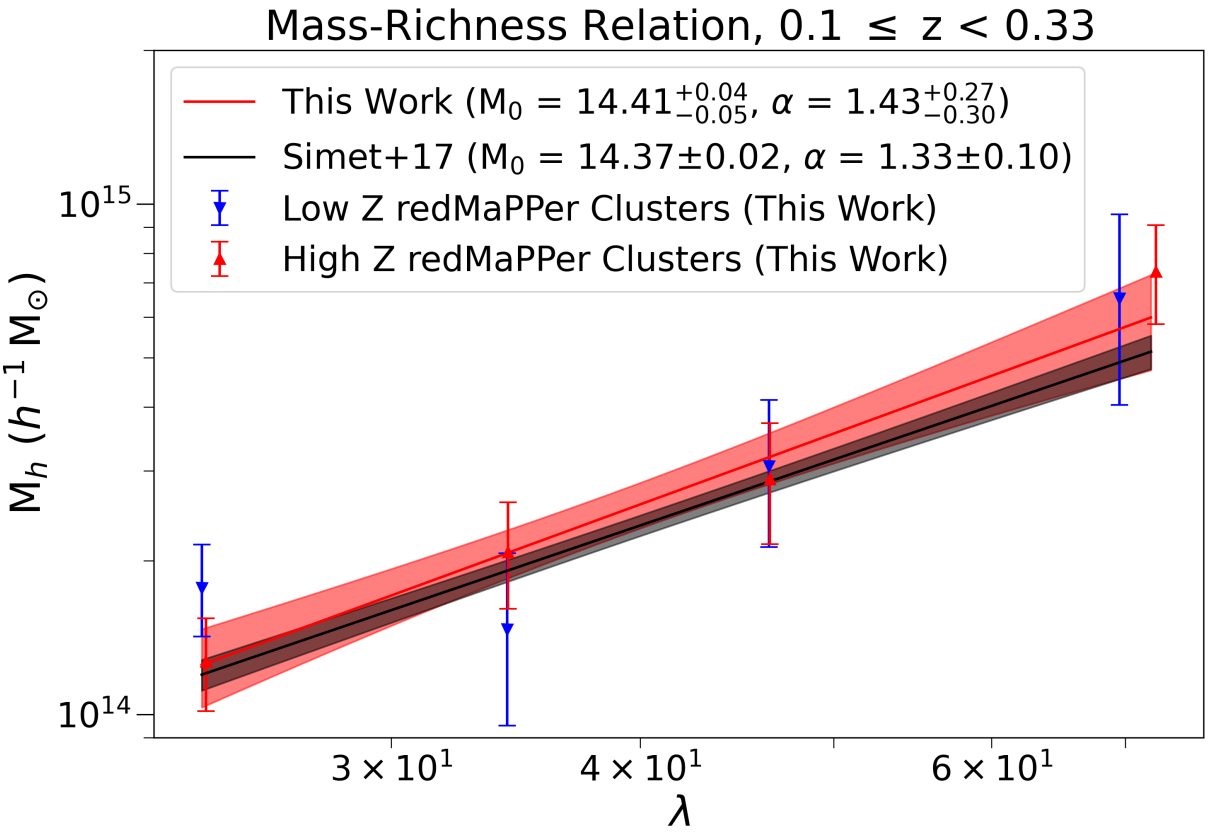

Figure 2.5: The mass-richness relation for redMaPPer clusters compared to the mass-richness relation from Simet et al. (2017).

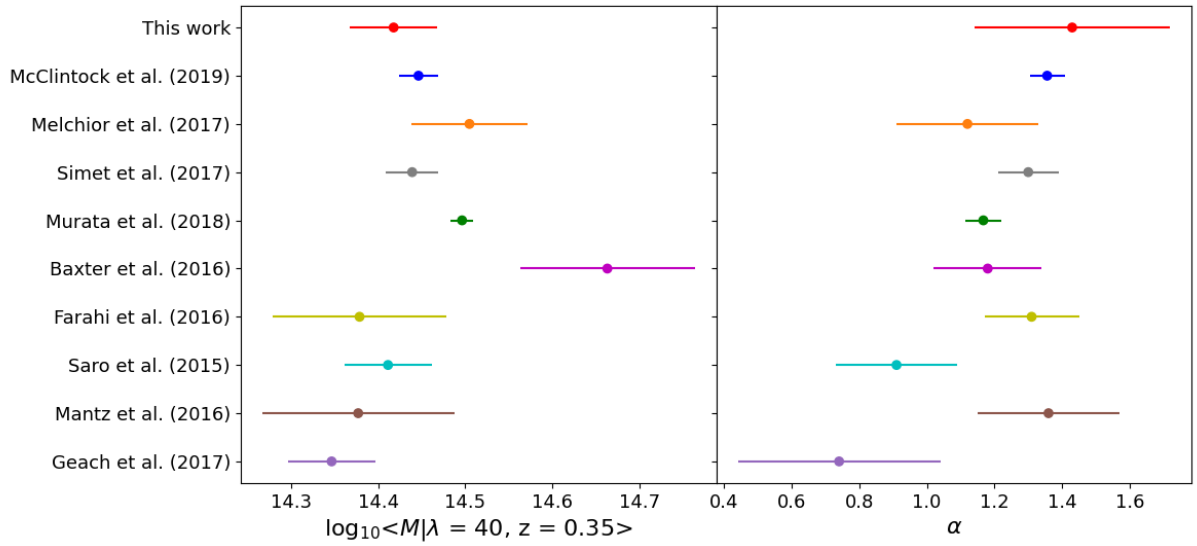

Figure 2.6: A comparison between the mass-richness relations from this work and from literature. λ values have all been converted to $\lambda_{\rm SDSS}$ to account for differing survey depths, and the relation derived in this work has been redshift evolved to $z = 0.35$ to make a direct comparison with the others.

and the resulting mass-richness relation to that of Simet et al. (2017). After binning the clusters by redshift and λ, measuring their $\Delta\Sigma$ profiles, and fitting them with the methodology described in Section 2.4.1, we apply a 2% correction to the mass to account for the effects of projection and triaxiality based on the analysis of Simet et al. (2017). The resulting masses are listed in Table 2.1. Finally, we fit a mass-richness relation to the redMaPPer cluster weak lensing masses, using the following form defined in Simet et al. (2017),

$$\langle M|\lambda\rangle = M_0 \left(\frac{\lambda}{\lambda_0}\right)^{\alpha}, \tag{2.16}$$

with the pivot, λ_0, fixed to 40. As can be seen in Figure 2.5, our measured values of M_0 and λ are in good agreement with those of Simet et al. (2017).

In addition to the mass-richness relation comparison with Simet et al. (2017), we also compare our results to a collection of redMaPPer mass-richness relations from literature. We use the collection of relations compiled in McClintock et al. (2019) as the basis for our comparisons. These mass-richness relations come from a variety of surveys with varying depths, which induces a disagreement in the λ measurement of a given cluster. As McClintock et al. (2019) cites the

$\lambda_{\rm DES\ Y1}$ values, we first convert them to the $\lambda_{\rm SDSS}$ values used elsewhere in this work. We also include redshift evolution to make a fair comparison to the other relations. To this end, we use the following conversions from McClintock et al. (2019).

$$\lambda_{\rm SDSS} = (0.93 \pm 0.14)\lambda_{\rm DES\ Y1} \tag{2.17}$$

$$M(\lambda, z) = M_0 \left(\frac{\lambda_{\rm SDSS}}{\lambda_0}\right)^{\alpha} \left(\frac{1+z}{1+z_0}\right)^{G_z} \tag{2.18}$$

We use $z_0 = 0.35$ and $G_z = -0.3 \pm 0.3$ to evolve our mass-richness relation to the same redshift as our comparison values. The comparison is presented in Figure 2.6. Our M_0 and α values are in broad agreement with those from other surveys and methodologies. This validates our derivation of the $n(z_{\rm s})$ distribution in Section 2.3.1 despite the lack of photometric and spectroscopic redshifts in the CFIS survey.

2.5.2 Tinker Groups

Halo Mass Binning

We then proceed to the group catalogue of Tinker (2020b). First, we bin the group catalogue by estimated halo mass, then fit the resulting $\Delta\Sigma$ signals using the methodology described in Section 3.4.2. The resulting masses are displayed in Table 2.2 and Figure 2.9. The highest mass bin is not in good agreement with the expected halo mass from the catalogue, given the 3σ discrepancy between the two values. However, it should be noted that unlike Section 2.5, we are not comparing two measurements using similar methodologies and techniques. The mass estimates from the group catalogue come from abundance matching, and therefore we do not necessarily expect strict agreement.

Whereas our fitted masses of redMaPPer clusters were compared to similarly-derived weak lensing masses (Simet et al., 2017), the masses in the Tinker (2020b) catalogue are based on abundance matching with cosmological parameters from the Planck-Bolshoi simulation. These cosmological parameters correspond to a high value of the parameter $S_8 \equiv (\Omega_{\rm m}/0.3)^{0.5}\sigma_8 = 0.83$. This value of S_8 differs from many low-redshift measurements. For example, Boruah et al. (2020) fits a number of non-CMB determinations (weak lensing, peculiar velocities, cluster abundances) of S_8, which together prefer a lower value of $S_8 = 0.765 \pm 0.009$. Note that not all datasets in Boruah et al. (2020) are independent, so the uncertainty in this average should be taken with caution. We therefore test the effect of re-adjusting Tinker's mass estimates. Specifically, we

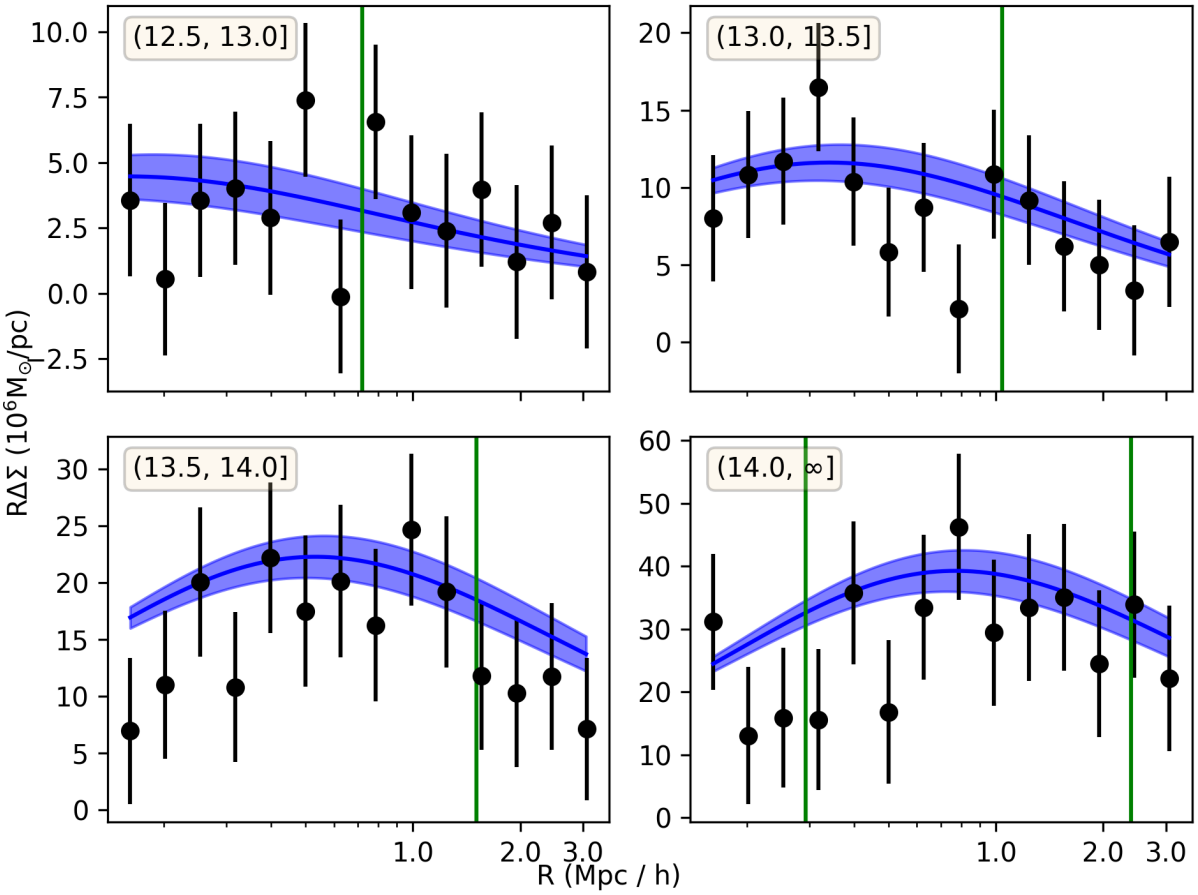

Figure 2.7: Weak lensing signals for all 4 Tinker Group mass bins fit with a halo model consisting of a centred NFW profile, an offset NFW profile, and a stellar component. The vertical green bars indicate the regions being fit. For the three lowest mass bins, there is only an upper limit to the fit range as their Einstein radii were too small to provide a lower limit.

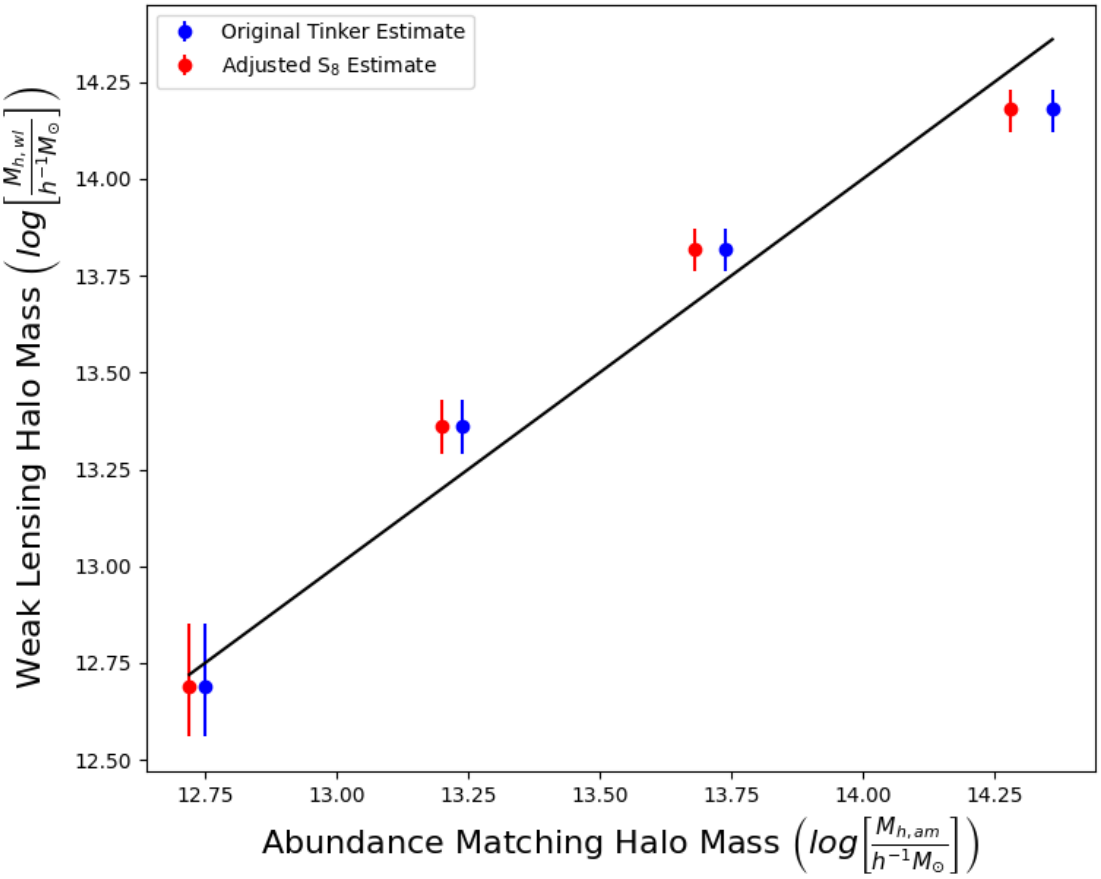

Figure 2.8: Comparison between estimated group halo mass of Tinker (2020b) and the weak lensing masses measured in this work. We show both the original halo mass estimates (blue), as well as the halo mass estimates after reducing S_8 and adjusting the masses via abundance matching (red).

use abundance matching to recalculate the halo masses for cosmologies with lower values of σ_8 by keeping Ω_m fixed at the value of 0.3 and using the Tinker et al. (2008) halo mass function. Reducing S_8 has the effect of reducing all predicted halo masses but the reduction is largest at the highest halo masses. As shown in Fig. 2.8, these $S_8 = 0.76$ halo masses are a better match to the weak lensing masses, particularly because the highest halo mass bin, which is 3.6 sigma discrepant with Bolshoi-Planck $S_8 = 0.83$ reduces to below 2σ for $S_8 = 0.76$. If we fit S_8 by adjusting the abundance-matched masses to the measured weak lensing halo masses, we find $S_8 = 0.74 \pm 0.03$, but the quality of the fit is not good: $\chi^2 = 10.7$ for 3 degrees of freedom ($p = 0.013$). Therefore, the uncertainties on the fitted S_8 may be underestimated.

For the groups with a mean estimated halo mass in excess of $10^{14}\ M_\odot$, we explore some potential explanations for why we observe such a strong discrepancy between the estimated halo mass and the weak lensing halo mass. First, we considered that despite their classifications as groups and not clusters, they have similar estimated masses as the lowest richness redMaPPer clusters. We therefore investigated the possibility that dilution was playing a similar role as in our cluster measurements. However, when measuring the dilution correction factor using Equation 2.8, we find no evidence of dilution around the groups.

We also consider that because of their high estimated mass, there are potentially strong lensing effects at low radial separations from the groups centres that suppress the signal in those regions. We therefore calculate the Einstein radius of the estimated halo mass, and exclude any points within double that radius from the fitting process. For the highest mass groups, this cuts out all data points less than ~0.3 h^{-1} Mpc from the group centre. The masses cited in Table 2.2 already include this cut, and so this also does not explain the discrepancy. The three lowest mass bins do not have Einstein radii large enough to affect the fitting procedure.

Binning by Colour and Stellar Mass of Central Galaxies

Additionally, we separate the groups by the colour of their central galaxy using the $color\_flag$ parameter of the catalogue. We then bin these groups by their estimated stellar mass and measure their weak lensing masses, which can be found in Table 2.3 and Figure 2.10. For the blue groups, we do not have sufficient signal to constrain the masses tightly. We also note that the weak lensing masses for these groups are systematically lower than the expectation from the catalogue, even after correcting for the high mass estimates due to the choice of cosmologies. We therefore fit a multiplicative factor f to the expectation values and find $f = 0.91^{+0.40}_{-0.30}$, indicating that this bias is not statistically significant.

The red groups are tightly constrained at stellar masses greater than $10^{11}\ M_\odot$, and are in better agreement with the expected masses from the catalogue than the blue groups. Additionally, we

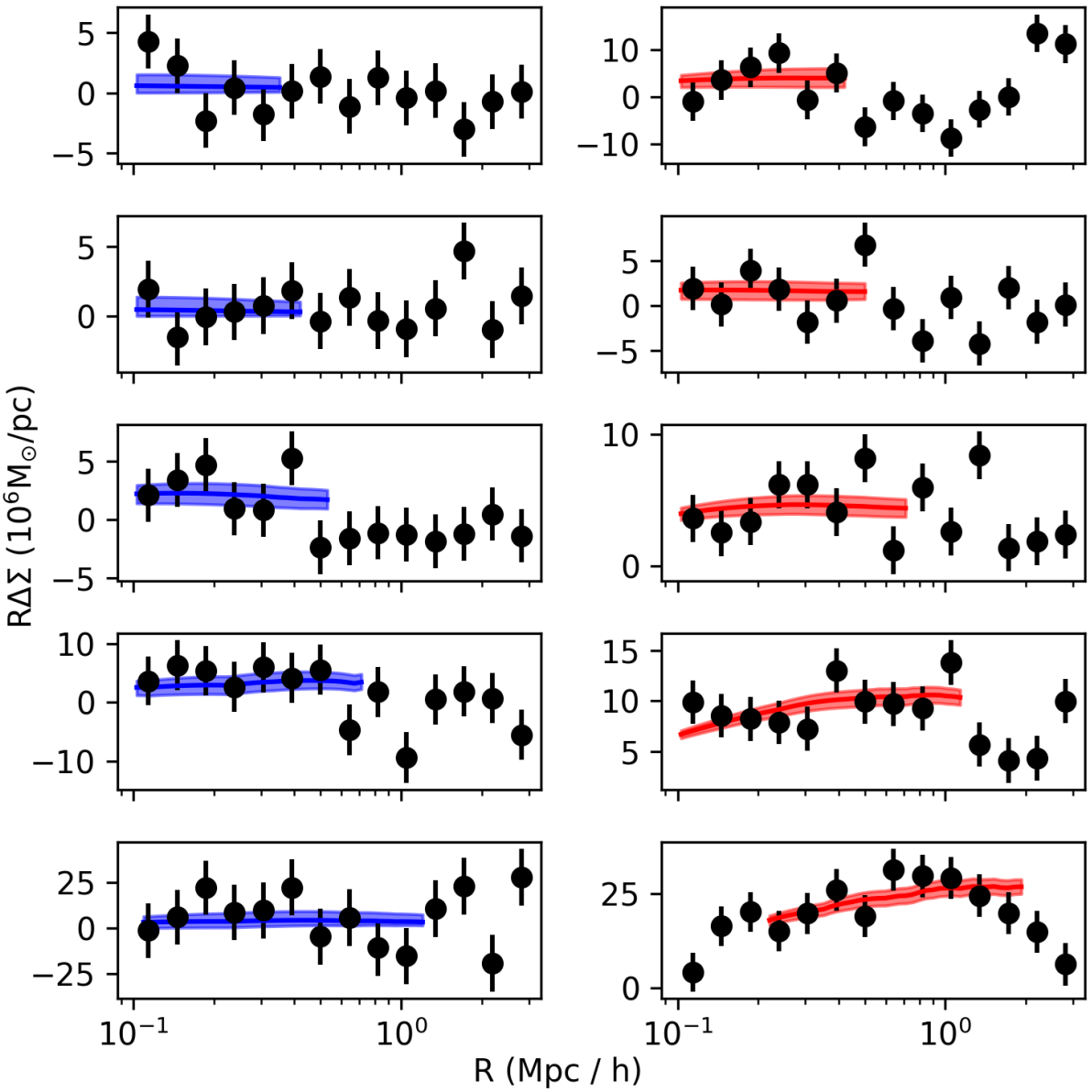

Figure 2.9: Weak lensing signals and fits for all Tinker groups binned by colour and stellar mass. Blue groups are in the left column, and red groups are in the right column. Stellar mass increases with each row. The best fit models and uncertainty are overplotted, and only the region they were fit to is shown. The inner limit to the fit is defined by the Einstein radius or the group, and the outer limit is defined by the virial radius.

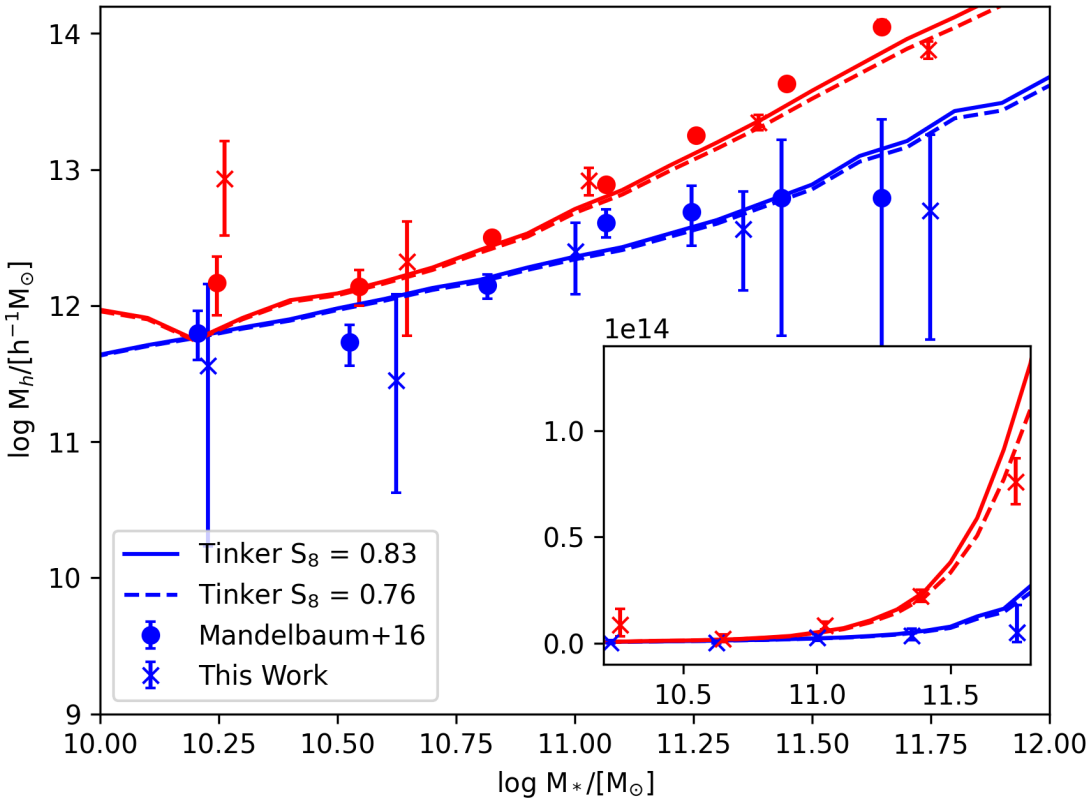

Figure 2.10: Masses for the Tinker groups binned by the colour and stellar mass of their central galaxies, compared to the expectation from the Tinker (2020b) catalogue, which had $S_8 = 0.83$. The dashed lines indicate the expected Tinker masses after adjusting the cosmology to $S_8 = 0.76$. We also show data from Mandelbaum et al. (2016), although these centrals are not drawn from the Tinker groups. Inset: Same plot but with a linearly scaled y-axis to show that the lowest mass red centrals, while having weak lensing masses greater than the expectation, are not significantly different.

see evidence for a bimodality in the halo masses of red and blue groups at a fixed stellar mass, in agreement with the results of Mandelbaum et al. (2016) and in disagreement with the results of Hudson et al. (2015).

Cui et al. (2021) use a set of simulations which successfully reproduce this bimodality to explore the root causes of this observation. They find that two components of their input physics are responsible for the phenomenon: jet-mode AGN feedback and X-ray AGN feedback. The jet-mode AGN feedback begins when the cold gas fraction is low, and the X-ray feedback begins later and removes the remaining star forming material, thus quenching and reddening the galaxy. After being quenched, the halo continues to grow, which leads to the observed bimodality.

To understand the impact of our choice of model, we choose to additionally perform fits without the offset halo component based on the mock profiles. We compare the ratios of the masses with the offset component to those without. We find that the inclusion of the offset profile reduces the masses of the blue groups to 26% of their mass without the offset component, while the masses of the red groups are reduced to 67% of their mass.

2.6 Conclusions

We derive an $n(z_s)$ estimate for the CFIS weak lensing survey by leveraging CFHTLenS photometry and an additional spectroscopic catalogue. We use the method of Hildebrandt et al. (2017) to reweight the spectroscopic catalogue until the distribution of sources matches that of CFIS. We then fit a simple model to this reweighted spectroscopic distribution to measure the redshift distribution of CFIS sources; a necessary component for a weak lensing survey with no photometric or spectroscopic redshifts.

We then validate our model for the source redshift distribution $n(z_s)$ by measuring the mass-richness relation using redMaPPer clusters with richnesses between $20 \leq \lambda < 140$ and redshifts between $0.1 \leq z < 0.33$ using the methodology of Simet et al. (2017). We fit the weak lensing profiles of these clusters, taking into account effects such as dilution, and halo projection and triaxiality. We then fit a simple model to the resulting masses to establish a mass-richness relation. The resulting mass-richness relation is in good agreement with that of Simet et al. (2017) as well as in broad agreement with the measurements from a variety of other surveys.

We then proceed to analyze the group catalogue of Tinker (2020b). We first split the group catalogue by the estimated halo masses. The resulting weak lensing profiles are then fit with a model including the effects of miscentring by estimating the offset profiles using the mock catalogues. We find that the estimated halo masses are in good agreement with the weak lensing

masses, except in the case where the estimated halo masses are in excess of $10^{14}\ M_{\odot}$. There is no evidence for dilution or a suppression of the signal due to strong lensing effects for these groups.

We then bin the Tinker (2020b) group catalogue by colour and stellar mass. Again, the mock catalogue is leveraged to estimate the contribution to the signal from miscentring. While the mass constraints on the groups with blue centrals are not strong, we find a systematic overestimation of the halo mass from the catalogue compared to the measured weak lensing masses. Additionally, we find evidence of bimodality in the halo masses of red and blue centrals at a fixed stellar mass, in agreement with the results of Mandelbaum et al. (2016).

2.7 Appendix

To demonstrate that the signals measured in this work are genuine and not the result of a strong systematic bias, we can compare them to the measured signals around the random points used to correct for dilution. Since the points were randomly selected, there should be no weak lensing signal observed around them. Figure 2.11 shows the mean tangential and cross components of the shapes of background sources around these random points. These signals are consistent with zero, indicating that that the signals measured in this work are truly the result of weak gravitational lensing induced by the clusters and groups being studied.

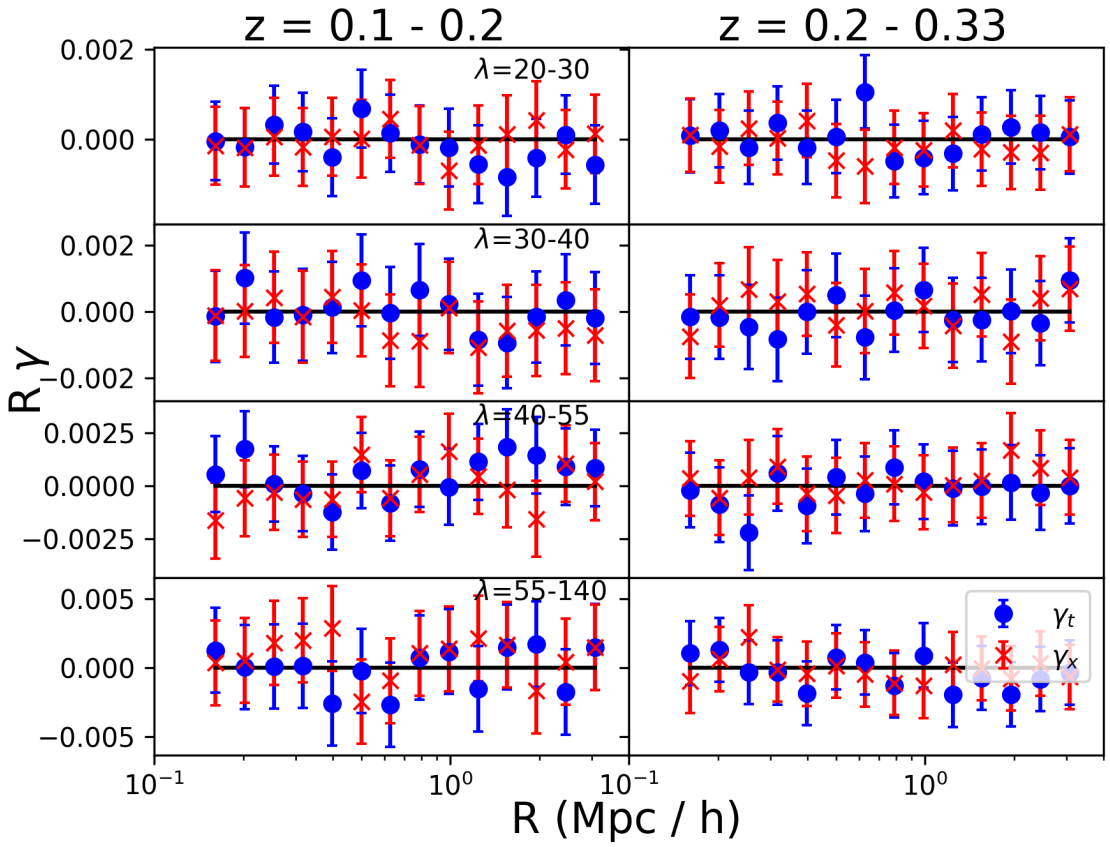

Figure 2.11: The tangential (blue dot) and cross (red cross) components of the γ signals measured around the random points for the redMaPPer clusters. Though these random points are not real lenses, and hence have no richness, the richness bins the random points were selected to correct for are shown.

Chapter 3

Satellites

3.1 Introduction

As galaxy groups accrete additional members, these satellite galaxies are subject to a series of interactions to which field galaxies are not subject. Ram pressure stripping, where the intracluster medium acts as a wind, strips away gas and dust from the infalling satellite galaxy. This effect was first discussed by Gunn & Gott (1972a) and has been observed many times since (e.g. Roberts et al. 2021b, Durret et al. 2021b). Tidal stripping occurs due to interactions with the host (group or cluster) halo. As the satellite passes through its pericentre point, it experiences its strongest tidal forces which strip material from the satellite subhalo. As most of the baryonic matter has sunk to the centre of the satellite's potential well, this tidal stripping primarily affects the dissipationless dark matter. This effect was first discussed in the context of globular clusters by von Hoerner (1957b), but a more thorough derivation in the context of satellite galaxies can be found in Read et al. (2006b). Harassment, whereby satellite galaxies are tidally heated by frequent, high speed interactions with other satellite galaxies (Moore et al., 1996b), can disrupt galaxy disks and strip away matter from dark matter haloes. The tidal heating of disks and dark matter haloes from harassment can therefore enhance tidal stripping in high density environments.

The quenching process can even begin before any material is stripped from the satellite subhalo. The subhalo, orbiting within the halo of the group, is dominated by the host halo and can no longer accrete star forming material. This cutoff of access to star forming material leads to the additional effect of quenching of star formation in satellite galaxies in group and cluster environments.

Weak gravitational lensing can be used to measure the distribution of matter around satellite subhaloes. Because it is sensitive to both baryonic and dark matter, it is a powerful technique for

measuring how galaxy group environments affect the subhaloes of the satellite members. Observationally, tidal stripping has been measured in rich clusters (Natarajan et al., 1998, Natarajan et al., 2002, Natarajan et al., 2009). In particular, Natarajan et al. (2002) found evidence of tidal stripping by examining satellite galaxies in massive galaxy clusters. Rich clusters were observed in the range of $0.17 \leq z \leq 0.58$ with archival data from the Hubble Space Telescope and strong and weak lensing were used to determine that the dark matter distribution in the inner regions of these clusters was smoothly distributed and a finite truncation radius was detected for the satellites.

Fang et al. (2016) observed rich clusters in the redMaPPer catalogue and found that many of the quenched satellites had been quenched prior to their accretion onto the cluster. This could potentially be explained by preprocessing of these cluster satellites by lower mass group environments before the group was accreted. Simulations additionally predict this tidal stripping effect at the smaller mass scales of galaxy groups (Joshi et al., 2019).

However, studies have attempted to observe preprocessing of cluster satellites by using weak lensing to study lower richness galaxy groups. Gillis et al. (2013), Li et al. (2014), and Sifón et al. (2015) all observed satellites in group environments with weak lensing. While satellite subhaloes were detectable and halo masses were obtained, statistically significant evidence for truncation radii of these group satellites has remained elusive.

Dynamical friction, the loss of momentum of an object as it passes through a field of less massive particles (Chandrasekhar, 1943), causes the orbits of satellite galaxies to decay as they travel through the dark matter and intracluster medium of their host haloes. As a result, we expect satellites that have spent the most time in the host halo to spend more time near the group centre, which in turn means we expect them to be more tidally stripped on average. We can therefore use the projected separation between the satellites and the group centres as a proxy for the infall time. By stacking satellite galaxies by that projected separation we expect to see that subhaloes with smaller separations have been more strongly stripped than satellite subhaloes at larger radii.

The dynamical friction force is proportional to the square of the satellite mass. This induces the complicating factor of mass segregation, whereby more massive satellites will sink to the centre of the groups on shorter timescales than their less massive counterparts (Contini et al., 2012, van den Bosch et al., 2015). This confuses the measurements described above as the effects of mass segregation and tidal stripping oppose each other when stacking satellites by projected separation. To account for the effect of mass segregation, we can use the stellar mass, which is relatively unaffected by tidal stripping, as a proxy for the infall mass. When measuring the stellar to halo mass relation as a function of the projected separation between satellite subhaloes and the group centres, we therefore anticipate ratios that decrease with increasing separation.

In this chapter, we make use of the group catalogue of Tinker (2020b) to measure the weak

lensing signal around satellite galaxies in group environments. We utilize a preliminary data release from the CFIS/UNIONS survey as our source catalogue. We then split the satellite sample into three bins of projected separation from the group centre to attempt to measure the effect of tidal stripping in these environments.

Gao et al. (2004) used simulations to analyze a population of satellite subhaloes. For satellites with the properties described in Table 3.2, we can use these simulations to make predictions about how much matter we expect to be retained after being tidally stripped. Using Gao et al. (2004), for the entire sample of satellites, we expect about ≈40% of the halo mass to be retained. For the satellites that have been binned by their projected separation from the group centre, the innermost bin should retain ≈15% of its halo mass, the middle bin should retain ≈35% of its halo mass, and the furthest bin from the group centre should retain ≈50% of its halo mass.

In Section 3.2, we provide a brief theoretical overview of weak gravitational lensing. In Section 3.3 we describe the data used to make the measurements, and we give a succinct overview of similar studies. In Section 3.4 we discuss the lens catalogue as well as the model used to fit a weak lensing signal from such lenses. We then present the results in Section 3.5, discuss them in Section 3.6, and offer our conclusions in Section 3.7.

Throughout this chapter, we adopt a flat ΛCDM cosmology with a Hubble parameter $h \equiv H_0/(100\ \mathrm{km\ s^{-1}\ Mpc^{-1}}) = 0.7$ and $\Omega_\mathrm{m} = 0.3$. The h dependence is included in all derived quantities throughout this work. Halo masses are defined as the mass within a radius where the density is 200 times the mean matter density ($M_{200\mathrm{m}}$).

3.2 Weak Gravitational Lensing

Light from distant background sources is distorted as it passes through the gravitational potentials from the galaxy groups and satellites being analyzed. The potentials cause a slight tangential shear in the shapes of the background sources. We can therefore examine the distribution of matter in these galaxy groups by measuring the tangential distortion they induce in the background sources. This distorting effect is sensitive to both baryonic and dark matter, making it a powerful probe of the dark sector.

Because light from the background sources is distorted by both the galaxy group halo, in addition to the subhaloes associated with the satellite galaxies hosted by the group, the distortion is more complex than for a single halo.

The tangential shear, γ_t, regardless of the number of lenses inducing it, can be expressed as

$$\gamma_\mathrm{t} = \frac{\Delta\Sigma}{\Sigma_\mathrm{cr}} \tag{3.1}$$

where $\Delta\Sigma$ is the excess surface density (ESD), and $\Sigma_{\rm cr}$ is the critical surface density. The excess surface density is defined as

$$\Delta\Sigma = \overline{\Sigma}(<R) - \Sigma(R) \tag{3.2}$$

where R is the projected separation between the lens and the background source on the sky. Because we will be analyzing satellite galaxies, there will be a $\Delta\Sigma$ signal associated with the satellite subhalo as well as an offset $\Delta\Sigma$ contribution from the host halo of the galaxy group. Section 3.4.2 will describe in greater detail how the $\Delta\Sigma$ signal from the offset group halo is modelled.

The critical surface mass density, which defines the separation between the strong and weak lensing regimes, is given by

$$\Sigma_{\rm cr}(z_{\rm l}, z_{\rm s}) = \frac{c^2}{4\pi G} \frac{D_{\rm A}(z_{\rm s})}{D_{\rm A}(z_{\rm l})\ D_{\rm A}(z_{\rm l}, z_{\rm s})} \tag{3.3}$$

where $D_{\rm A}(z_{\rm l})$, $D_{\rm A}(z_{\rm s})$, and $D_{\rm A}(z_{\rm l}, z_{\rm s})$ are the angular diameter distances to the lens, source, and between the lens and source respectively. For weak lensing, $\Delta\Sigma \ll \Sigma_{\rm cr}$, and therefore the induced shear, $\gamma_{\rm t}$, is small.

If the individual source redshifts are not known, the critical surface mass density can be altered to incorporate a probability density function, $n(z_{\rm s})$ that describes the overall redshift distribution of the background sources

$$\tilde{\Sigma}_{\rm cr}^{-1} = \frac{4\pi G}{c^2} \int_{z_{\rm l}}^{\infty} \frac{D_{\rm A}(z_{\rm l})\ D_{\rm A}(z_{\rm l}, z_{\rm s})}{D_{\rm A}(z_{\rm s})}\ n(z_{\rm s})\ dz_{\rm s} \tag{3.4}$$

Lens source pairs are given weights, $w_{\rm ls}$, defined as

$$w_{\rm ls} = w_{\rm s}\ \tilde{\Sigma}_{\rm cr}^{-2} \tag{3.5}$$

The weights used in this study are provided by the *lens*fit algorithm, which was used to measure the galaxy shapes. The excess surface mass density can then be written in terms of the observables as

$$\Delta\Sigma(r) = \frac{\Sigma_{\rm ls} w_{\rm ls} \gamma_{\rm t} \tilde{\Sigma}_{\rm cr,ls}}{\Sigma_{\rm ls} w_{\rm ls}} \tag{3.6}$$

For the uncertainty in $\Delta\Sigma$, we use the variance of our shape catalogue (described in Section 3.3). In general, the variance can be written as

$$\mathrm{Var}(\gamma_t) = \left(\frac{1}{\Sigma w_i}\right)^2 \Sigma w_i^2 \sigma_i^2 \tag{3.7}$$

where w_i is the *lens*fit weight assigned to a given galaxy shape, and σ_i is the variance of the ellipticity. For our catalogue, $\sigma_i^2 \equiv \frac{1}{2w_i}$, which reduces the variance to

$$\mathrm{Var}(\gamma_t) = \frac{1}{2\Sigma w_i} \,. \tag{3.8}$$

The uncertainty in the observed $\Delta\Sigma$ is then the variance, scaled by $\Sigma_{\rm cr}$.

3.3 CFIS

CFIS is a wide field imaging survey, with weak lensing being a primary science driver. The survey will ultimately contain $\sim$ 5000 square degrees of high quality, r-band weak lensing data. This work makes use of an internal release of the first 1,565 square degrees of weak lensing data.

For this work, we make use of the shape catalogue generated by ShapePipe, a Bayesian model fitting code that produces galaxy shapes (Guinot et al., submitted). ShapePipe also makes use of metacalibration to perform an initial calibration of the galaxy shapes (Sheldon & Huff, 2017). The initial release contains 40,151,119 usable sources with shape measurements. This is already comparable to the number of sources from much wider surveys, such as SDSS DR7 with 41,631,361 galaxies with shapes (Luo et al., 2018).

It should be noted that the number of objects is not the only advantage of the CFIS data. CFIS data is also deeper, providing a greater fraction of sources at large distances. This increases $\Sigma_{\rm cr}$, boosting the excess surface mass density signal (Equations 3.4 and 3.6).

This gives CFIS a distinct advantage over previous weak lensing surveys, especially when it comes to subtle effects such as the tidal stripping of satellite galaxies.

This work has several advantages over these previous studies. In addition to the advantages associated with the CFIS survey above, CFIS also has significant overlap with the SDSS catalogue, which provides us with the ability to utilize large catalogues of galaxy groups, such as the Tinker (2020b) group catalogue used in this work. This group catalogue comes with several advantages of its own. The catalogue was assembled using a more refined group finding algorithm that results in a more pure sample of galaxy groups. Additionally, the group catalogue also comes with a catalogue of mocks, allowing us to directly estimate the weak lensing contribution from the offset halo component, thus contributing to a better estimate of the satellite dark matter halo.

Bin (h^{-1} **kpc**)	**<Separation>** (h^{-1} **kpc**)	$\mathbf{N}_{\mathrm{lenses}}$	$\log\langle\frac{M_{\mathrm{h,sat}}}{h^{-1}M_\odot}\rangle$	$\log\langle\frac{M_{\mathrm{h,host}}}{h^{-1}M_\odot}\rangle$	$< z >$	$\log\langle\frac{M_*}{M_\odot}\rangle$	$\log\langle\frac{L}{L_\odot}\rangle$
All	476.6	12248	12.01	14.26	0.074	10.83	10.11
(0, 254]	134.4	4169	12.00	14.05	0.068	10.78	10.14
(254, 566]	398.0	4136	12.00	14.16	0.073	10.81	10.06
(566, ∞]	920.8	3943	12.01	14.47	0.081	10.89	10.13

Table 3.1: Properties of satellite galaxies before and after binning by their projected separation from the group centre. These are the means of the values provided by the Tinker (2020b) catalogue.

3.4 Satellite Galaxies as Lenses: Data and Model

3.4.1 Satellites from the Tinker group catalogue

We select satellite galaxies from the group catalogue of Tinker (2020b). We select satellite galaxies from groups with five or more satellites by cutting with N_sat ≥ 5. The properties of this satellite sample are presented in Figure 3.1 and Table 3.2.

There are 12,248 satellites in total (log $\langle\frac{M_*}{M_\odot}\rangle$=10.83), with 3,063 being star forming (log $\langle\frac{M_*}{M_\odot}\rangle$=10.33) and 9,185 being quenched (log $\langle\frac{M_*}{M_\odot}\rangle$=10.66). For the total sample log $\langle\frac{M_h}{h^{-1}M_\odot}\rangle$ = 12.58, for the star forming sample log $\langle\frac{M_h}{h^{-1}M_\odot}\rangle$ = 11.17, and for the quenched sample log $\langle\frac{M_h}{h^{-1}M_\odot}\rangle$ = 11.79.

Since the dark matter subhalo is more extended than the stars of the satellite galaxy and therefore is preferentially stripped, we can use the stellar mass of the satellite to estimate the pre-infall dark matter halo mass. To accomplish this, we make use of the stellar-to-halo mass relation of Chapter 2 (Figure 2.10) to convert the stellar mass provided in the group catalogue to a corresponding pre-infall halo mass, $M_{\mathrm{h,max}}$. Using this relation, we derive a pre-infall halo mass for the star forming satellite population of log $\langle\frac{M_{\mathrm{h,max}}}{h^{-1}M_\odot}\rangle$ = 11.85. For the population of quenched satellites, we find log $\langle\frac{M_{\mathrm{h,max}}}{h^{-1}M_\odot}\rangle$ = 12.22. A histogram of $\langle\frac{M_{\mathrm{h,max}}}{h^{-1}M_\odot}\rangle$ is shown in Figure 3.1.

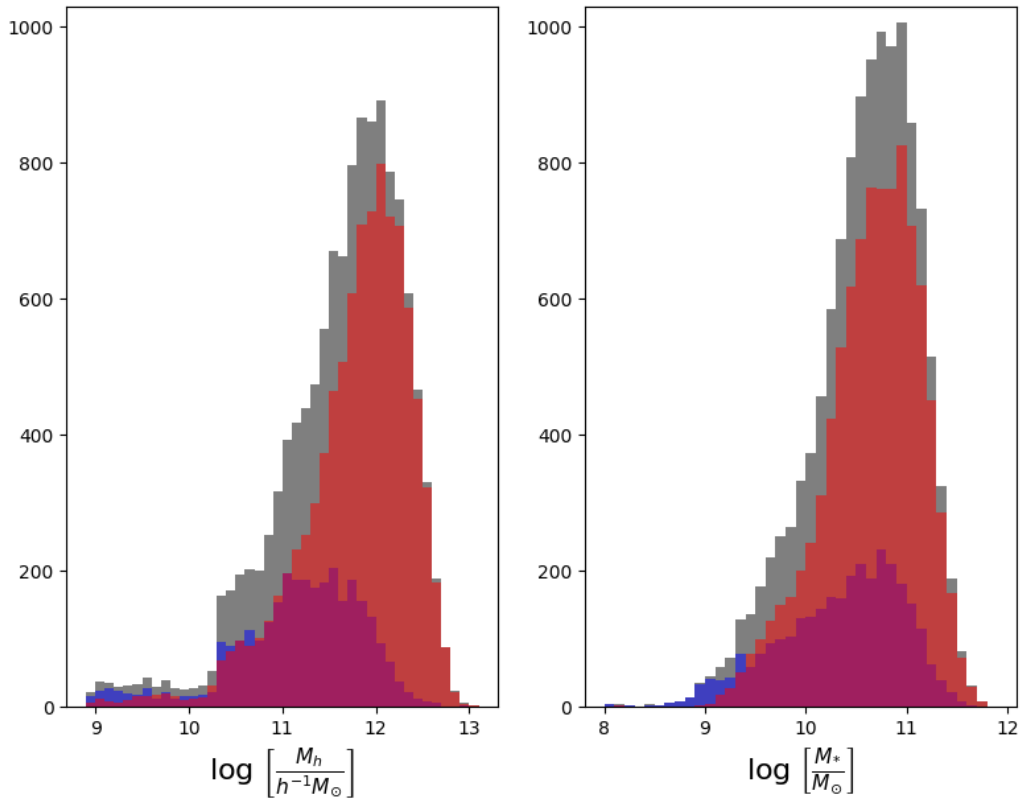

Figure 3.1: Left: Distribution of pre-infall satellite halo masses as estimated from their stellar mass for the sample of satellite galaxies in the Tinker (2020b) catalogue which overlap with CFIS. The red and blue histograms represent the halo mass distribution for the quenched and star forming satellites respectively, while the black histogram is the total distribution. Right: The distribution of stellar masses for quenched (red) and star forming (blue) satellites.

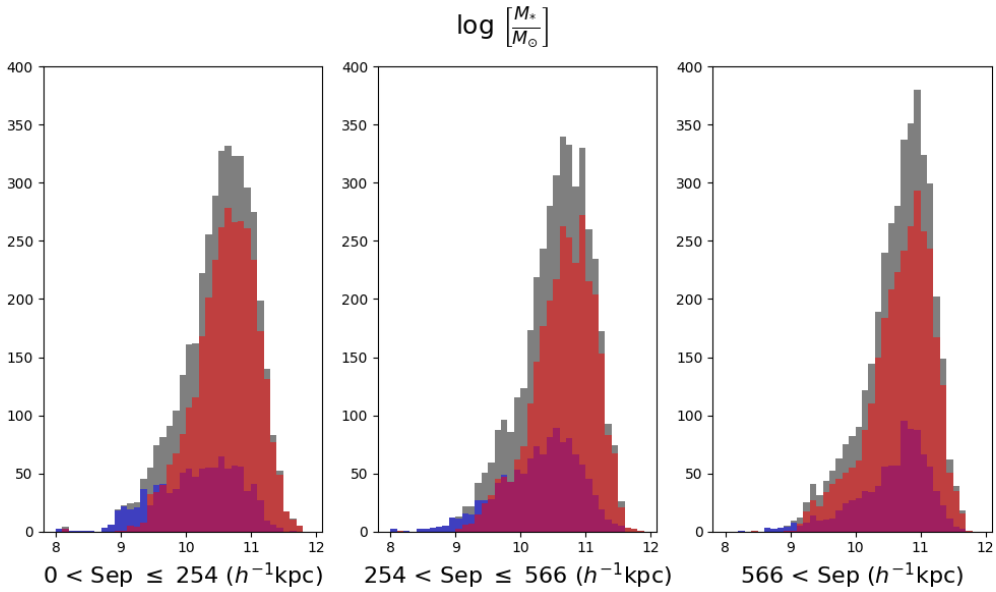

Figure 3.2: Distribution of stellar masses of the satellite galaxies after being binned by their projected separation from the group centre.

3.4.2 Model for Weak Lensing by Satellites

We fit $\Delta\Sigma$ with a combination of different models. The first is a simple non-truncated profile consisting of an NFW profile for the satellite subhalo and an offset profile designed to account for the group halo.

The offset group component is calculated using the mock catalogue for the Tinker (2020b) groups. For each satellite in the mock catalogue, we find the most massive object within a $3h^{-1}$Mpc projected radius. We then generate an offset NFW profile for each of these objects using the following equation:

$$\bar{\Sigma}_{\rm OH}(R|R_{\rm OH}) = \frac{1}{2\pi}\int_0^{2\pi} {\rm d}\theta\, \Sigma_{\rm NFW}\left(\sqrt{R_{\rm OH}^2 + R^2 + 2RR_{\rm OH}\cos\theta}\right) .$$

The mean of each of these offset halo profiles is then calculated, and the overall $\Delta\Sigma$ signal is calculated with Equation 3.2. Figure 3.4 visualizes the $\Delta\Sigma$ contribution from offset haloes.

To complete the model, we generate a third component to account for the stellar mass of the satellite galaxy. This is modeled with the stellar mass from the group catalogue:

$$\Delta\Sigma_* = \frac{M_*}{\pi R^2} .$$

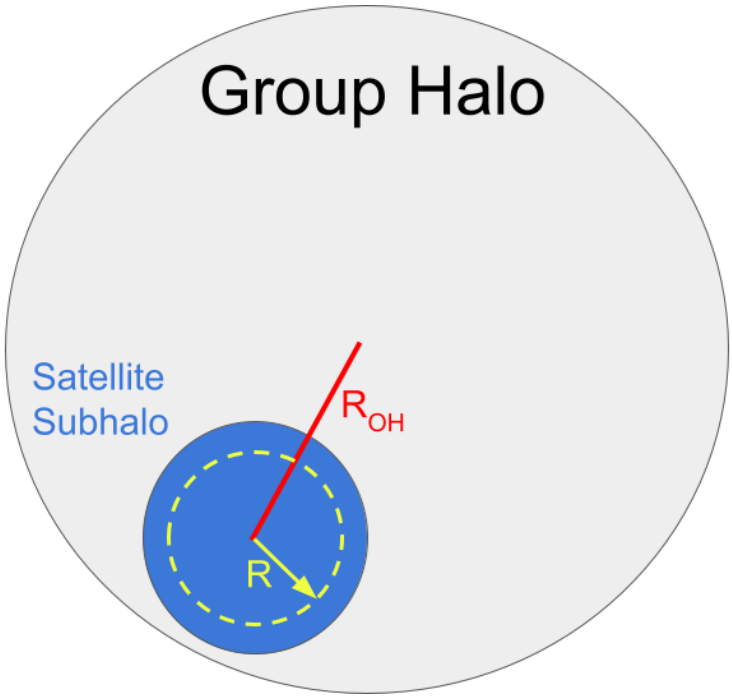

Figure 3.3: Diagram explaining the calculation of the offset NFW term (Equation 3.4.2). The group halo is indicated in grey, while the satellite subhalo orbiting within the group halo is in blue. R_{OH} (red line) shows the offset between the centre of the group halo and the centre of the satellite subhalo. R, (green circle/arrow) is the radius at which the offset contribution is calculated at. Because we want the offset group contribution for a range of radii, we evaluate the integral of Equation 3.4.2 for each radial bin in the fits.

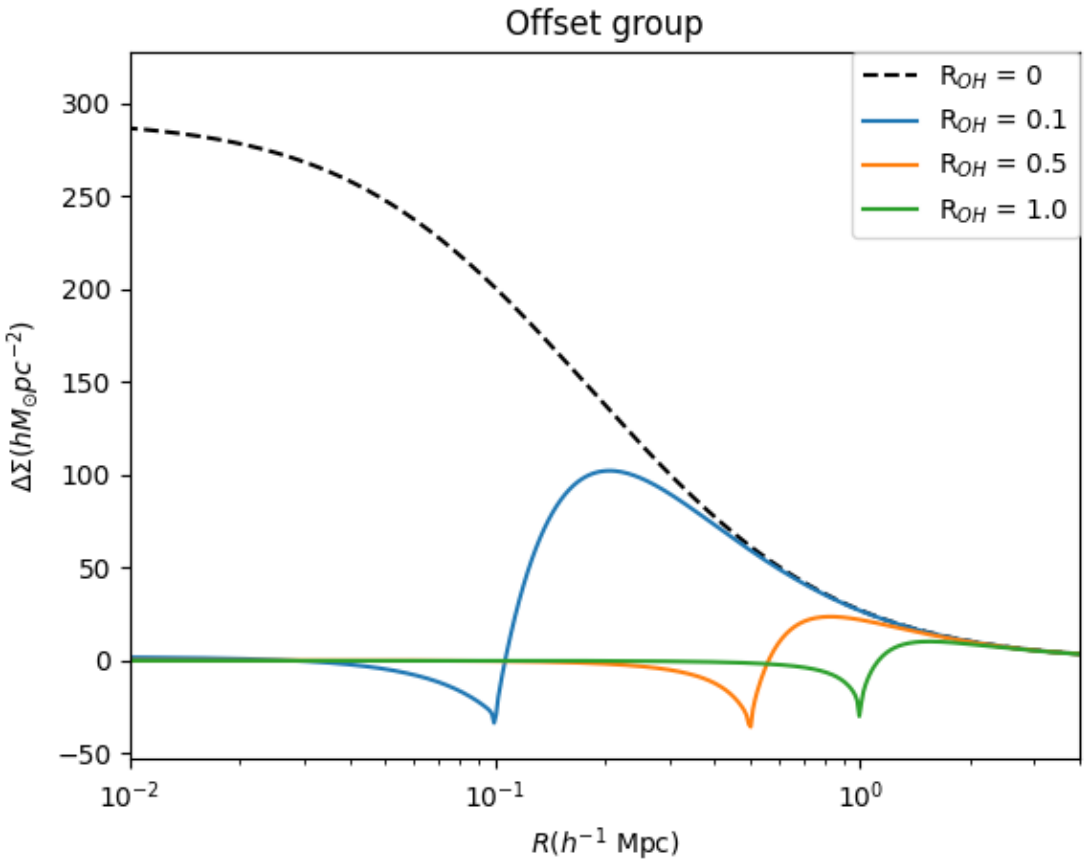

Figure 3.4: $\Delta\Sigma$ contribution from haloes at various R_{OH} offsets. An R_{OH} of 0 is equivalent to a centred NFW.

The complete model therefore consists of the addition of the NFW subhalo component, the offset NFW group term, and the stellar mass term. The data was fit out to the point where the offset group term becomes dominant, in order to avoid fitting contributions to the $\Delta\Sigma$ signal from contaminating effects from nearby structures. We test the sensitivity of the fit to this choice of fitting radius and discuss the effect it has on the measured parameters in Section 3.5.2.

Because we are attempting to measure the truncation radius due to tidal stripping for these satellites, we must also fit for this. Here, we additionally fit with the stripping model of Mandelbaum et al. (2006), which modifies the satellite subhalo term beyond some radius $R_{\rm trunc}$ as follows:

$$\Delta\Sigma(R \geq R_{\rm trunc}) = \frac{\Delta\Sigma(R_{\rm trunc})}{(R/R_{\rm trunc})^{-2}} \,. \tag{3.9}$$

We use this modification of the subhalo term in two different additional models beyond the nontruncated fit. The signal is therefore fit with 3 different combinations of free parameters. The first fit uses the halo mass as the free parameter, while no truncation radius is applied. The second fit uses both the halo mass and the truncation radius as free parameters. The third and final fit fixes the halo mass and fits a truncation radius. In this scenario, the mean stellar mass for the satellites is calculated using the group catalogue, then the expected halo mass is interpolated by assuming the stellar to halo mass relation for centrals from Chapter 2.

A fourth fit where the truncation radius is not fit and the halo mass is fixed to 0 $M_\odot$ is also applied but not shown. This is calculated for the sole purpose of statistically determining how strong the satellite detection is. All four of the fits described here include the fixed contributions from the stellar component and the offset group component.

3.5 Results

3.5.1 All Satellites

The signal for all satellites, regardless of projected separation from the group centre, is shown in Figure 3.5. This signal is then fit with the models described in Section 3.4.2.

All 3 models with a satellite dark matter subhalo component are a good fit to the data. The model with no satellite dark matter subhalo, i.e. 100% stripping, is ruled out at 2.7σ. Additionally, the masses derived from the two fits where the satellite dark matter halo mass is a free parameter ($\log\langle\frac{M}{h^{-1}M_\odot}\rangle = 12.48^{+0.15}_{-0.19}$ and $\log\langle\frac{M}{h^{-1}M_\odot}\rangle = 12.48^{+0.18}_{-0.21}$) are in good agreement with the expected mass from the model where this parameter was fixed to the value obtained from centrals ($\log\langle\frac{M}{h^{-1}M_\odot}\rangle = 12.42$).

Bin (h^{-1} **kpc**)	**<Separation>** (h^{-1} **kpc**)	**Fit 1** (h^{-1} **Mpc**)	**Fit 2** (h^{-1} **Mpc**)	**Fit 3** (h^{-1} **Mpc**)
All	476.6	$\log\langle\frac{M}{h^{-1}M_\odot}\rangle=12.48^{+0.15}_{-0.19}$ $R_{trunc}=\infty$ χ^2=6.77 dof=8	$\log\langle\frac{M}{h^{-1}M_\odot}\rangle=12.48^{+0.18}_{-0.21}$ $R_{trunc}>0.18$ $\chi^2=6.77$ dof=7	$\log\langle\frac{M}{h^{-1}M_\odot}\rangle=12.42$ $R_{trunc}>0.19$ $\chi^2=6.88$ dof=8
(0, 254]	134.4	$\log\langle\frac{M}{h^{-1}M_\odot}\rangle=12.48^{+0.41}_{-0.63}$ $R_{trunc}=\infty$ $\chi^2=5.28$ dof=9	$\log\langle\frac{M}{h^{-1}M_\odot}\rangle=12.29^{+0.70}_{-1.06}$ $R_{trunc}=0.10^{+0.06}_{-0.06}$ $\chi^2=5.4$ dof=8	$\log\langle\frac{M}{h^{-1}M_\odot}\rangle=12.39$ $R_{trunc}>0.03$ $\chi^2=5.3$ dof=9
(254, 566]	398.0	$\log\langle\frac{M}{h^{-1}M_\odot}\rangle=12.09^{+0.44}_{-0.94}$ $R_{trunc}=\infty$ $\chi^2=17.82$ dof=12	$\log\langle\frac{M}{h^{-1}M_\odot}\rangle=11.63^{+0.75}_{-1.01}$ $R_{trunc}=0.14^{+0.09}_{-0.09}$ $\chi^2=18.3$ dof=11	$\log\langle\frac{M}{h^{-1}M_\odot}\rangle=12.41$ $R_{trunc}>0.01$ $\chi^2=18.3$ dof=12
(566, ∞]	920.8	$\log\langle\frac{M}{h^{-1}M_\odot}\rangle=12.18^{+0.36}_{-0.65}$ $R_{trunc}=\infty$ $\chi^2=12.81$ dof=14	$\log\langle\frac{M}{h^{-1}M_\odot}\rangle=11.97^{+0.60}_{-1.04}$ $R_{trunc}=0.16^{+0.12}_{-0.09}$ $\chi^2=12.8$ dof=13	$\log\langle\frac{M}{h^{-1}M_\odot}\rangle=12.48$ $R_{trunc}=0.11^{+0.07}_{-0.06}$ $\chi^2=11.9$ dof=14

Table 3.2: Fits to the weak lensing satellite signal using the three models described in Section 3.4.2. The first row contains the fits for the total sample of unbinned satellites, while the remaining three rows are for the satellites after being binned by projected separation from the group centre. Fit 1 is the model with mass as the only free parameter. In Fit 2, both mass and truncation radius are free parameters. In Fit 3, the mass is fixed, and the truncation radius is the only free parameter. For cases where the truncation radius was consistent with the maximum radius with which we fit, we quote only a lower limit. The χ^2 and number of degrees of freedom for each fit are shown as well.

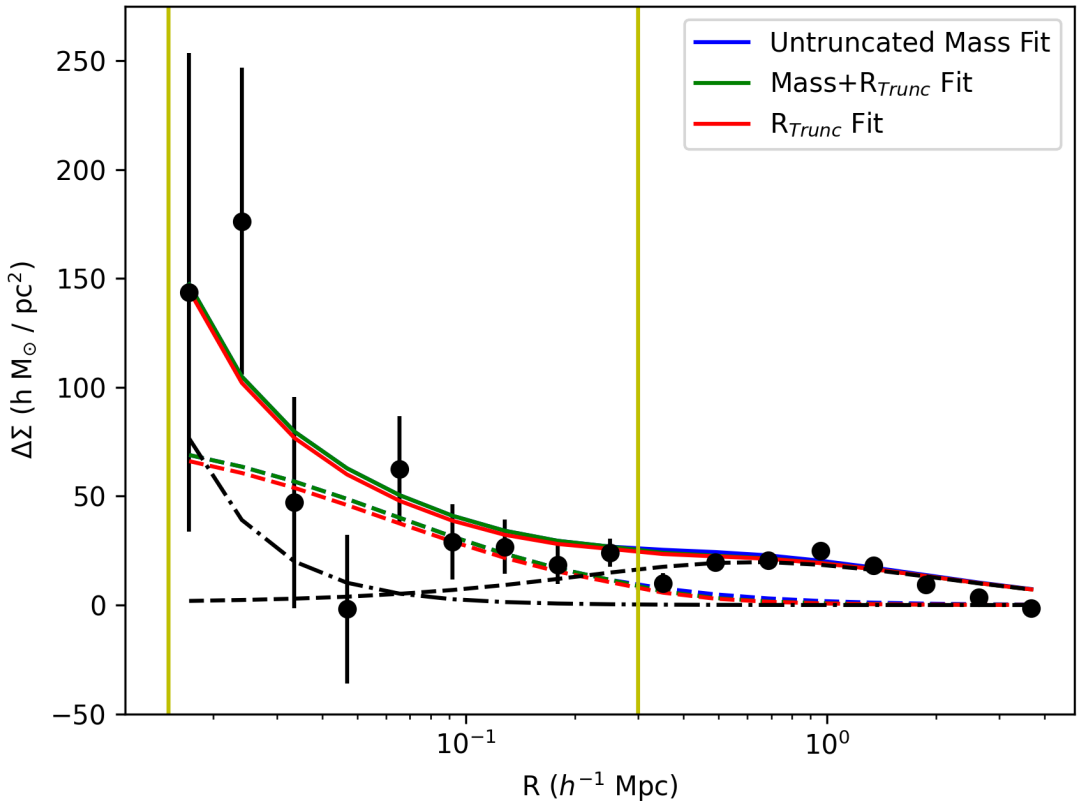

Figure 3.5: Weak lensing signal for all satellite galaxies in the Tinker (2020b) group catalogue with the three fits overlaid. The solid lines are the sums of all of the model components. The dashed coloured lines are the contributions from the satellite subhaloes, the black dashed line is the offset group term, and the dash-dotted line is the stellar component. The vertical yellow lines indicate the range of data that was fit with each model. All satellites belong to groups with N_sat $\geq$ 5 and have P_SAT > 0.5

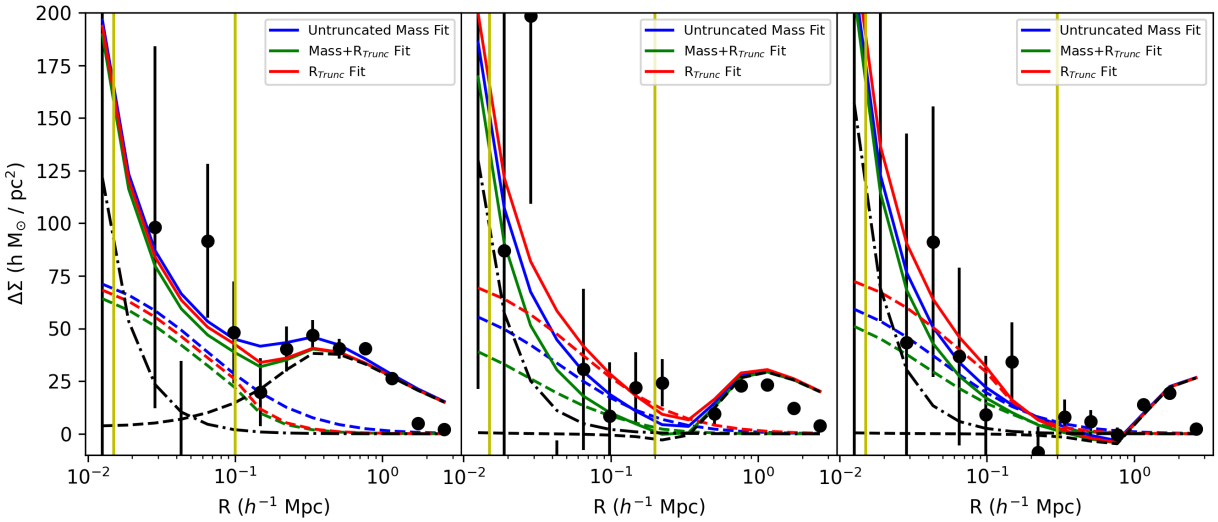

Figure 3.6: Weak lensing signal for satellite galaxies in the Tinker (2020b) group catalogue after being binned by their projected separation from the group centre. Left: The satellites with the smallest projected separations ($R_{\rm sep} \leq 254h^{-1}$ kpc). Middle: The satellites with $254 < R_{\rm sep} \leq 566h^{-1}$ kpc. Right: The satellites with the largest projected separations ($R_{\rm sep} > 566h^{-1}$ kpc). The vertical yellow lines indicate the range of data that was fit with each model.

Lens properties, as well as the results from fitting the various models, are shown in Table 3.2. The measured truncation radius is $R_{\rm trunc} > 0.19h^{-1}$ Mpc for the second model and $R_{\rm trunc} > 0.18h^{-1}$ Mpc for the third model. Note that that the models only fit the data out to $\approx 0.3h^{-1}$ Mpc, a truncation radius that is consistent with 0.3 h^{-1} Mpc means that no statistically significant upper limit can be placed on truncation due to tidal stripping.

3.5.2 Satellites Binned by Separation from Central

To attempt to measure the effects of tidal stripping on these satellite haloes, we additionally bin them by their projected separation from their respective group centres. We define the bin edges by selecting radii that provide us with three radial bins with an equal number of satellites in each bin. Not all satellites in the CFIS footprint have lens source pairs however, which results in slightly different numbers of satellites per bin. Details for each bin can be found in Table 3.2.

In this case, the uncertainties in the mass of the satellite dark matter halo are significantly larger than in the unbinned scenario due to the reduction in the number of objects per bin. Additionally, when we fit the bins with the 2 larger projected separations with a satellite halo

mass fixed to 0 $M_\odot$, the fit is statistically not significantly worse than the fits shown in Figure 3.5, questioning whether a signal from the satellites is even detectable at all in these bins.

We made two attempts at compensating for the reduction in the sample size per bin. The first was to change maximum fitting radius. Since the signal is stronger at larger radii due to the increase in the number of background sources, we thought including extra data points may improve the fit. However, reducing or increasing the number of data points in the fit showed no statistical improvement.

Additionally, we tried improving the purity of the sample by placing stricter constraints on which objects were considered satellites. To do this, we simply changed the P_SAT value from the Tinker (2020b) catalogue for which we consider an object a satellite. By increasing this value from the nominal 0.5, to 0.6, 0.7, 0.8, and 0.9, we decrease the number of satellites per bin, but hopefully increase the signal by rejecting more false positives from the satellite sample. As with adjusting the number of data points fit, adjusting the purity of the sample offered no improvement to satellite fits, as the increase in the sample purity was offset by the reduced sample size.

3.6 Discussion

When all satellites in the catalogue are binned together, regardless of projected separation from the group centre, we obtain $\Delta\Sigma$ profiles that are sufficient to place a statistically significant constraint on the subhalo mass and truncation radius. By comparing the fitted models to a model with no dark matter halo, we find that the dark matter halo mass is detected at the 2.7σ level. Additionally, we obtain the same satellite halo mass for both models with mass as a free parameter, and find that the mass is in agreement with the prediction from the group catalogue.

However, by binning the satellites by projected separation from the group centre, the noise increases. Of the three bins, the only one with a signal strong enough to detect the contribution from the satellite halo is the innermost bin. For this bin, we can rule out the zero mass model at the $\sim 2\sigma$ level. When applying the zero mass model to the more separated bins, we find χ^2 values that are quite comparable to those of our other models. Overall, we fail to detect statistically significant evidence of tidal stripping in satellite groups due to the increase in noise when binning the satellites by projected separation from the group centre. The strength of our signal is comparable to that of Sifón et al. (2015) despite having a larger weak lensing catalogue with which to work. This is likely due to the lack of photometric redshift estimates which would help separate genuine background sources from foreground objects.

In order to determine the effects of contamination from galaxies that are erroneously listed as satellites, we also apply various cuts on the probability that a given galaxy is truly a satellite

by cutting on the P_SAT parameter. As Tinker (2020b) uses 0.5 as the threshold for the P_SAT parameter for classifying galaxies as satellites, we first cut on that value, and then additionally cut on 0.6, 0.7, 0.8, and 0.9 and examine how that affects the measured weak lensing signal of the stacked lenses. While these higher cuts increase the purity of the satellite galaxy sample, they also further reduce the number of lenses in each bin. We find that the increase in purity is not sufficient to offset this reduction in numbers, and the resulting fits were less significant than with the original threshold.

Despite the lack of detection of the tidal stripping of satellite subhaloes in galaxy groups, we can still place some constraints on the truncation radius. We vary the truncation radius of the various models applied to all satellites until the χ^2 increases by 4 to determine the 2σ lower limit. We find that we can rule out a truncation radius smaller than 17 h^{-1} kpc at the 2σ confidence level. This value is comparable to the ~15 kpc radius Natarajan et al. (1998) found that encompassed most of the total mass of L^* galaxies in massive clusters.

We additionally note that the offset profiles we use in the fitting process are not a great fit to the weak lensing signal, especially at large radii. Given the non-detection of tidal stripping, the weakness of the signal strength, and the fact that we don't fit the signal to any data points where the offset group term is dominant, we elect to ignore this issue in this work. However, this highlights the importance of realistic mock group catalogues. As weak lensing surveys continue to grow, and group catalogues continue to improve, signals will become stronger and the offset group term will need to be more accurately modelled than can be done here.

3.7 Conclusions

We use the SDSS group catalogue of Tinker (2020b) to observe the weak lensing signal around satellite galaxies in group environments in an attempt to measure the tidal stripping of these objects.

For the entire sample of satellites, we find a satellite subhalo mass in good agreement with the expectation from the stellar-mass-to-halo-mass relation of central galaxies drawn from the same catalogue. Additionally, we place a 2σ lower limit on the truncation radius of 17 h^{-1} kpc.

We then attempt to measure the truncation radius as a function of the projected separation from the group centre by binning the satellites. With the satellites binned, the strength of the signal decreases significantly. We were only able to detect the weak lensing signal contributed by the satellite dark matter haloes in one of the 3 bins of projected separation. We try to improve the signal by improving the purity of the satellite sample, but any improvement in the signal is offset by the decrease in the number of lenses. We also attempt to improve the fit by fitting the data

out to different radii, but this does not improve the quality of the fits to a statistically significant degree.

Future studies can potentially fare better with improved group catalogues and additional weak lensing data. The group catalogue used in this work is based upon SDSS data, but the deeper DESI survey (DESI Collaboration et al., 2016) should result in an order of magnitude larger sample of galaxy groups and satellites. Additionally, this work was completed with the internal "version 0" release of the first 1,565 square degrees of CFIS weak lensing data. Ultimately, the survey should produce approximately 5,000 square degrees of high quality weak lensing data, expanding the overlap between the source catalogue and existing group catalogues, providing a much larger sample of satellites with which to work. This will allow us to place tighter constraints on satellite masses, even after being binned by projected separation from the group centre.

Chapter 4

Simulations

4.1 Introduction

Weak gravitational lensing is a powerful tool for probing the matter distribution in the universe. Both baryonic and dark matter induce a distortion in the observed shape of distant background galaxies. Correlations in the shapes of these distant background galaxies can therefore tell us about the mass distribution in the universe from galactic scales up to the large scale structure of the universe.

Cosmic shear, the weak gravitational lensing due to the large scale structure of the universe, is a very demanding application of this technique. It generally requires the shapes of the background sources to be measured with better than one percent accuracy. While there are a variety of techniques for measuring galaxy shapes, none surpass the required threshold without some form of external calibration.

The solution to this problem requires simulations of weak lensing observations. By simulating weak lensing observations, the input galaxy shapes are known in advance and can then be compared to the measured shape to determine the bias of the shape measurements.

In practice, there are many additional complicating factors that can induce shape measurement biases. Light from these distant background source galaxies passes through the atmosphere, which blurs the observations and circularizes the observed galaxy shape, destroying some of the shape information. That light is then pixelised onto a CCD. Additionally, since it's the background sources that contain the information, the images of these faint sources are very noisy. All of these factors make measuring shapes on a given image difficult.

Beyond that, there are also factors relating to the weak lensing survey itself that can induce bias. The depth of the survey affects the effective number density of sources, which affects the number of blended sources you expect to observe. If two galaxies blend together and are detected as a single object, attempts to measure its shape will produce spurious results. The number of stars observed can also impact how well you can model the PSF, which determines how well the original galaxy shape can be recovered after attempting to correct for the blurring effect of the atmosphere. Even the unique distortions of the camera used to take the observations can impact the measurement bias.

It is therefore a good strategy when calibrating shape measurement pipelines to produce a set of simulated observations that reproduce the properties of the weak lensing survey as closely as possible. STEP (Heymans et al., 2006b; Massey et al., 2007) and GREAT (Bridle et al., 2010; Kitching et al., 2010; Mandelbaum et al., 2014) began this process by producing a set of survey-agnostic simulated galaxy observations. These were generated for shape measurement competitions and were relatively simple.

Future simulation work focussed on the calibration of specific weak lensing surveys. Fenech Conti et al. (2017) generated a mock survey with catalogue properties intended to emulate the KiDS survey as closely as possible. Galaxy properties were determined parametrically, however, and the galaxies were randomly distributed across the field. Kannawadi et al. (2019) expanded on the simulations by specifically addressing those issues. Galaxy properties were taken directly from the COSMOS galaxy catalogue (Griffith et al., 2012). Thus, any correlations between galaxy magnitudes, sizes, and ellipticities was automatically accounted for, and the clustering of galaxies was accurately represented.

As demonstrated in Hoekstra et al. (2017), there are many sources of bias that can arise from utilizing an improper distribution of galaxy properties. Galaxy sizes can affect the bias, as large galaxies are less affected by the circularization due to the PSF. Fluctuations in the density of sources can also induce bias by affecting the number of blended sources and close pairs (Figure 4.3). It's therefore important to capture the clustering of sources by using accurate positional information in simulations. Galaxies that are too faint to be detected in the weak lensing survey can also create bias. These undetected galaxies, given their large numbers, are often blended with brighter galaxies or bias the background estimation of nearby detected galaxies. Ellipticity can also play a role in inducing bias as less elliptical galaxies are more strongly affected by the input shear. Additionally, there are correlations between each of these properties, so ensuring an accurate distribution of galaxy properties when creating simulations is of critical importance. Idealized simulations with postage stamps of individual galaxies cannot capture all of these sources of bias. Instead, we must replicate the observing conditions of the CFIS survey as closely as possible.

We describe here the set of simulations generated to calibrate the CFIS/UNIONS weak lensing survey. These simulations take the added step of accurately recreating the unique observing strategy of the CFIS/UNIONS survey, as well as improving the astrometric modeling by incorporating the actual camera distortions from CFIS/UNIONS observations.

4.2 CFIS

CFIS is an imaging survey, with a large r-band component with weak lensing as a primary science focus. With a goal of 5,000 square degrees of weak lensing data with excellent photometric quality, CFIS aims to surpass prior northern hemisphere weak lensing surveys such as KiDS (de Jong et al., 2013).

The CFIS observations are processed by two independent shape measurement pipelines. The first pipeline uses the model fitting approach, with *lens*fit (Miller et al., 2007a) as its core shape measurement algorithm. The second pipeline, ShapePipe (Guinot et al., in prep), uses a combination of the `ngmix` [1] software and metacalibration (Sheldon & Huff, 2017). `ngmix` fits a Gaussian model to the galaxy images to determine their shape, then metacalibration is applied for a preliminary calibration of the shape measurements. Given that ShapePipe already incorporates a form of bias calibration, we will focus on the analysis and bias correction for the *lens*fit catalogue here.

4.2.1 Bias

Bias in weak lensing surveys is generally expressed in terms of a multiplicative component, m, and an additive component, c as follows

$$e_{\rm obs} = (1 + m)[\gamma + e_{\rm int}] + c \tag{4.1}$$

Here $e_{\rm obs}$ is the observed galaxy shape, $e_{\rm int}$ is the intrinsic galaxy shape, and γ is the shear. By examining the measured shapes from a real survey, the additive component of the bias can be estimated, but not the multiplicative component, which will average to zero for all shapes. It is therefore necessary to estimate these biases by using simulations.

In the absence of some external source of bias, we expect that by averaging the millions of galaxies in the catalogue, the mean of the two-component ellipticity (e_1 and e_2) should be consistent with zero. The mean shape of the 83 million objects in the preliminary "version 0"

[1] https://github.com/esheldon/ngmix

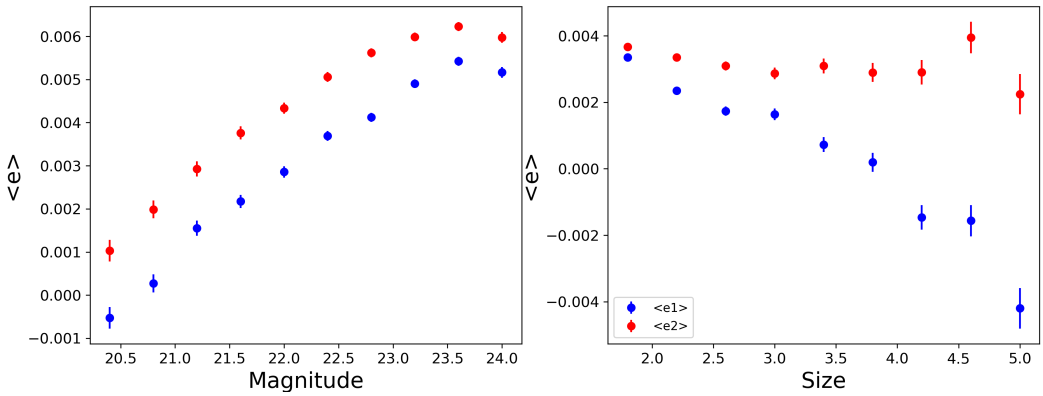

Figure 4.1: Left: The mean e_1 and e_2 components of CFIS galaxy shapes as a function of their r-band magnitude. While reasonably bright objects are relatively unbiased, the faint objects that make up the bulk of the population of background objects used in weak lensing analyses are significantly biased. While the severity of the bias is significant, e_1 and e_2 show similar trends. Right: The mean e_1 and e_2 components of CFIS galaxy shapes as a function of their measured size. Smaller objects have a significant positive e_1 component while larger objects are biased negatively. The second component, e_2, remains positively biased regardless of galaxy size.

release of the *lens*fit catalogue is $e = (3.8\text{e}{-3} \pm 3\text{e}{-5}, 4.8\text{e}{-3} \pm 3\text{e}{-5})$, clearly indicating that the shape measurement pipeline is not free of additive bias. We can also examine the additive bias as a function of the observed brightness of the objects. We therefore calculate the mean e_1 and e_2 components of their shapes as a function of their magnitude, as measured by the `MAG_BEST` parameter from Sextractor (Bertin & Arnouts, 1996) which the pipeline uses for object detection. This relation is plotted in Figure 4.1.

Both components of the galaxy shapes increase as the objects get fainter. Additionally, while the bias of both e_1 and e_2 increase at similar rates, the magnitude of the bias is significantly different, with the e_2 component being more strongly biased than the e_1 component. While the source of this difference between the e_1 and e_2 components is currently unknown, the advantage of using realistic simulations is that imaging properties can be altered to better understand how these biases arise. This will be discussed in further detail in Section 4.5.

We additionally check for any correlations between the shape components and the size of the galaxies. We therefore take the mean e_1 and e_2 components as a function of their size as measured by the `original_scalelength` Sextractor parameter (Figure 4.1). As with magnitude, both shape components are significantly biased, but with size, we observe that the e_1 and e_2 components are biased in very different ways. The first shape component, e_1, is positively biased at small

sizes, and eventually becomes negatively biased at large sizes. The second shape component, e_2, on the other hand, is positively biased at all sizes. Biases as a function of magnitude and size are a topic that is also explored using the CFHTLenS survey in Heymans et al. (2012). It is important to note that the CFHTLenS shape catalogue was also generated using the *lens*fit pipeline. They also found that small objects contributed more to the additive bias for the e_2 measurements than large objects. These biases, therefore, may not be a generic property of shape measurement algorithms, but may specifically be associated with the shape measurement algorithm used in these surveys. Regardless, these biases are very statistically significant and it's clear that they must be corrected for.

We also find that there is some spatial dependence to the biases. We calculate the mean of the e_1 and e_2 components within given regions of the sky (top row of Figure 4.2). Some of the more extremely biased regions are located on the edge of the CFIS footprint. These occur when there are very few sources in a given bin and should be ignored. However, even in the more well sampled regions of the footprint, there is a spatial dependence on the bias. It should be noted that the CFIS survey was designed to be uniformly deep. The exposures were intended to be halted once a specific signal to noise ratio was reached, with minimum and maximum exposure times of 100 and 300 seconds. Despite this, there are still some noticeable depth variations across the survey. Given that there is an additive bias that depends on the magnitude of the sources, it is perhaps unsurprising that deeper regions of the survey (with a larger number of more strongly biased sources) would result in this kind of spatial dependence.

Finally, we also examine the PSF variation across the CFIS footprint (bottom row of Figure 4.2). Since source shapes are convolved with the PSF as the light passes through the Earth's atmosphere, the PSF must be estimated and sources must be deconvolved with this estimate before the shape is measured. It is therefore important to understand how the PSF varies when simulating the survey. Here, we see more polarized e_1 components of the PSF with large, sudden changes between neighboring regions of the survey. The second shape component, e_2, in comparison, shows much more subtle variation across the CFIS footprint. There is also some evidence of "PSF leakage", the transfer of the shape of the PSF onto the observed shape of the galaxies, i.e. regions with positive e components in the galaxy map are correlated with regions of positive e components in the PSF map.

4.3 Simulations

To calibrate out the multiplicative and additive bias, we generate artificial observations. These simulations contain a PSF, which is convolved with the source galaxies, and an artificial shear is

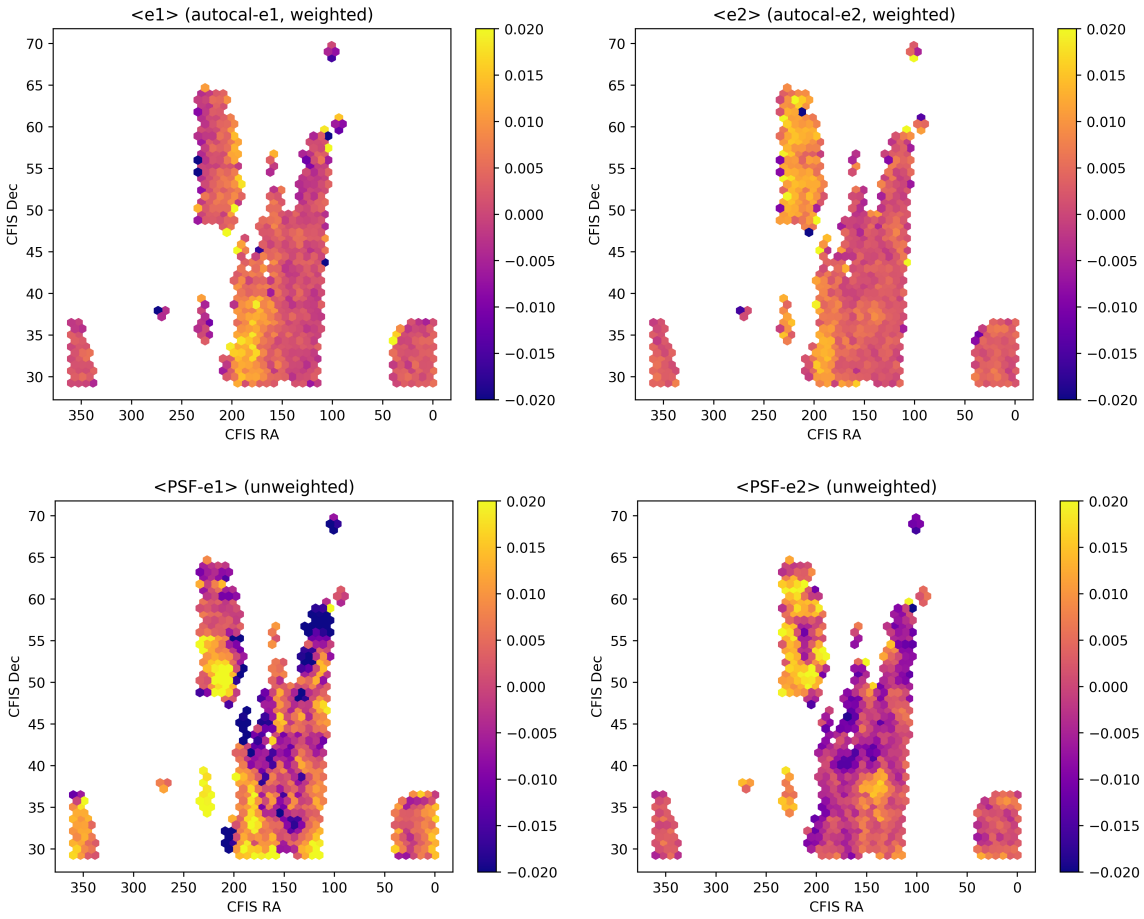

Figure 4.2: Top: The mean e_1 (left) and e_2 (right) components of CFIS galaxy shapes as a function of their position on the sky. Certain regions of the survey are more biased than others. Bottom: The mean e_1 (left) and e_2 (right) components of CFIS PSF shapes as a function of their position on the sky. The first shape component, e_1, shows strong rapid changes across the footprint, while e_2 shows changes that are less extreme.

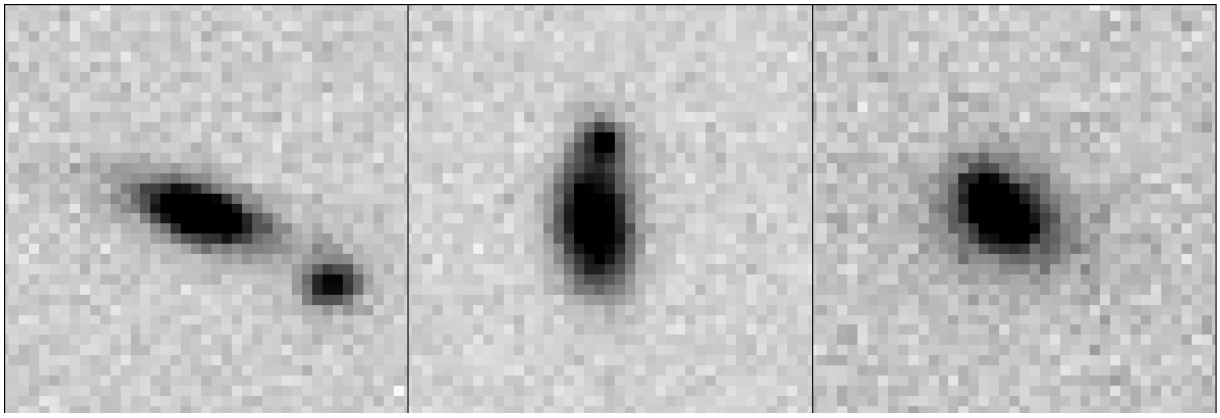

Figure 4.3: A series of sources with varying separations. As the separation decreases (left to right), the likelihood that the object detection algorithm detects two distinct objects decreases. If the pair is detected as a single object, it can induce bias as the shape measurement algorithm will measure the combined shape for the blend. The reported shape can therefore be a poor representation of the actual shapes of the individual objects.

Figure 4.4: Cutout from a simulation coadd showing two rotations of the same field. We create four such fields, each with an additional rotation of 45 degrees to minimize the effect of shape noise.

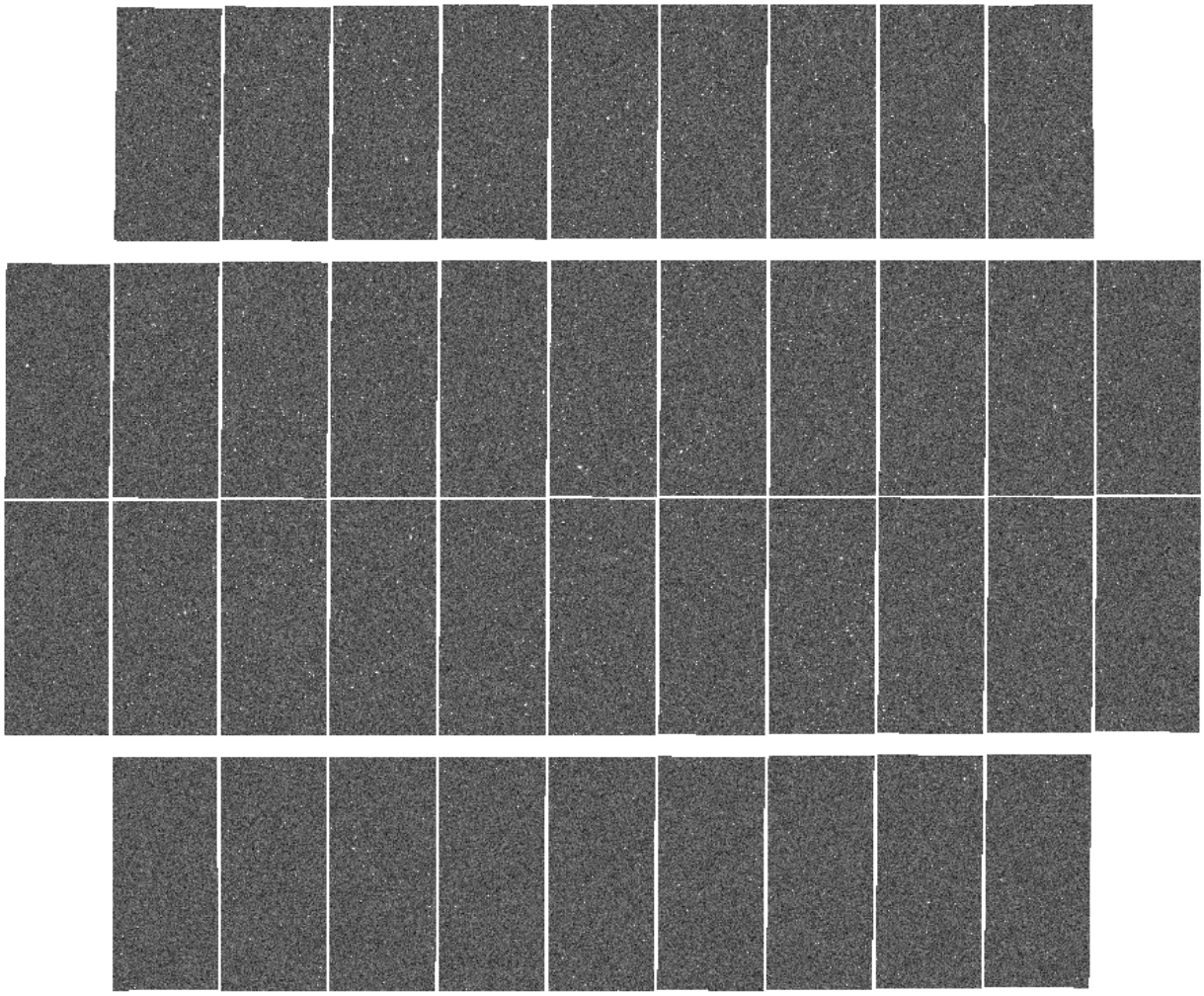

Figure 4.5: Simulation of a single CFIS exposure. All 40 chips in the Megacam array are simulated with the appropriate gaps.

added. These simulations are then processed by measuring shapes for each galaxy to determine how well the input shear is recovered.

Given the various sources of multiplicative and additive bias that can arise from correlations in galaxy properties, it is very important to make sure that the distribution of galaxy properties (magnitude, ellipticity, clustering, and size) is accurate. To that end, simulations are generated by utilizing the ACS-GC catalogue of Griffith et al. (2012) as an input catalogue for the simulation pipeline. The ACS-GC catalogue contains photometry and morphology for galaxies in the COSMOS field, and is sufficiently deep to simulate CFIS fields well beyond the CFIS detection limit. Because we are taking morphological parameters from ACS-GC, our simulations will naturally account for any correlations between magnitude, size, and ellipticity. Additionally, as positions are also taken from ACS-GC, realistic clustering of objects is included.

Multiple variations of each simulated observation are also created. The variations differ by galaxy shape orientation and applied shear. Four versions of each galaxy in the input catalogue are generated. The initial shape from the ACS-GC catalogue is used for the first version, while the remaining three have the galaxy rotated by 45, 90, and 135 degrees. This strategy is employed to deal with shape noise. With just a single observation, shape noise would dominate, but by producing the additional rotations, shape noise (before shear is applied) is eliminated as the mean ellipticity becomes 0.

In addition to the four rotations, we apply 8 shears to each of the rotated observations, resulting in 32 variations of each image. The 8 shears are selected following the strategy of Fenech Conti et al. (2017). All images contain a total applied shear of $|\gamma| = 0.02$. The shears used are

$$\gamma = [(0.0, 0.02), (0.0142, 0.0142), (0.02, 0.0), (0.0142, -0.0142),$$
$$(0.0, -0.02), (-0.0142, -0.0142), (-0.02, 0.0), (-0.0142, 0.0142)]$$

The COSMOS field lies near the equator while CFIS only surveys the sky north of 30 degrees declination. Because galaxy positions carry information on clustering, which can affect multiplicative bias by increasing the number of blended sources, it is important to retain the relative positions of objects on the sky. We therefore shift the positions of objects in the ACS-GC catalogue to a location that overlaps the CFIS survey. We shift the positions such that the catalogue overlaps 4 coadded CFIS tiles, which are 0.5 degrees by 0.5 degrees.

Given that the ACS-GC catalogue contains local stars which are not impacted by weak gravitational lensing, we must first carefully remove them from the catalogue. We therefore follow the prescription described in Griffith et al. (2012), whereby we apply a cut and remove all sources with with a magnitude $\mu \leq 18$ or (magnitude $\mu \geq 18$ and effective radius $r_e \leq 0.03''$).

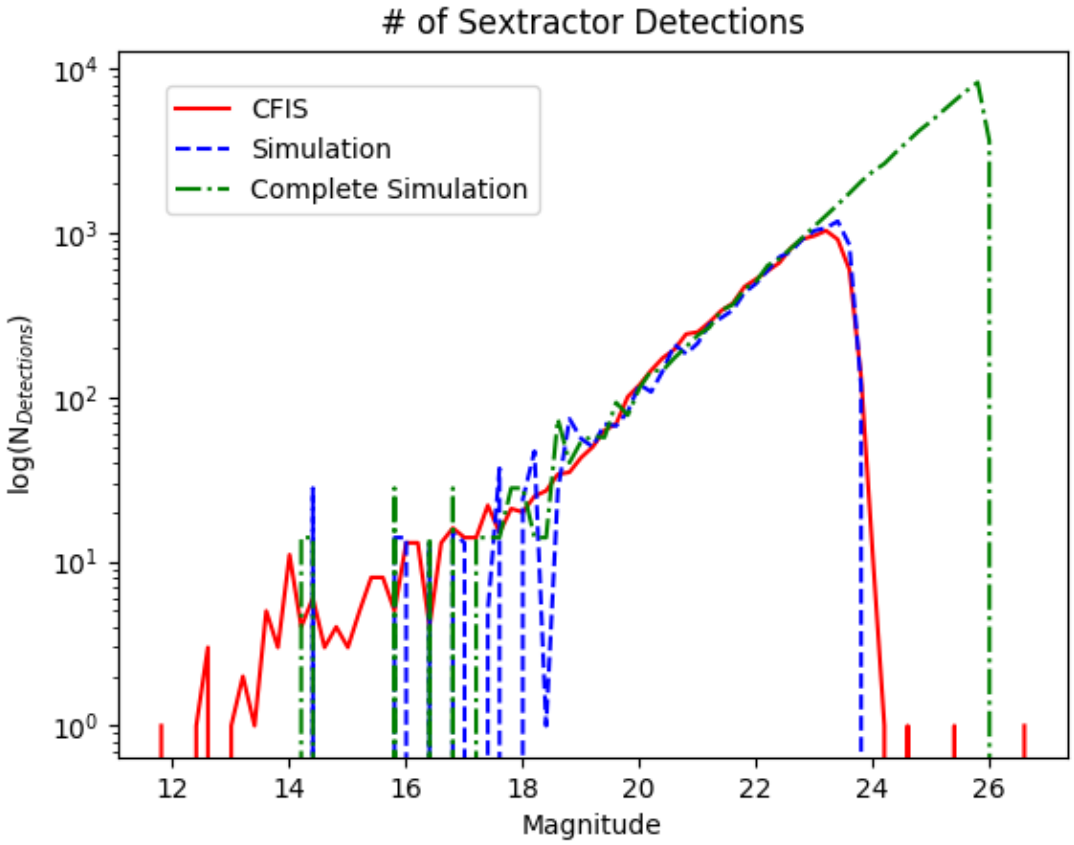

Figure 4.6: Histograms of the number of objects per square degree in the input catalogue as a function of their assigned r-band magnitude. The galaxies come directly from the ACS-GC catalogue, while the stars are from a simulated Besançon model. The simulated input catalogue (green) extends out to $r = 26$, which is beyond the detection threshold for CFIS. The blue line shows the number of objects detected from a Sextractor run on the simulated image, while the red line shows the number of objects detected from a Sextractor run on a real CFIS image.

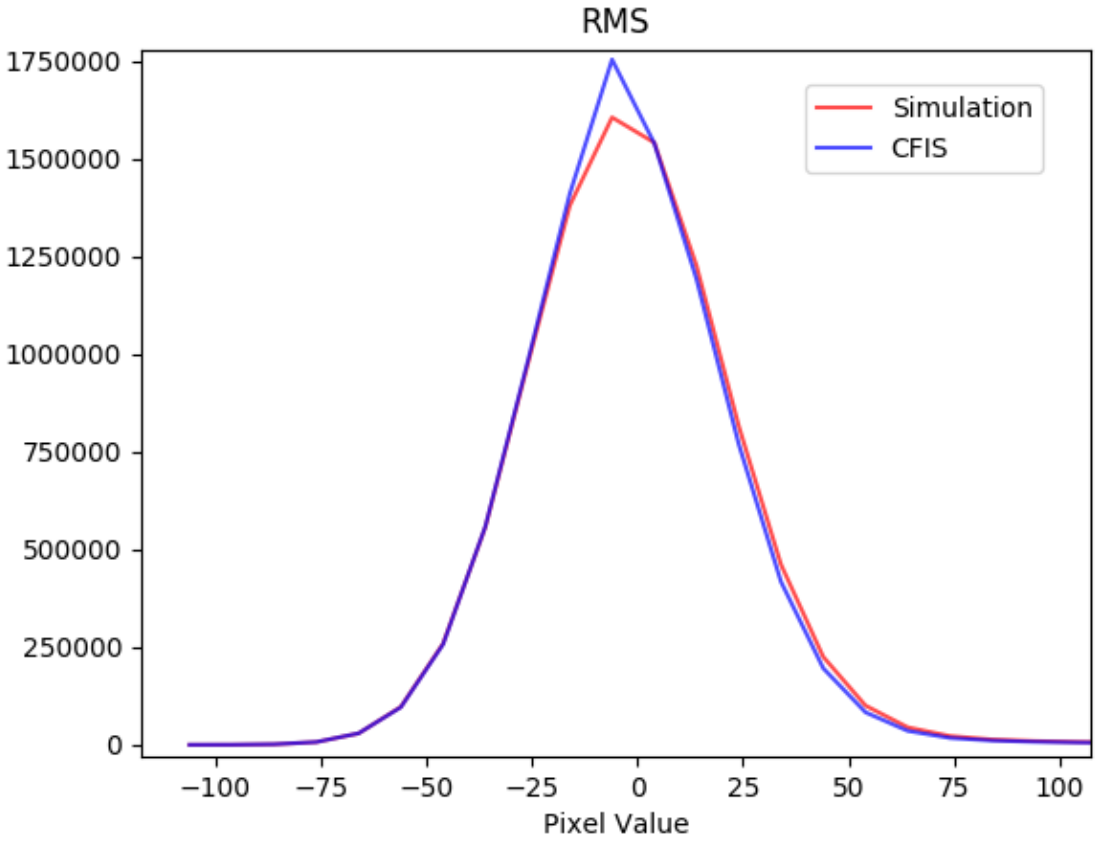

Figure 4.7: The root mean squared of pixel values in a simulated CFIS image (red) and an actual CFIS image (blue). The width of the two curves is a measurement of the level of noise present in the two images.

We then generate a simulated distribution of stars to be added back in. The stellar population is drawn from the Besançon model (Czekaj et al., 2014). We simulate the stellar catalogue out to an r-band magnitude of 26, almost two magnitudes past the nominal detection threshold of 24.1 (Figure 4.6).

GalSim (Rowe et al., 2015) is then used to convert the input catalogue into a simulated observation. Size, ellipticity, Sérsic index, and r-band magnitude are taken from each object in the ACS-GC catalogue and converted into a single Sérsic profile. The surface brightness profile is then copied 32 times, with each copy being rotated by an additional 45 degrees (Figure 4.4) and with one of eight shears applied. This provides us with 32 versions of the same galaxy with different position angles and shears that combine to minimize the effects of shape noise. Because the galaxy positions are also drawn from the ACS-GC catalogue, the 32 variations of each galaxy are not rendered to the same observation. Rather, we opt to generate 32 exposures of the same field, each with a different combination of rotation and shear applied.

The galaxy is convolved with a PSF, modelled as a Moffat profile with a FWHM of 0.6 arcseconds, consistent with CFIS seeing conditions. For the current analysis, PSFs are circular, though future iterations of the simulations will feature more realistic anisotropic PSFs. The galaxies and stars are then added to the simulated CCDs. A Gaussian noise field is then added to the 32 variations of the images to match the noise properties of CFIS data and to ensure that the detection number count distribution rolls over at the same r-band magnitude.

Individual CFIS exposures are simulated. As such, the MegaCam array of forty 2048 x 4612 e2v CCDs, with appropriate chip gaps, is modelled (Boulade et al., 2003) (Figure 4.5). We create the simulations with the correct pixel scale of 0.187 arcseconds per pixel creating a 1 square degree field per exposure. The world coordinate system (WCS) from each MegaCam observation is also applied to the simulated image. The WCS contains the geometric transformations which translate a location on the CCD pixel grid to a location on the sky and vice-versa. The WCS also contains the distortions and shears that arise from the optical assembly of the instrument itself.

We incorporate the CFIS observing strategy into the simulations by duplicating the dithering pattern of the real CFIS observations. Given the survey's unique observing strategy of dithering each exposure by about one third of the camera's field of view, we want to ensure that any biases associated with this novel observing pattern are captured by the simulations. Because we are duplicating the survey so closely, we can process the simulated CFIS data using the same pipelines that are used to process the real CFIS data with no modifications.

Several individual exposures go into the production of a single coadd, and because the dithers are so large, there are portions of these single exposures that lie outside the shifted ACS-GC catalogue. In some cases, there are entire chips that do not contain any ACS-GC objects. We do simulate the stellar catalogue in these regions, as stellar sources are required in each chip by

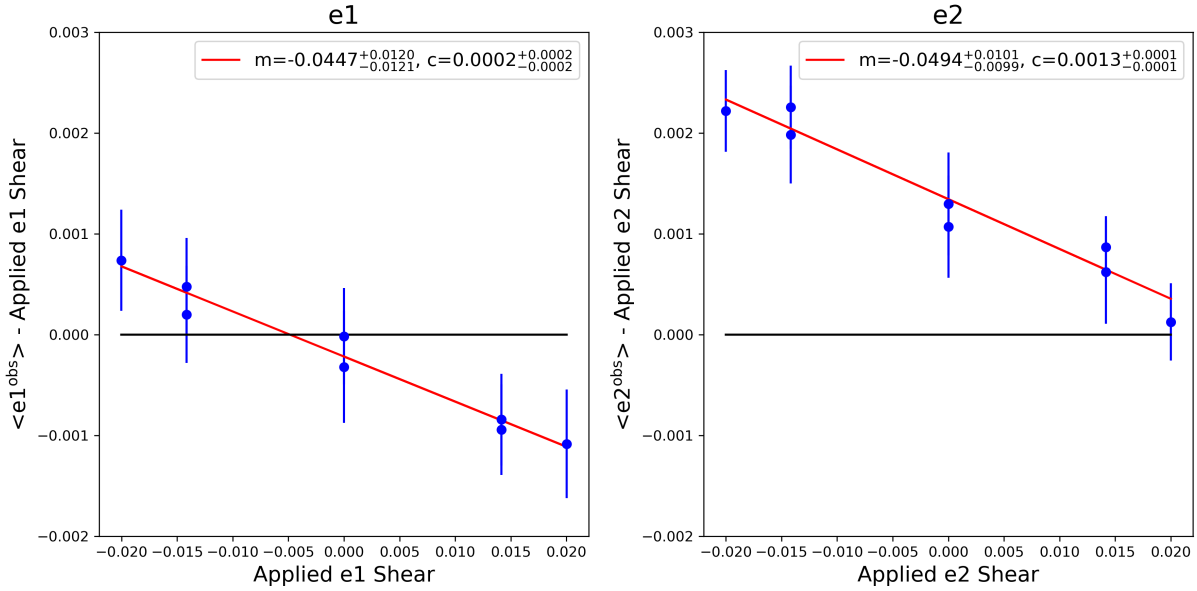

Figure 4.8: Bias present in the e_1 and e_2 components of the measured shapes. We fit a linear model (red) to measure the multiplicative (m) and additive (c) biases.

the shape measurement algorithms. We note that this lack of galaxies in areas of the individual exposures is not an issue in practice, as even the real CFIS data is masked and therefore also contains large regions with no sources, particularly around large, bright foreground galaxies like M101. Individual exposures are combined using the same THELI pipeline (Erben et al., 2005) used to stack the CFIS exposures.

4.4 Results

After the shape catalogues are produced, we estimate both the multiplicative and additive bias by plotting the known applied shear to the measured e_1 and e_2 shapes. In the absence of any such biases, the mean recovered shapes should be consistent with the applied shears. We plot the difference between the observed shapes and the applied shear in Figure 4.8.

The uncertainties are derived from bootstrap sampling. We match the shape catalogues for all 4 rotations and order them. This guarantees that when we select subsamples from the catalogues, we get all four rotations of the same galaxy each time. We bootstrap sample the population 1,000 times and calculate the standard deviation of the values which are then used as the uncertainties.

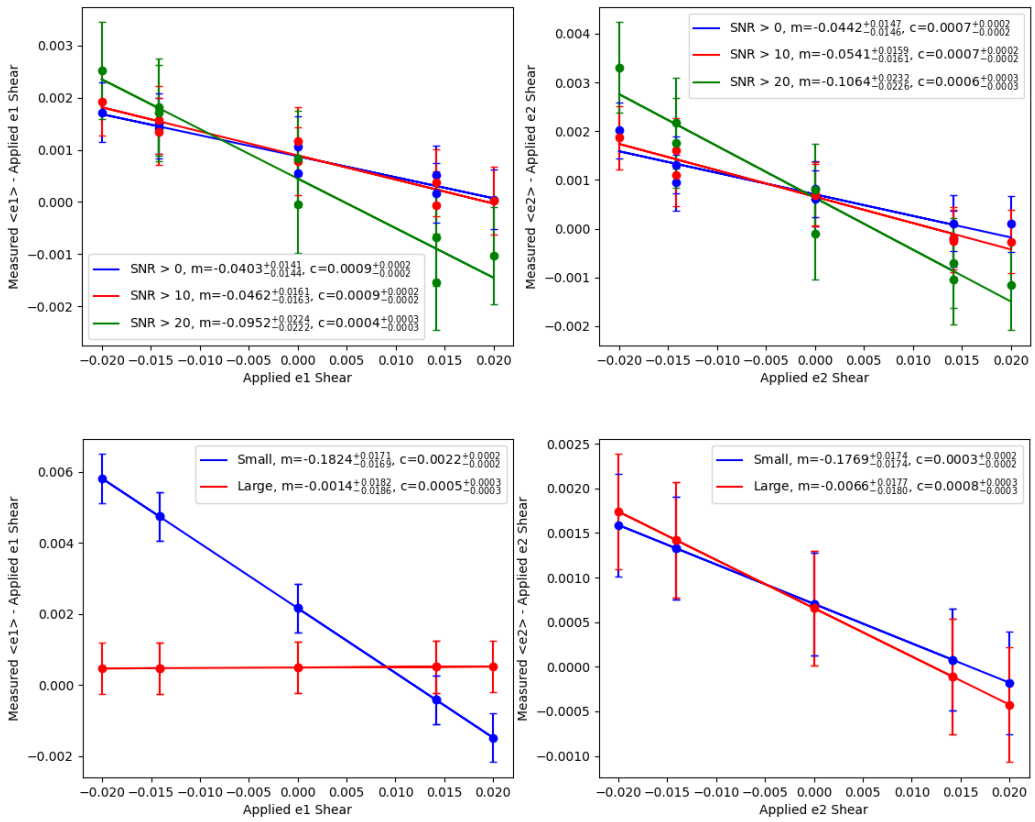

Figure 4.9: Top: Bias present in the e_1 and e_2 components of the measured shapes after filtering by the signal to noise ratio. Bottom: Bias present in the e_1 and e_2 components of the measured shapes after filtering by size. The small sample is from sources where FLUX_RADIUS $\leq$ 3.0. The large sample contains everything else.

We then perform a linear fit on the data to measure the multiplicative and additive biases present in the shape measurement process. These values, the slope and intercept of the linear model, correspond to the m and c of Equation 4.1.

This results in multiplicative biases for the e_1 and e_2 components that are consistent with one another, but there is a significantly larger additive bias for the e_2 component. This additive bias on the e_2 component was also present in the CFHTLenS survey, which was also carried out by the same observatory (Heymans et al., 2012) and utilized the same shape measurement algorithm.

4.5 Discussion and Conclusions

Weak lensing surveys that are designed to measure cosmic shear, the lensing due to the large scale structure, require precise shape measurements for the background sources. Generally, the multiplicative bias must be known to better than one percent. To achieve this goal for the CFIS survey, we have described here a preliminary set of lensing simulations designed to match the CFIS survey specifications and observing qualities.

These simulations are then tested against a weak lensing pipeline that is using the *lens*fit shape measurement algorithm at its core (Miller et al., 2007a). We find that, on its own, the weak lensing pipeline has a multiplicative bias of ∼4.7% and an additive bias of ∼0.08%. This is less than the previous weak lensing survey carried out by the same instruments, CFHTLenS, which found a multiplicative bias of ∼6% (Heymans et al., 2012). There have been some improvements to the *lens*fit shape measurement algorithm since then, and for this analysis, we make use of the reported AUTOCAL-E1 and AUTOCAL-E2 measurements which incorporate some self-calibration.

Despite the modest improvement, the multiplicative bias is still significantly higher than the desired target of better than one percent, which demonstrates the need for bias calibration. We additionally examine the additive bias as a function of source magnitude and size by examining the weak lensing shape catalogue. We find that, overall, additive bias increases as sources become fainter. For size, the situation is not so simple. The e_1 component of the shapes shows a positive additive bias for small sources and a negative additive bias for large objects, while the e_2 component has a positive additive bias regardless of size.

An additional complication comes from the fact that, while small, the e_2 component of the additive bias for the survey is significantly larger than for the e_1 component. While this discrepancy is not new (it was measured in the CFHTLenS survey (Heymans et al., 2012)), its source remains undetermined.

When comparing the additive bias measured from the simulations to the additive bias measured from the data itself, we also find a discrepancy. From the simulations, $c_1 = 0.0002 \pm 0.0002$

and $c_2 = 0.0013 \pm 0.0001$. When taking the weighted means of the shape components from the *lens*fit catalogue, however, we recover $c_1 = 0.003772$ and $c_2 = 0.004989$. It should be noted that these simulations are still under development and this result is not entirely unexpected. In the simulations presented here, the PSF is isotropic, while real data shows complex PSF leakage with galaxy shapes. As the simulations continue to improve, we expect the estimates of the biases to become more realistic as well. Additionally, since this work was performed, there have been improvements to the *lens*fit pipeline used to measure shapes. Notably, the astrometry has been improved, which has dropped the mean e_1 and e_2 values from what is reported here.

The simulations used for CFIS have the advantage of including the world coordinate systems (WCS) from actual CFIS observations. While this means that any bias induced by the effects of the WCS on real observations is included in the simulations, it means that we can additionally modify the WCS as a means of testing it as a potential source of these differences between the two components of the additive bias.

In addition to understanding the sources of these biases, future work will expand on increasing the realism of the simulations. The PSF in the current suite of simulations is constant across all observations. Future implementations of these simulations will include more accurate PSF models. Incorporating more complex, anisotropic PSF models, we will be able to test for PSF leakage, which appears to be an issue for the survey considering the correlation in galaxy and PSF shapes present in Figure 4.2. An additional benefit of introducing multiple PSFs is that the number of simulated observations will also increase, allowing for more precise measurements of the multiplicative bias. Understanding and calibrating these sources of bias will become increasingly important in the future, as upcoming weak lensing surveys (LSST[2], Euclid[3], Roman[4]) require even higher levels of precision.

[2]http://lsst.org
[3]https://www.euclid-ec.org/
[4]https://roman.gsfc.nasa.gov/

Chapter 5

Conclusion

In this thesis, various topics relating to weak lensing were explored. Chapter 2 examined the redshift distribution of sources in the CFIS-*r* survey before using that distribution to measure the cluster mass-richness relation. Cluster number counts are an important cosmological probe, as they can be used to reconstruct the cluster mass function which depends on the cosmological parameters σ_8 and Ω_m. To do this, cluster masses, in addition to the counts, must be measured. The cluster mass-richness relation provides a simple conversion between the observable richness and the cluster's mass. We compare the mass-richness relation derived from CFIS-*r* using the redMaPPer cluster catalogue (Rykoff et al., 2014) and find good agreement with results from previous surveys. Additionally, we analyzed populations of star-forming and quiescent group centrals using the group catalogue of Tinker (2020a). The centrals were binned by their estimated stellar mass, then halo masses were measured via weak lensing. We confirm evidence of a halo mass bimodality between these populations for a fixed stellar mass.

Chapter 3 examined the topic of satellites in galaxy groups. Again, we used an early, internal release of the CFIS-*r* shape catalogue to measure the subhalo mass for a typical group satellite. We attempted to detect evidence for the tidal stripping of satellites in these environments. Tidal stripping is thought to play a role in the quenching of star formation in satellite galaxies in dense environments. We attempted to detect tidal stripping by binning satellites from the Tinker (2020a) group catalogue by their projected separation from the group centre. We found, however, the resulting $\Delta\Sigma$ signal from these bins was too weak to significantly detect this effect, regardless of the various efforts made to enhance it. The CFIS-*r* survey is still underway and will eventually produce a catalogue that covers ~5,000 square degrees. The extra coverage will increase the sample size of galaxy groups, so there remains a potential to detect this effect in the near future.

Chapter 4 covered the work done to calibrate the CFIS-*r* survey using simulations of weak

lensing observations. The simulations were created to reproduce CFIS data as closely as possible. Clustering and morphological information for the simulated galaxies was drawn from the COSMOS catalogue (Griffith et al., 2012). The objects were then sheared and convolved with PSFs before being added to observations that followed the observing strategy of CFIS. An initial analysis of the first set of simulations shows multiplicative and additive biases that depend on properties such as size and magnitude, consistent with findings from efforts to calibrate other surveys.

Appendix A discusses a public, web-based tool for weak lensing analysis. Users can provide a list of lenses, and the tool will use one of two publicly available weak lensing catalogues to generate a $\Delta\Sigma$ signal which is then emailed back to the user. The architecture of the tool is discussed, and a comparison between the $\Delta\Sigma$ signal generated from the site is compared with a previously published signal.

There remains much work to be done on the CFIS survey. Data collection is ongoing, but will eventually result in a ~4,800 square degree catalogue of high quality, deep r-band photometry. This data set will then need to be processed and shapes for over a hundred million galaxies will need to be measured. These shapes will then need to be calibrated by a robust set of simulations. By that point, the simulation framework will be improved to include a set of realistic PSFs that closely match the real CFIS data. These simulations will then be used to calibrate two independent shape measurement pipelines to ensure that the shapes produced are accurate to within one part in one thousand. This will enable the CFIS survey to analyze the weak lensing induced by the large scale structure (cosmic shear) which will help untangle some of the current cosmological questions surrounding the apparent acceleration in the expansion of the universe.

Beyond CFIS, the future of weak lensing looks very promising. Within the next decade, three major surveys that will produce an enormous amount of high quality data will begin. LSST will scan the southern night sky once every few nights, producing ~20,000 square degrees of galaxy shapes. Euclid and Roman will launch and observe the sky in the visible and IR bands from their location orbiting the L2 Sun-Earth Lagrangian point, removing the blurring effect of the atmosphere, a major thorn in the side of traditional ground based weak lensing surveys. These surveys will guarantee that weak gravitational lensing will continue to play an important role in exploring the many questions surrounding the dark universe for decades to come.

References

Aihara H., et al., 2011, Astrophysical Journal, Supplement, 193, 29

Allen S. W., Evrard A. E., Mantz A. B., 2011, Annual Review of Astronomy and Astrophysics, 49, 409

Bacon D. J., Refregier A. R., Ellis R. S., 2000, Mon. Not. Roy. Astron. Soc., 318, 625

Bahcall N. A., Cen R., 1993, Astrophysical Journal, Letters, 407, L49

Berlind A. A., et al., 2006, Astrophysical Journal, Supplement, 167, 1

Bertin E., Arnouts S., 1996, , 117, 393

Blandford R., Narayan R., 1986, Astrophysical Journal, 310, 568

Blanton M. R., et al., 2017, Astronomical Journal, 154, 28

Bleem L. E., et al., 2015, Astrophysical Journal, Supplement, 216, 27

Böhringer H., et al., 2000, Astrophysical Journal, Supplement, 129, 435

Boruah S. S., Hudson M. J., Lavaux G., 2020, Mon. Not. Roy. Astron. Soc., 498, 2703

Boulade O., et al., 2003, in Iye M., Moorwood A. F. M., eds, Society of Photo-Optical Instrumentation Engineers (SPIE) Conference Series Vol. 4841, Instrument Design and Performance for Optical/Infrared Ground-based Telescopes. pp 72–81, doi:10.1117/12.459890

Brainerd T. G., Blandford R. D., Smail I., 1996, Astrophysical Journal, 466, 623

Bridle S. L., Kneib J. P., Bardeau S., Gull S. F., 2002, in Natarajan P., ed., The Shapes of Galaxies and their Dark Halos. pp 38–46, doi:10.1142/9789812778017_0006

Bridle S., et al., 2010, Mon. Not. Roy. Astron. Soc., 405, 2044

Cardone V. F., Martinelli M., Calabrese E., Galli S., Huang Z., Maoli R., Melchiorri A., Scaramella R., 2014, Mon. Not. Roy. Astron. Soc., 439, 202

Carlberg R. G., Morris S. L., Yee H. K. C., Ellingson E., 1997, Astrophysical Journal, Letters, 479, L19

Chandrasekhar S., 1943, Astrophysical Journal, 97, 255

Clowe D., Gonzalez A., Markevitch M., 2004, The Astrophysical Journal, 604, 596–603

Colpi M., Mayer L., Governato F., 1999, Astrophysical Journal, 525, 720

Contini E., De Lucia G., Borgani S., 2012, Mon. Not. Roy. Astron. Soc., 420, 2978

Costanzi M., et al., 2021, Physical Review D, 103

Cui W., Davé R., Peacock J. A., Anglés-Alcázar D., Yang X., 2021, Nature Astronomy, 5, 1069

Czekaj M. A., Robin A. C., Figueras F., Luri X., Haywood M., 2014, Astronomy and Astrophysics, 564, A102

DES Collaboration et al., 2021, arXiv e-prints, p. arXiv:2105.13549

DESI Collaboration et al., 2016, The DESI Experiment Part I: Science,Targeting, and Survey Design (arXiv:1611.00036)

Drakos N. E., Taylor J. E., Benson A. J., 2017, Mon. Not. Roy. Astron. Soc., 468, 2345

Dressler A., 1980, Astrophysical Journal, 236, 351

Duffy A. R., Schaye J., Kay S. T., Dalla Vecchia C., 2008, Mon. Not. Roy. Astron. Soc., 390, L64

Durret F., Chiche S., Lobo C., Jauzac M., 2021a, Astronomy and Astrophysics, 648, A63

Durret F., Chiche S., Lobo C., Jauzac M., 2021b, Astronomy and Astrophysics, 648, A63

Dyson F. W., Eddington A. S., Davidson C., 1920, Philosophical Transactions of the Royal Society of London Series A, 220, 291

Efstathiou G., Sutherland W. J., Maddox S. J., 1990, Nature, 348, 705

Einstein A., 1916, Annalen der Physik, 354, 769

Eke V. R., et al., 2004, Mon. Not. Roy. Astron. Soc., 348, 866

Epps S. D., Hudson M. J., 2017, Monthly Notices of the Royal Astronomical Society, 468, 2605–2613

Erben T., et al., 2005, Astronomische Nachrichten, 326, 432

Fang Y., Clampitt J., Dalal N., Jain B., Rozo E., Moustakas J., Rykoff E., 2016, Mon. Not. Roy. Astron. Soc., 463, 1907

Fenech Conti I., Herbonnet R., Hoekstra H., Merten J., Miller L., Viola M., 2017, Mon. Not. Roy. Astron. Soc., 467, 1627

Ford J., VanderPlas J., 2016, Astronomical Journal, 152, 228

Ford J., Hildebrandt H., Van Waerbeke L., Erben T., Laigle C., Milkeraitis M., Morrison C. B., 2014, Mon. Not. Roy. Astron. Soc., 439, 3755

Foreman-Mackey D., Hogg D. W., Lang D., Goodman J., 2013, Publications of ASP, 125, 306

Fort B., Prieur J. L., Mathez G., Mellier Y., Soucail G., 1988, Astronomy and Astrophysics, 200, L17

Frenk C. S., White S. D. M., Davis M., Efstathiou G., 1988, Astrophysical Journal, 327, 507

Gamow G., Teller E., 1939, Physical Review, 55, 654

Gao L., White S. D. M., Jenkins A., Stoehr F., Springel V., 2004, Mon. Not. Roy. Astron. Soc., 355, 819

Gillis B. R., et al., 2013, Mon. Not. Roy. Astron. Soc., 431, 1439

Griffith R. L., et al., 2012, Astrophysical Journal, Supplement, 200, 9

Gunn J. E., Gott J. Richard I., 1972a, Astrophysical Journal, 176, 1

Gunn J. E., Gott J. Richard I., 1972b, Astrophysical Journal, 176, 1

Guth A. H., 1981, Physical Review D, 23, 347

Hanany S., et al., 2000, Astrophysical Journal, Letters, 545, L5

Heymans C., et al., 2006a, Mon. Not. Roy. Astron. Soc., 368, 1323

Heymans C., et al., 2006b, Mon. Not. Roy. Astron. Soc., 368, 1323

Heymans C., et al., 2012, Mon. Not. Roy. Astron. Soc., 427, 146

Hildebrandt H., et al., 2017, Mon. Not. Roy. Astron. Soc., 465, 1454

Hodgson T., Bartalucci I., Johnston-Hollitt M., McKinley B., Vazza F., Wittor D., 2021, Astrophysical Journal, 909, 198

Hoekstra H., et al., 2001, Astrophysical Journal, Letters, 548, L5

Hoekstra H., et al., 2006, Astrophysical Journal, 647, 116

Hoekstra H., Herbonnet R., Muzzin A., Babul A., Mahdavi A., Viola M., Cacciato M., 2015, Mon. Not. Roy. Astron. Soc., 449, 685

Hoekstra H., Viola M., Herbonnet R., 2017, Mon. Not. Roy. Astron. Soc., 468, 3295

Hubble E. P., 1926, Astrophysical Journal, 64, 321

Hubble E., 1929, Proceedings of the National Academy of Science, 15, 168

Huchra J. P., Geller M. J., 1982, Astrophysical Journal, 257, 423

Hudson M. J., Gwyn S. D. J., Dahle H., Kaiser N., 1998, Astrophysical Journal, 503, 531

Hudson M. J., et al., 2015, Mon. Not. Roy. Astron. Soc., 447, 298

Huff E., Mandelbaum R., 2017, arXiv e-prints, p. arXiv:1702.02600

Ivezić Ž., et al., 2019, Astrophysical Journal, 873, 111

Joshi G. D., Parker L. C., Wadsley J., Keller B. W., 2019, Mon. Not. Roy. Astron. Soc., 483, 235

Kaiser N., Squires G., 1993, Astrophysical Journal, 404, 441

Kaiser N., Squires G., Broadhurst T., 1995, Astrophysical Journal, 449, 460

Kaiser N., Wilson G., Luppino G. A., 2000, arXiv e-prints, pp astro–ph/0003338

Kannawadi A., et al., 2019, Astronomy and Astrophysics, 624, A92

Kitching T., et al., 2010, arXiv e-prints, p. arXiv:1009.0779

Kuijken K., 1999, Astronomy and Astrophysics, 352, 355

Kuijken K., et al., 2015, Mon. Not. Roy. Astron. Soc., 454, 3500

Laureijs R., et al., 2012, in Clampin M. C., Fazio G. G., MacEwen H. A., Oschmann Jacobus M. J., eds, Society of Photo-Optical Instrumentation Engineers (SPIE) Conference Series Vol. 8442, Space Telescopes and Instrumentation 2012: Optical, Infrared, and Millimeter Wave. p. 84420T, doi:10.1117/12.926496

Le Fèvre O., et al., 2013, Astronomy and Astrophysics, 559, A14

Li R., et al., 2014, Mon. Not. Roy. Astron. Soc., 438, 2864

Lifshitz E. M., 1946, J. Phys. (Moscow), 10

Lima M., Cunha C. E., Oyaizu H., Frieman J., Lin H., Sheldon E. S., 2008, Mon. Not. Roy. Astron. Soc., 390, 118

Luo W., et al., 2018, Astrophysical Journal, 862, 4

Mandelbaum R., Seljak U., Kauffmann G., Hirata C. M., Brinkmann J., 2006, Mon. Not. Roy. Astron. Soc., 368, 715

Mandelbaum R., et al., 2014, Astrophysical Journal, Supplement, 212, 5

Mandelbaum R., et al., 2015, Mon. Not. Roy. Astron. Soc., 450, 2963

Mandelbaum R., Wang W., Zu Y., White S., Henriques B., More S., 2016, Mon. Not. Roy. Astron. Soc., 457, 3200

Massey R., et al., 2007, Mon. Not. Roy. Astron. Soc., 376, 13

McClintock T., et al., 2019, Mon. Not. Roy. Astron. Soc., 482, 1352

Miller L., Kitching T. D., Heymans C., Heavens A. F., van Waerbeke L., 2007a, Mon. Not. Roy. Astron. Soc., 382, 315

Miller L., Kitching T. D., Heymans C., Heavens A. F., Van Waerbeke L., 2007b, Monthly Notices of the Royal Astronomical Society, 382, 315–324

Miller L., et al., 2013, Mon. Not. Roy. Astron. Soc., 429, 2858

Moore B., Katz N., Lake G., Dressler A., Oemler A., 1996a, Nature, 379, 613

Moore B., Katz N., Lake G., Dressler A., Oemler A., 1996b, Nature, 379, 613

Moore B., Lake G., Quinn T., Stadel J., 1999, Mon. Not. Roy. Astron. Soc., 304, 465

Natarajan P., Kneib J.-P., Smail I., Ellis R. S., 1998, Astrophysical Journal, 499, 600

Natarajan P., Kneib J.-P., Smail I., 2002, Astrophysical Journal, Letters, 580, L11

Natarajan P., Kneib J.-P., Smail I., Treu T., Ellis R., Moran S., Limousin M., Czoske O., 2009, Astrophysical Journal, 693, 970

Newman J. A., et al., 2013, Astrophysical Journal, Supplement, 208, 5

Oemler Augustus J., 1974, Astrophysical Journal, 194, 1

Ostriker J. P., Steinhardt P. J., 1995, Nature, 377, 600

Parker L. C., Hudson M. J., Carlberg R. G., Hoekstra H., 2005, Astrophysical Journal, 634, 806

Perlmutter S., et al., 1999, Astrophysical Journal, 517, 565

Planck Collaboration et al., 2014, Astronomy and Astrophysics, 571, A20

Planck Collaboration et al., 2020, Astronomy and Astrophysics, 641, A6

Press W. H., Schechter P., 1974, Astrophysical Journal, 187, 425

Rafelski M., et al., 2015, Astronomical Journal, 150, 31

Read J. I., Wilkinson M. I., Evans N. W., Gilmore G., Kleyna J. T., 2006a, Monthly Notices of the Royal Astronomical Society, 366, 429

Read J. I., Wilkinson M. I., Evans N. W., Gilmore G., Kleyna J. T., 2006b, Mon. Not. Roy. Astron. Soc., 366, 429

Reid B. A., et al., 2010, Monthly Notices of the Royal Astronomical Society

Richstone D. O., 1976, Astrophysical Journal, 204, 642

Riess A. G., et al., 1998, Astronomical Journal, 116, 1009

Rix H.-W., et al., 2004, Astrophysical Journal, Supplement, 152, 163

Roberts M. S., Rots A. H., 1973, Astronomy and Astrophysics, 26, 483

Roberts I. D., et al., 2021a, arXiv e-prints, p. arXiv:2104.05383

Roberts I. D., van Weeren R. J., McGee S. L., Botteon A., Ignesti A., Rottgering H. J. A., 2021b, Astronomy and Astrophysics, 652, A153

Rowe B. T. P., et al., 2015, Astronomy and Computing, 10, 121

Rubin V. C., Ford W. K. J., Thonnard N., 1978, Astrophysical Journal, Letters, 225, L107

Rykoff E. S., et al., 2014, Astrophysical Journal, 785, 104

Sevilla-Noarbe I., et al., 2021, Astrophysical Journal, Supplement, 254, 24

Sheldon E. S., Huff E. M., 2017, Astrophysical Journal, 841, 24

Sheldon E. S., et al., 2004, Astronomical Journal, 127, 2544

Sifón C., et al., 2015, Mon. Not. Roy. Astron. Soc., 454, 3938

Simet M., McClintock T., Mandelbaum R., Rozo E., Rykoff E., Sheldon E., Wechsler R. H., 2017, Mon. Not. Roy. Astron. Soc., 466, 3103

Singh S., Mandelbaum R., Seljak U., Slosar A., Vazquez Gonzalez J., 2017, Mon. Not. Roy. Astron. Soc., 471, 3827

Smith R. J., et al., 2010, Mon. Not. Roy. Astron. Soc., 408, 1417

Soucail G., Fort B., Mellier Y., Picat J. P., 1987, Astronomy and Astrophysics, 172, L14

Spergel D., et al., 2013, arXiv e-prints, p. arXiv:1305.5422

Sunyaev R. A., Zeldovich Y. B., 1972, Comments on Astrophysics and Space Physics, 4, 173

Tinker J. L., 2020a, arXiv e-prints, p. arXiv:2007.12200

Tinker J. L., 2020b, arXiv e-prints, p. arXiv:2010.02946

Tinker J., Kravtsov A. V., Klypin A., Abazajian K., Warren M., Yepes G., Gottlöber S., Holz D. E., 2008, Astrophysical Journal, 688, 709

Tyson J. A., Valdes F., Jarvis J. F., Mills A. P. J., 1984, Astrophysical Journal, Letters, 281, L59

Tyson J. A., Valdes F., Wenk R. A., 1990, Astrophysical Journal, Letters, 349, L1

Van Waerbeke L., et al., 2000, Astronomy and Astrophysics, 358, 30

Vogelsberger M., Marinacci F., Torrey P., Puchwein E., 2019, Cosmological Simulations of Galaxy Formation (arXiv:1909.07976)

Walsh D., Carswell R. F., Weymann R. J., 1979, Nature, 279, 381

Wittman D. M., Tyson J. A., Kirkman D., Dell'Antonio I., Bernstein G., 2000, Nature, 405, 143

Yang X., Mo H. J., van den Bosch F. C., Pasquali A., Li C., Barden M., 2007, Astrophysical Journal, 671, 153

Zwicky F., 1933, Helvetica Physica Acta, 6, 110

de Bernardis P., et al., 2000, Nature, 404, 955

de Jong J. T. A., et al., 2013, The Messenger, 154, 44

van den Bosch F. C., Ogiya G., Hahn O., Burkert A., 2018, Mon. Not. Roy. Astron. Soc., 474, 3043

van den Bosch F. C., Jiang F., Campbell D., Behroozi P., 2015, Monthly Notices of the Royal Astronomical Society, 455, 158

von Hoerner S., 1957a, Astrophysical Journal, 125, 451

von Hoerner S., 1957b, Astrophysical Journal, 125, 451

von Soldner J. G., 1804, Berliner Astronomisches Jahrbuch, pp 161–172

APPENDICES

Appendix A

Weak Lensing for the Masses

In this appendix, we introduce a free, public, web-based tool ("Weak Lensing for the Masses") for efficiently performing weak lensing analyses without sacrificing the constraining power of the resulting $\Delta\Sigma$ profiles. In A.1, we describe the way that traditional lensing algorithms find lens-source pairs. Section A.2 describes the approach utilized by the web-based weak lensing analysis tool outlined in Section A.3. In Section A.4, a $\Delta\Sigma$ signal generated by the pipeline outlined in this chapter is compared to that of previously published results.

A.1 Traditional Lensing Analysis

To measure a weak lensing signal, one must first find the background sources around the selected lenses and measure their projected separation in physical units. Because only the background sources that lie near the lens on the sky are distorted, the sources that lie at a large angular separations from the lens are not important. It is therefore more computationally efficient to simply ignore any sources with a separation that is too large. But to know whether or not a source is near or far from the lens, the separation must be computed.

Calculating the projected separation between a lens and every source in the survey is far too expensive an approach to use with even the current generation of weak lensing surveys. One common method of avoiding this scenario while still finding most of the lens-source pairs is to break the footprint of the survey into a set of rectangular regions. You then determine the region your lens lies in and calculate the lens-source pair separations for all of the sources in the same region.

While this is more computationally efficient than calculating separations for all sources in the catalogue, there is a tradeoff between efficiency and the ability to utilize every lens-source pair that exists in the complete survey. If your lens happens to fall near the edge of a region, potentially half of the sources that are near the lens will lie in a different region and will therefore be excluded from the lensing analysis. If the lens lies in a corner of the region, up to 75% of the sources are missed. By not considering all lens-source pairs, you lose constraining power as the error bars depend on the number of pairs.

In principle, one could correct for this by making the regions larger, but then the number of separations that must be calculated increases, as does the number of lens-source pairs that are too distant to be physically interesting for galaxy-galaxy lensing. This is computationally wasteful. Another solution could be to consider the regions surrounding the one the lens resides in for cases where the lens happens to fall near an edge. However, this runs into the same issue as increasing the region size, as processing time will be wasted computing separations for lens-source pairs that have a large angular separation. In the following section, we will introduce an algorithm that doesn't sacrifice usable lens-source pairs, but that also doesn't waste processing time calculating separations for lens-source pairs that are too distant to be useful. This is the lens-source algorithm that powers the "Weak Lensing for the Masses" pipeline.

A.2 Processing

Here, we will describe an algorithm for efficiently finding every physically interesting lens-source pair in a catalogue without calculating all separations. To accomplish this, we utilize the HealPix software[1] which breaks the sky into regions it calls pixels. This is similar in concept to breaking a large survey into rectangular regions, but the advantage of using HealPix is that it efficiently allows one to calculate the set of pixels that are within a given angular distance from any point in the survey.

In practice, this allows us to break a survey into very small regions that contain relatively few sources. In the traditional approach, this would lead to the loss of many potentially useful lens-source pairs. However, because we can calculate which pixels are within a given separation from our source, we keep *all* of the useful lens-source pairs while simultaneously minimizing the number of calculations of lens-source pair separations for pairs that are not useful.

We begin by preprocessing the entire source catalogue for a given weak lensing survey, calculating the pixel ID for each source and storing it in the catalogue. Then, using the known redshift of each lens, we calculate the angular size which corresponds to the physical scale we

[1] https://healpix.sourceforge.io/

are interested in. Healpix then determines every pixel ID that overlaps with a circle around the lens with the radius of that angular size. The lens-source angular separation can then be calculated for each pair without having to waste computation time on a large number of pairs that are too separated to be useful. Using Healpix also ensures that we capture every source within a given radius to the lens, as opposed to other optimization strategies that can omit lens-source pairs for lenses that fall on the edge of a catalogue tile. This strategy ensures that we have the strongest possible signal without the extreme computational overhead of calculating the lens-source separations for every source in the catalogue.

A.3 Weak Lensing for the Masses

Figure A.1 shows the interface for "Weak Lensing for the Masses". This webpage, which is hosted on an Ubuntu[2] server, is written using the flask package[3] which facilitates web development in python. Users provide their email address and a comma separated list of right ascensions, declinations, and redshifts that correspond to each of their lenses. Users can then select between one of two publicly available weak lensing shape catalogues. When users submit their request, it is saved to a MySQL database[4]. The server processes the requests one at a time, on a first come first served basis.

The server contains the public releases of the CFHTLenS and KiDS DR2 weak lensing catalogues, which have been loaded into healpy[5], a Python wrapper around the C++ HealPix libraries. The catalogues are processed slightly differently due to the varying survey parameters. For example, KiDS DR2 provides a full posterior for the photometric redshift of every source in the catalog, while CFHTLenS does not. For KiDS, we follow processing guidelines defined in Appendix C of Kuijken et al. (2015). Specifically, we reject all sources that do not meet the following criteria:

- MAN_MASK = 0
- WEIGHT > 0
- 0.005 < z_B < 1.2
- SNRATIO > 0

[2]https://ubuntu.com/
[3]https://flask.palletsprojects.com/en/2.0.x/
[4]https://www.mysql.com/
[5]https://healpy.readthedocs.io/en/latest/

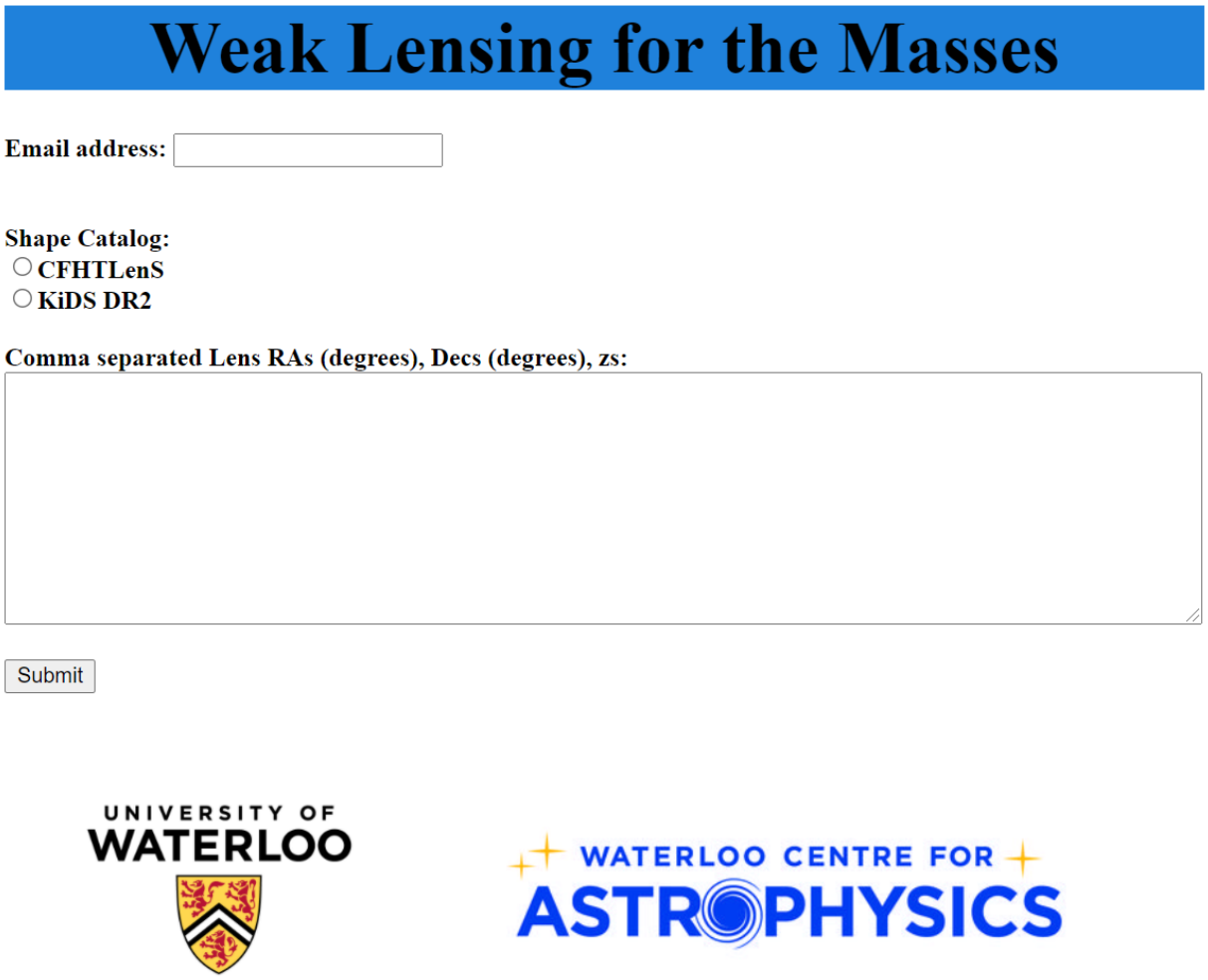

Figure A.1: The interface for Weak Lensing for the Masses

All multiplicative and corrective biases are also applied to the shape measurements for each source.

For CFHTLenS, we apply a similar set of cuts to the *lens*fit shape measurements. CFHTLenS does not provide a full $p(z)$ redshift probability distribution. Instead, we model the $p(z)$ as a gaussian with $\sigma = (1.0 + z) * 0.04$. As we calculate Σ_{cr}^{-1} by integrating from z_l to ∞, treating the redshift as a Gaussian probability distribution function will downweight sources that are near to the lens in redshift space, where we expect the shearing to be minimal.

The python framework is designed to be extensible. As other weak lensing surveys, or newer releases of existing surveys become public in the future, the catalogues can quickly be processed and added to the server.

Once the server is finished analysing the job, the output is emailed back to the user at the address they provided. The output consists of figures for the $\Delta\Sigma$ and the γ_t profiles, as well as text files containing the data points for the figures, the mean Σ_{cr} value, the γ_x values, and the weights for each bin.

A.3.1 Model Fitting

Fitting the $\Delta\Sigma$ profiles with a model can be a complex process. The model one chooses can be largely dependent on the type of objects being measured. If measuring the weak lensing signal from satellite galaxies, for example, one must factor in the offset halo term due to the group or cluster halo. If measuring centrals, one should also fit for a miscentring parameter, as your choice of the group centre might not be accurate. If only fitting a single NFW, one should know the mean virial radius of the objects so as to not bias the fit with signal from external sources.

As our pipeline has no way of knowing what types of objects are being measured or what their expected masses and virial radii are, we opt to leave the fitting up to the user. There are existing tools that can make the complicated process of fitting models to the data easier. CLUSTER-LENSING[6] (Ford & VanderPlas, 2016) is a publicly available python package for calculating properties of NFW halos, including $\Delta\Sigma$ profiles and miscentring terms. For simple fits, such as cluster/group centres or field galaxies, cluster-lensing and an MCMC package such as EMCEE[7] (Foreman-Mackey et al., 2013) is sufficient to achieve a fit and halo mass estimate.

If fitting the inner-most bins of the signal is important, and the stellar mass is known, one should also include the stellar matter component to the $\Delta\Sigma$. This is easily modelled as a point

[6]https://github.com/jesford/cluster-lensing
[7]https://emcee.readthedocs.io/en/stable/

source. The $\Delta\Sigma$ signal for a point source is simply:

$$\Delta\Sigma = \frac{M}{\pi\, R^2}\,. \tag{A.1}$$

This term can then be added to the fit $\Delta\Sigma$ profile.

For satellite galaxies, or galaxies in high density environments, one must also consider contributions to the weak lensing signal from external sources. To model these terms, one can follow the prescription of Gillis et al. (2013), equations 11-13.

A.4 Comparison

As a test of the processing pipeline, we compare the $\Delta\Sigma$ signal generated by our pipeline to one from a published article. We use the same list of lenses used to produce the panel in the 3rd row, 3rd column of Figure 2 of Hudson et al. (2015). To simplify the comparison, we focus on the region that is dominated by the NFW halo. A comparison of the $\Delta\Sigma$ profiles can be seen in Figure A.2.

Though there are some differences, it should be noted that the binning used to reproduce the figure is not identical. Naturally, the processing pipelines themselves are different. Despite the differences, the signals are corellated, as expected. Additionally, an NFW fit to the signal generated using the pipeline described in this chapter is in good agreement with the published mass from Hudson et al. (2015).

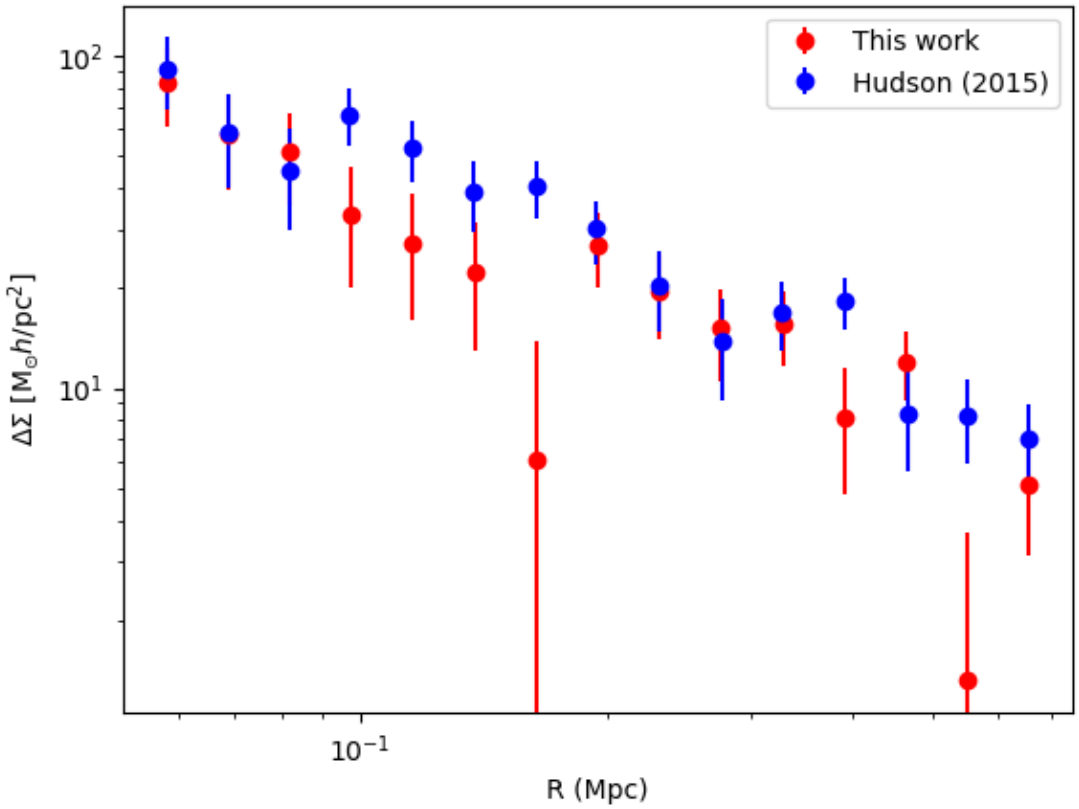

Figure A.2: Comparison of weak lensing signals from this work (red) and Hudson et al. (2015) (blue). To simplify the fitting process, we only consider the radial bins dominated by the NFW term.